UNIVERSITÉ DE MONTRÉAL

VISCOELASTIC DISTORTION DURING MANUFACTURING AND POST-CURING OF THERMOSET COMPOSITES: CHARACTERIZATION AND MODELING

MARÍA BENAVENTE MIANA
DÉPARTEMENT DE GÉNIE MÉCANIQUE
ÉCOLE POLYTECHNIQUE DE MONTRÉAL

THÈSE PRÉSENTÉE EN VUE DE L'OBTENTION
DU DIPLÔME DE PHILOSOPHIÆ DOCTOR
(GÉNIE MÉCANIQUE)
DÉCEMBRE 2017

UNIVERSITÉ DE MONTRÉAL

ÉCOLE POLYTECHNIQUE DE MONTRÉAL

Cette thèse intitulée :

VISCOELASTIC DISTORTION DURING MANUFACTURING AND POST-CURING OF THERMOSET COMPOSITES: CHARACTERIZATION AND MODELING

présentée par : BENAVENTE MIANA María
en vue de l'obtention du diplôme de : Philosophiæ Doctor
a été dûment acceptée par le jury d'examen constitué de :

M. LABERGE LEBEL Louis, Ph. D., président
M. RUIZ Eduardo Antonio Julian, Ph. D., membre et directeur de recherche
M. LÉVESQUE Martin, Ph. D., membre et codirecteur de recherche
M. HUBERT Pascal, Ph. D., membre
M. BOYARD Nicolas, Ph. D., membre externe

DEDICATION

To $OI\nabla$, you already know.
To my love Nico.

A $OI\nabla$, vosotros ya sabéis.
A mi gran apoyo Nico.

ACKNOWLEDGEMENTS

I would like to thank my supervisor Pr. Edu Ruiz for giving me the chance to undertake this work which stimulated me for the past four years. I thank Pr. Martin Levésque, co-director of this thesis, for the support and trust he gave me throughout this project. Their high expectations and scientific rigour challenged me to give the very best of myself and, hence, to exceed my limits. Also, I want to thank Pr. Pascal Hubert and Pr. Nicolas Boyard for being my committee members and Pr. Louis Laberge Lebel for being the Jury President.

I wish to express my sincere appreciation and gratitude to Lionel Marcin from Safran Tech, Thierry Godon from Safran Aircraft Engines and Nicolas Carrere from Safran Composites. Much of this work would not have been possible without their guidance and assistance.

I would like to thank the members of the A2C2 and LM2 laboratories who I had the chance to work with : Maurice Dykmans, Jesus Fernández Verbo, Nicolas Vernet, Jon Zubimendi, Grégory Martinez, Hubert Courteau-Godmaire, Rolland Delorme, Ilyass Tabiai and Alessandro Scola. I would like to particularly thank Christophe Ravey, Joffrey Renaud, Cédric Pupin and Alice Courtois for their advice, moral support and friendship. I would like to deeply acknowledge Philippe Causse for all the support, trust and advices he gave me at the beginning of this project. The technical advice and support of Catherine Billotte, Roland Fosting and Christian-Charles Martel are also gratefully acknowledged.

I owe special gratitude to my friends and family. I thank Alberto, Esther, Gabriel, Daphné and Javier for their support and kindness. I would like to express my heartfelt gratitude to my parents and brother who have always encouraged me to move forward and pursue my dreams. You were always by my side, even when we were 6,000 Km apart.

Finally, I would like to thank Nico for his love and patience. Your unconditional support gave me courage to overcome the difficult times. I could not have done it without you.

RÉSUMÉ

L'utilisation des matériaux composites à matrice organique (CMO) thermodurcissable dans l'industrie aérospatiale ne cesse d'augmenter, comme le montre le développement des moteurs LEAP de Safran et General Electrics ou les avions C-series de Bombardier. Ces matériaux possèdent un rapport rigidité/masse plus avantageux ainsi qu'une meilleure résistance à la corrosion et à la fatigue que les alliages métalliques. Ces avantages font des matériaux composites d'excellents candidats pour des applications de haute performance. Cependant, leur utilisation pour des composants structuraux a été restreinte de par leur faible résistance au délaminage (particulièrement les composites stratifiés) et leur instabilité géométrique suite à la fabrication.

Depuis les années 1960, des renforts tridimensionnels (3D) ont été développés pour améliorer la résistance à l'impact et au délaminage des composites. Les instabilités géométriques sont essentiellement attribuables aux contraintes résiduelles qui se développent pendant la fabrication. Le retrait chimique de la résine, l'incompatibilité des coefficients de dilatation thermique du renfort et de la matrice et l'interaction entre la pièce et le moule sont connus pour être les principaux mécanismes responsables de la génération des contraintes résiduelles. Ces distortions sont préjudiciables pour les profils aérodynamiques, comme celui des aubes soufflantes. L'industrie aérospatiale déploie donc des efforts considérables pour les éviter. Actuellement, les moules et les paramètres de fabrication sont modifiés suivant une méthode essais-erreurs pour tenir compte de la distortion induite au cours du procédé de fabrication. Il est donc essentiel de développer une méthodologie numérique pour concevoir les moules et déterminer les paramètres de fabrication réduisant les instabilités géométriques.

Ce travail vise à comprendre l'origine physique de la distortion résiduelle rencontrée dans des pièces composites pendant le cycle de post-cuisson et à développer un outil numérique pour prédire les contraintes résiduelles et la distortion géométrique induites au cours d'un cycle de fabrication de moulage par transfert de résine (Resin Transfer Molding, RTM).

Premièrement, une nouvelle hypothèse basée sur le comportement viscoélastique des composites a été présentée pour expliquer l'évolution de la distortion géométrique de pièces ayant été soumises à un cycle de post-cuisson. Elle suppose que du fluage peut être observé pendant le cycle de post-cuisson réalisé à l'extérieur du moule de fabrication, augmentant ainsi la distorsion géométrique des pièces. Pour valider cette hypothèse, six plaques bilames à renforts 3D interlock ont été fabriquées et soumises à différents cycles de post-cuisson. La distortion géométrique a été mesurée après le cycle de fabrication en utilisant un palpeur électronique et

par analyse d'images pendant la post-cuisson à l'extérieur du moule. Les résultats ont montré que la déflection des plaques bilames pouvait augmenter jusqu'à 20 % après qu'elles aient été soumises à un cycle de post-cuisson à l'extérieur du moule de fabrication. De plus, il a été constaté que l'évolution de la déflection pendant les cycles de post-cuisson était dépendante du temps et de la température.

Une revue rigoureuse et exhaustive des modèles numériques généralement utilisés dans la littérature pour prédire les contraintes résiduelles développées au cours de la fabrication a été presentée. La validité et la précision des modèles élastiques, viscoélastiques et pseudo-viscoélastiques ("path-dependent") ainsi que leur implémentation dans un logiciel d'éléments finis ont été analysées en calculant l'évolution des contraintes et des déformations d'un élément soumis à des cycles thermiques et mécaniques. Les résultats ont révélé que les modèles élastique-instantané et pseudo-viscoélastique n'étaient pas adaptés aux simulations qui incluent une évolution des propriétés mécaniques au cours de l'analyse. Par conséquent, ils ne sont pas valides pour prédire les contraintes résiduelles développées au cours de la fabrication.

Finalement, une approche modulaire a été développée pour simuler les phénomènes thermiques, chimiques et mécaniques qui ont lieu simultanément pendant le procédé de fabrication et la post-cuisson. Les distorsions géométriques développées lors de la fabrication des plaques bilames à renfort 3D interlock ont été calculées en utilisant des modèles thermo-élastique et viscoélastique. Les résultats obtenus ont été comparés avec la déflection mesurée expérimentalement après le cycle de fabrication en RTM et lors du processus de post-cuisson des plaques bilames. Il a été constaté que les modèles thermo-élastique et viscoélastique prévoyaient des contraintes résiduelles et une distortion géométrique similaires pendant le cycle RTM étudié. De plus, ils entraînaient des divergences inférieures à 5 % par rapport aux mesures expérimentales. Cependant, de la relaxation de contraintes et du fluage significatifs ont été prédits par le modèle viscoélastique lors des simulations sur un élément soumis à des cycles mécaniques à haute température. Ces résultats suggéraient que différents cycles de cuisson (*i.e.,* taux de refroidissement plus lents) pouvaient entraîner de la relaxation des contraintes et donc des divergences significatives entre ces modèles. Ainsi, le modèle viscoélastique a prédit avec précision l'évolution de la distortion géométrique mesurée expérimentalement pendant un cycle de post-cuisson à l'éxtérieur du moule de fabrication. Il a prévu une augmentation de la distortion géométrique allant jusqu'à 15 % dans des plaques bilames selon le temps et la température de post-cuisson. Ces résultats ont confirmé que l'augmentation de la distortion géométrique est induite par le fluage et valident donc l'hypothèse proposée.

Dans cette thèse, une analyse approfondie de l'origine physique de la distortion résiduelle rencontrée dans des pièces composites pendant le cycle de post-cuisson à été menée. L'outil

numérique développé a été utilisé avec succès pour prédire la distortion géométrique induite au cours d'une fabrication RTM avec des cycles de post-cuisson dans des plaques bilames à renfort 3D interlock. Les résultats ont révélé que le comportement viscoélastique doit être pris en compte pour prédire précisément l'évolution de la distortion géométrique au cours d'un procédé de fabrication incluant des étapes de post-cuisson.

ABSTRACT

This thesis aimed at understanding the physical origins of process-induced residual distortion in composite parts during the post-curing process and to develop a numerical tool to predict the residual stresses and geometrical distortion developed during Resin Transfer Molding (RTM) and post-curing processes.

Firstly, an hypothesis based on the composite's viscoelastic behavior was presented to explain the geometrical distortion evolution encountered in parts after being submitted to a free-standing post-curing cycle. This hypothesis states that creep strains can develop during the heating and isotherm phases of a free-standing post-curing process, thus increasing the part's geometrical distortion. To validate this hypothesis, six flat plates with a [0/90] lay-up configuration reinforced with a three dimensional interlock woven fabric were manufactured and submitted to different post-curing cycles. The geometrical distortion was measured after the manufacturing cycle using a Linear Variable Differential Transducer (LVDT) and during the post-curing cycle by digital image analysis. The results showed that the geometrical distortion could increase by up to 20 % after once the plate is submitted to a free-standing post-curing cycle. Moreover, it was found that the post-curing geometrical distortion evolution was time and temperature dependent.

A rigorous and comprehensive review of the numerical models generally used in the literature to predict residual stresses and geometrical distortions developed during the manufacturing process of composite parts is presented. The validity and accuracy of elastic (*i.e.,* CHILE), viscoelastic and path-dependent models and their implementation into a finite element software have been analyzed by computing the stresses and strains evolution during single element simulations exposed to thermal and mechanical cycles. The results revealed that the instantaneous-elastic and path-dependent models were not suitable for simulations where the mechanical properties evolve during the analysis.

Finally, a sequentially modular approach was developed to simulate the thermo-chemo-mechanical phenomena involved in the manufacturing and post-manufacturing processes. The geometrical distortion developed during the manufacturing of asymmetric plates was computed using thermo-elastic and viscoelastic models was compared to those measured experimentally after the RTM manufacturing and during the post-curing process. It was found that elastic and viscoelastic models predicted similar residual stresses and geometrical distortion evolution during the studied RTM manufacturing process and led to discrepancies lower than 5 %, when compared to experimental measurements. However, significant stresses re-

laxation and creep strains were predicted by the viscoelastic model during the single element analysis at high temperature and, therefore, different cure cycles (*i.e.,* slower cool-down rates) could led to significant discrepancies between those models. Moreover, the viscoelastic model predicted accurately the time- and temperature-dependent geometrical distortion evolution phenomenon measured experimentally during the post-curing process. A 15 % increase was predicted by the viscoelastic model after submitting the part to a free-standing post-curing process. These results confirmed that the increase of geometrical distortion is generated by the time and temperature dependent creep strains, hence validated the hypothesis proposed in this thesis.

In this work, a thorough analysis of the physical origins of process-induced residual distortion in composite parts during the post-curing process was conducted. The developed numerical tool has been successfully used to predict the geometrical distortion developed during the RTM manufacturing and post-curing processes of asymmetric plates reinforced with 3D interlock fabric. The results revealed that a degree of cure and temperature-dependent viscoelastic model was required to accurately predict the different thermo-chemo-mechanical phenomena triggered by the manufacturing and post-curing processes. Finally, the numerical code has been transferred to our industrial partner to predict the residual stresses developed during the manufacturing and post-curing of structural parts.

TABLE OF CONTENTS

LIST OF TABLES

LIST OF FIGURES

LIST OF SYMBOLS AND ABBREVIATIONS

α	Degree of cure
α_{gel}	Gel point
β_r	Resin's coefficient of chemical shrinkage
$\boldsymbol{\beta}_c$	Composites's coefficient of chemical shrinkage
$\boldsymbol{\varepsilon}$	Mechanical strains
$\boldsymbol{\varepsilon}^{NM}$	Non mechanical strains
$\boldsymbol{\varepsilon}^{T}$	Total strains
$\boldsymbol{\kappa}$	Thermal conductivity
K	Plate's curvature
K_0	Plate's post-manufacturing curvature
$\boldsymbol{\lambda}$	DiBenedetto material constant
ρ_c	Composite's density
ρ_r	Resin's density
ν^r	Resin's Poisson ratio
ν^f	Fabric's Poisson ratio
ω^k	Inverted relaxation times
θ_g^r	Resin's coefficient of thermal expansion in the glassy state
θ_r^r	Resin's coefficient of thermal expansion in the rubbery state
$\boldsymbol{\theta}_g^c$	Composite's coefficient of thermal expansion in the glassy state
$\boldsymbol{\theta}_r^c$	Composite's coefficient of thermal expansion in the rubbery state
$\boldsymbol{\sigma}$	Stresses
ζ_{pc}	Composite's specific heat
$\boldsymbol{\chi}$	Viscoelastic hidden internal variables
$\frac{\partial \Delta \boldsymbol{\sigma}}{\partial \Delta \boldsymbol{\varepsilon}}$	Jacobian matrix
A_i	Arrhenius constant
a_T	Viscoelastic shift factor
$\mathbf{C}^0$	Instantaneous stiffness tensor
$\mathbf{C}^k$	Relaxation stiffness tensors
$\mathbf{C}^\infty$	Completely relaxed stiffness tensor
$\mathbf{C}_e(T^*)$	Cure and temperature dependent elastic stiffness tensor
$\mathbf{C}_{PD}(T, \alpha)$	Cure and temperature dependent path dependent stiffness tensor
E_i	Arrhenius activation energy
E^r	Resins's Young modulus

E^f	Fabric's Young modulus
H_r	Resin's enthalpy
H_i	Resin's activation energy (shift factor model)
k_i	Chemical reaction rate constants (Kamal-Sourour model)
m	Material constants (Kamal-Sourour model)
$\dot{Q}_r$	Internal heat generation rate
R	Ideal gas constant
r	Plate's curvature radius
$\boldsymbol{s}$	Path-dependent history state variable
T	Temperature
T_g	Glass transition temperature
t	Time
V^f	Fabric's volume fraction
V_s^r	Resin's volume shrinkage
2D	Two Dimensional
3D	Three Dimensional
CHILE	Cure Hardening Instantaneous Linear Elastic
CLT	Classical Laminate Theory
CTE	Coefficient of Thermal Expansion
DGEBF	Diglycidyl Ether of Bisphenol F
DMTA	Dynamic Mechanical Thermal Analysis
FBG	Fiber Bragg Gratting
FD	Finite Difference
FE	Finite Element
FEA	Finite Element Analysis
LVDT	Linear Variable Differential Transformer
M-DSC	Modulated Differential Scanning Calorimeter
RTM	Resin Transfer Molding
TMA	Thermo-Mechanical Analysis
TTSP	Time Temperature Superposition Principle
DC3D8	Abaqus eight-node linear brick element (heat transfer analysis)
C3D8	Abaqus eight-node linear brick element (mechanical analysis)
C3D20	Abaqus twenty-node brick element (mechanical analysis)

LIST OF APPENDICES

CHAPTER 1 INTRODUCTION

Thermoset matrix composites are increasingly used in the aerospace industry. This trend is partially due to their high specific mechanical, corrosion and fatigue resistance properties, when compared to those of metals. However, their use in structural components has been limitedart, by their low delamination resistance (for laminated composites) and post manufacturing geometrical stability.

Three-dimensionally (3D) reinforced composites have been developed to improve delamination and impact resistance by the presence of fibers in the out-of-plane direction which stop or reduce the growth of delamination cracks. Moreover, 3D weaving techniques are being used to produce near-net-shape of complicated geometries that can greatly reduce the manufacturing cost of those parts. For those reasons, three-dimensionally reinforced composites are now being used in the aerospace industry for structural components, such as engines, turbine rotors and rocket nozzles, among others.

Geometrical instabilities are essentially triggered by the residual stresses built-up during manufacturing. Resin's chemical shrinkage, Coefficient of Thermal Expansion (CTE) mismatch between the reinforcement and the matrix, and tool-part interaction are known to be the main mechanisms responsible for the residual stresses generation. These geometrical instabilities are detrimental for aerodynamic profiles and the aerospace industry deploys significant efforts to minimize them. Molds and manufacturing process parameters are nowadays modified on a trial and error basis to alleviate manufacturing process induced distortions. There is therefore a need to develop a scientific understanding that could lead to optimized molds and processing parameters reducing manufacturing induced distortions within acceptable tolerances.

This work is part of the NSERC-Safran Industrial Research Chair on Novel 3D Composite Materials for the Aerospace Industry. The Chair specifically deals with the development of manufacturing processes for composites structural parts through the impregnation of three-dimensional (3D) reinforcement by the liquid injection technique. The project was decomposed into two sub-projects : *i*) the first sub-project dealt with the development of a multi-scale homogenized model for predicting the composite's viscoelastic behavior as a function of degree of cure and temperature. It involved one PhD student. *ii*) the second sub-project, which is the subject of this thesis, dealt with the characterization and prediction of the residual stresses developed during the manufacturing of composite parts reinforced with 3D interlock woven carbon fibers by the Resin Transfer Molding (RTM) process.

This study focused especially on the physical origins of process-induced residual distortion in composite parts reinforced with 3D woven interlock fabric during manufacturing and free-standing post-curing processes. It addressed three objectives, namely characterization of asymmetric plates geometrical distortion with time and temperature, implementation of degree of cure- and temperature-dependent mechanical models into a Finite-Element software and development of a numerical tool to capture the thermo-chemo-mechanical phenomena involved in the manufacturing and post-curing of composites. The novelty of this project relies on the study, prediction and comprehension of the geometrical distortion evolution during different post-curing cycles in composite plates.

This thesis is organized as follows. Chapter 2 presents a literature survey on thermoset composites and the mechanisms responsible for the residual stresses built-up during the manufacturing. Chapter 3 introduces the project's research objectives and describes the relationship between the objectives and the publication strategy. The three articles resulting from this work are presented in Chapters 4 to 6. Chapter 4 details the studies of the viscoelastic effects on the geometric distortion of asymmetric plates reinforced with 3D interlock fabric. Chapter 5 presents the numerical code and material models developed to predict the residual stresses built-up during the manufacturing process. Chapter 6 presents a comparison between experimental data and the predicted geometrical distortion for different post-curing cycles and part geometries. Chapter 7 discusses the relationship between the articles. The contributions and limitations from this thesis are finally summarized and topics for future studies are recommended.

CHAPTER 2 LITERATURE REVIEW

Numerical modeling used to predict the residual stresses developed during the manufacturing of composite parts has gained interesest in the last decades. In early works on process modeling, the authors assumed that the thermal strains were the only source of residual stresses. However, it has been proven that, over the manufacturing process, composite components undergo different states and interactions that can also induce residual stresses. This chapter contains a comprehensive review on the mechanisms involved in the residual stresses and geometrical distortion development during the manufacturing process of composite parts. The mechanical properties having an effect on the residual stresses development are presented. Then, the process modeling methodology generally used in the literature to capture the thermo-chemo-mechanical phenomena occurring during composite manufacturing is described. Finally, the experimental techniques used to characterize the effect of the main mechanisms of residual stresses generation are presented.

The modified Voigt notation has been adopted in this section to represent tensors. Thus, symmetric second-order tensors were expressed as six-component vectors and symmetric fourth-order tensors were expressed as 6×6 matrices. Light-faced letters (*i.e.,* a, α, A) denoted scalar quantities, boldfaced lowercase Greek letters (*i.e.,* $\boldsymbol{\sigma}$) represented second order tensors while fourth-order tensors were represented by boldfaced capital Roman letters (*i.e.,* $\mathbf{C}$).

2.1 Sources of residual stresses and geometrical distortion during the RTM process

Residual stresses are self-balanced stresses that are present in a material free of any external load or thermal gradient. Their presence in a composite part can lead to matrix cracking or/and geometrical distortion that results in a reduction of the composite structure performance and difficulties during the assembly (Novak and DeCrescente, 1970; Naik et al., 2002; Ruiz and Trochu, 2005a; Causse et al., 2012). The thermal strains, chemical shrinkage and tool part interaction have been identified as the main mechanisms of residual stresses generation (Radford and Rennick, 2000; Wisnom et al., 2006; Parlevliet et al., 2006; Radford, 2010). Temperature and degree of cure gradients during manufacturing, cure cycle, manufacturing process and humidity, among others, can also have an impact in the residual stresses and hence the geometrical distortion (Bogetti and Gillespie Jr, 1992; White and Hahn, 1993; Fernlund et al., 2002; Ruiz and Trochu, 2006; Palerosi and de Almeida, 2007).

Figure 2.1 shows schematically the residual stresses generation during a traditional Resin Transfer Molding (RTM) cycle. In the first stage the reinforcement is placed in the mold's cavity prior the resin injection. Once the mold is closed, the reinforcement is compacted by the rigid mold which can induce to fiber displacement, tension in the reinforcement ply and non-uniform fiber volume fraction distribution (Gao and Young, 2002; Potter et al., 2005; Dong, 2011). Then the mold is preheated, during this section the coefficient of thermal expansion mismatch between the reinforcement and the tool can induce residual stresses into the fibers. Once the temperature is stabilized the resin is injected into the mold. Prior the resin solidification (gel point) it is commonly assumed that the chemical shrinkage and the coefficient of thermal expansion mismatch between the fibers and the matrix do not generate any residual stresses in the composite since the resin is still in the liquid state. After the gel point, the chemical shrinkage will induce residual stresses until the part is completely cured (White and Hahn, 1993; Ersoy et al., 2005). The effect of thermal strains on the residual stresses development become particularly significant during the cool-down stage (Hahn and Pagano, 1975; Radford and Diefendorf, 1993). Finally, the tool-part interaction define the parts boundary conditions and can induce residual stresses relaxation over in-mold manufacturing (Kim and White, 1997; Kiasat and Mostofi, 2008).

2.2 Material properties evolution during the RTM process

The residual stresses development during the manufacturing are highly dependent on the composite constituents properties evolution. During the manufacturing the fibers mechanical properties, and hence the reinforcement mechanical properties, are typically assumed to remain stable (Ersoy et al., 2010a; Khoun et al., 2012). Consequently, the composite's mechanical properties evolution during manufacturing are governed by the resin behavior during cure (White and Kim, 1998; Ersoy et al., 2010b).

2.2.1 Fibrous reinforcement

A fibrous reinforcement architecture is a multi-scale assemblage of microscopic fibers into yarns, themselves arranged according to a particular pattern which conditions the composite's overall properties.

Recent developments on weaving techniques enabled the fabrication of three-dimensional (3D) reinforcements. Three dimensional architectures can be classified according to their through-thickness reinforcement as : orthogonal, multi-axial or interlock, among others. 3D interlock woven fabrics are composed of superimposed weft tows held together in-plane and out-of

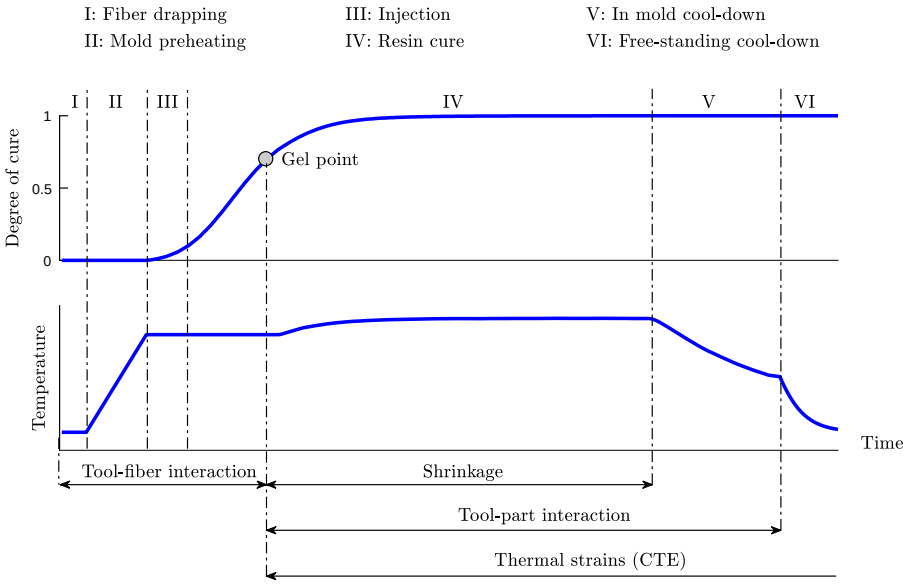

Figure 2.1 Schematic representation of the mechanisms generating residual stresses during the RTM manufacturing process (Causse and Trochu, 2012)

plane (thickness direction) by warp yarns, as shown in Figure 2.2. Those fabrics enhance post-impact strength, damage and delamination resistance (Mouritz et al., 1999; Tong et al., 2002; Baucom and Zikry, 2005; Naik et al., 2002), when compared to traditional laminates. Moreover, the design of the weaving architecture can be optimized for each specific application. For those reasons, three-dimensional reinforcement architectures are being used in the aerospace industry for structural components, such as fan cases and fan blades (De Luycker et al., 2009).

2.2.2 Thermoset matrices

Thermoset polymers are characterized by the generation of an irreversible 3D molecular network during their curing. Thermoset resins undergo three different states during the manufacturing process. Initially in a liquid state, the resin becomes rubbery as the process advances. This physical transformation is caused by the cross-linking of growing polymer chains creating a network of high molecular weight. The transformation from a viscous liquid to an elastic rubber is referred to as the gel point. Finally, the thermoset resin reaches a glassy/solid state when most of the cross-links are formed and the motion of the polymer chains is restrained. The cross-linking process is quantified by the degree of cure, α. This variable ranges from 0 to 1, corresponding to the uncured and completely cure states,

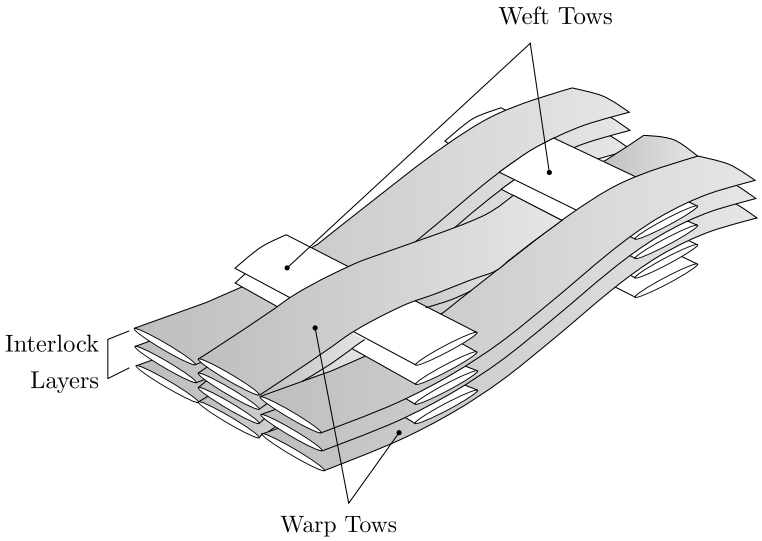

Figure 2.2 Schematic representation of a 3D interlock ply with four interlock layers

respectively.

Along the years, several models have been developed to describe the properties evolution with the degree of cure. The main models found in the literature to describe the cure kinetics, the volumetric changes and the mechanical properties are presented herein.

Cure kinetics

The cure reaction rate of a thermoset matrix is generally described using phenomenological models. The total heat of reaction released during the cure is measured using a Differential Scanning Calorimeter (DSC) under isotherm and dynamic conditions.

The reaction rate, $\mathrm{d}\alpha/\mathrm{d}t$, is assumed to be proportional to the heat flow rate, $\mathrm{dH}/\mathrm{d}t$, as (Ruiz and Trochu, 2005b; Khoun et al., 2010; Baran et al., 2014)

$$\frac{\mathrm{d}\alpha}{\mathrm{d}t} = \frac{1}{\mathrm{H}_r}\frac{\mathrm{dH}}{\mathrm{d}t} \tag{2.1}$$

where H_r is the total resin enthalpy.

Turi (1981) introduced a simple kinetic model where the reaction rate was expressed by a n-order equation as

$$\frac{\mathrm{d}\alpha}{\mathrm{d}t} = k\,(1-\alpha)^n \tag{2.2}$$

where n was the reaction order and k was the chemical reaction rate constant described by

the Arrhenius temperature dependency equation as

$$k = A \exp\left(-\frac{E}{RT}\right) \tag{2.3}$$

where A, E, R and T were the Arrhenius constant, the Arrhenius activation energy, the ideal gas constant and the temperature, respectively.

However, equation 2.2 cannot account for the simultaneous reactions occurring during the curing progress and the different resin transitions states (*i.e.,* gelification and vitrification) (Yousefi et al., 1997).

Kamal and Sourour (Kamal and Sourour, 1973) developed a phenomenological model that has been widely used in the literature to describe the reaction rate for epoxy resins and reads

$$\frac{\mathrm{d}\alpha}{\mathrm{d}t} = \left(k_1 + k_2\alpha^m\right)(1-\alpha)^n \tag{2.4}$$

where m and n were a material constant and k_1 and k_2 were the chemical reaction rate constants with Arrhenius temperature dependency.

The main drawback of the Kamal and Sourour model is that it does not account for the thermoset vitrification phenomenon. It has been demonstrated that the reaction rate decreases significantly once the resin reaches the glassy/solid state. The restrained chain mobility during the vitrification state causes a shift in the cure rate mechanisms from kinetics to molecular diffusion (Hubert et al., 2001). To account for the diffusion mechanisms, the Kamal and Sourour model from equation 2.4 was modified as

$$\frac{\mathrm{d}\alpha}{\mathrm{d}t} = \left(k_1 + k_2\alpha^m\right)(1-\alpha)^n F(\alpha) \tag{2.5}$$

where $F(\alpha)$ was an empirical formula that accounted for the diffusion phenomena. $F(\alpha)$ has been recently expressed by Pupin et al. (2017) as

$$F(\alpha) = \frac{1}{1+\exp(B_1(\alpha - B_2))}, \tag{2.6}$$

where B_1 and B_2 were material constants.

Volumetric changes

Chemical shrinkage suffered by the resin during its curing and thermal expansion are the main physical causes behind the volumetric variation occurring during the manufacturing process in thermoset matrix.

Chemical shrinkage

Volume contraction occurring during curing is described by the chemical shrinkage coefficient. This contraction is related to a change from van der Waals links, in the liquid state, to stronger covalent bonds, in the glassy state (Khoun et al., 2010; Billotte et al., 2013). The thermoset chemical shrinkage has been typically assumed to vary linearly with the degree of cure after the gel point and to be temperature independent (Khoun et al., 2010; Nawab et al., 2012; Billotte et al., 2013). Nawab et al. (2013c) reviewed the chemical shrinkage characterization techniques generally used in the literature. Figure 2.3 shows the chemical shrinkage measured with a rheometer for different thermal conditions by Khoun et al. (2010).

Coefficient of thermal expansion

The CTE quantifies the contraction or expansion of the material associated with temperature variation. The Thermo-Mechanical Analysis (TMA) technique has been generally used to characterize the CTE in thermoset resins, other methods such as dilatometer (Prasatya et al., 2001) or PVT-α (Nawab et al., 2013c) has also being used to measure the degree of cure-dependent CTE.

Several authors observed that the CTE was higher in the rubbery state (at low degree of cure or above the resin's glass transition temperature) than in the glassy state (Prasatya et al., 2001; Svanberg and Holmberg, 2004a; Ruiz and Trochu, 2005b; Khoun et al., 2010; Nawab et al., 2013a). The resin's CTE has been generally modeled as

$$\boldsymbol{\theta}^r = \begin{cases} \boldsymbol{\theta}_g^r & T < T_g(\alpha) \\ \boldsymbol{\theta}_r^r & T \geq T_g(\alpha) \end{cases} \tag{2.7}$$

where $\boldsymbol{\theta}_g^r$ and $\boldsymbol{\theta}_r^r$ were the coefficients of thermal expansion in the glassy and rubbery state, respectively. $T_g(\alpha)$ was the degree of cure-dependent glass transition temperature obtained from the DiBenedetto equation as (Nielsen, 1969; Pascault and Williams, 1990)

$$\frac{T_g(\alpha) - T_g^{(0)}}{T_g^{(\infty)} - T_g^{(0)}} = \frac{\lambda\alpha}{1 - (1-\lambda)\alpha} \tag{2.8}$$

where T_g^0 and $T_g^{(\infty)}$ were the monomer's and fully cured resin's glass transition temperature, respectively, and λ was a material constant.

Prasatya et al. (2001) modified equation 2.7 to consider a smoother transition around the

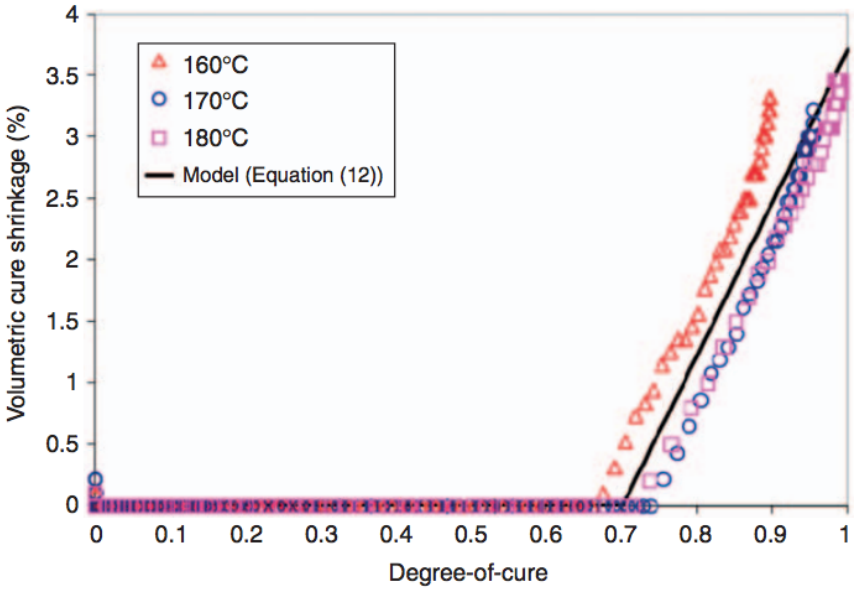

Figure 2.3 Chemical shrinkage evolution with the degree of cure for different thermal conditions (Khoun et al., 2010)

glass transition temperature as

$$\boldsymbol{\theta}^r = \begin{cases} \boldsymbol{\theta}_g^r & T < T_g(\alpha) - 30°C \\ \boldsymbol{\theta}^1 + \boldsymbol{\theta}^2(T - T_g(\alpha)) + \boldsymbol{\theta}^3(T - T_g(\alpha))^2 & T_g(\alpha) - 30°C \leq T < T_g(\alpha) + 15°C \\ \boldsymbol{\theta}_r^r & T \geq T_g(\alpha) + 15°C \end{cases} \tag{2.9}$$

where $\boldsymbol{\theta}^1$, $\boldsymbol{\theta}^2$ and $\boldsymbol{\theta}^3$ were material constants. This model reproduced more accurately the coefficient of thermal expansion evolution around the glass transition temperature. However, the advantages of using this model, when compared to that from equation 2.7, have never been reported.

Mechanical properties

Elastic behavior

In a linearly elastic solid, the stresses $\boldsymbol{\sigma}$ are related to the strains $\boldsymbol{\varepsilon}$ through

$$\boldsymbol{\sigma} = \mathbf{C} : \boldsymbol{\varepsilon} \tag{2.10}$$

where $\boldsymbol{\varepsilon} = \boldsymbol{\varepsilon}^T - (\boldsymbol{\varepsilon}_C^{NM} + \boldsymbol{\varepsilon}_{TH}^{NM})$, $\boldsymbol{\varepsilon}^T$ is the total strain and $\boldsymbol{\varepsilon}_C^{NM}$ and $\boldsymbol{\varepsilon}_{TH}^{NM}$ are the stress-free strain associated to chemical shrinkage and thermal dilatation, respectively. $\mathbf{C}$ is the elastic

stiffness tensor.

Several models have been developed to account for temperature-softening and cure-hardening effects that can occur simultaneously during the manufacturing. Huang et al. (2000) assumed that the elastic stiffness tensor varied linearly with the degree of cure and was temperature independent as

$$\mathbf{C}(\alpha) = \alpha \mathbf{C} \tag{2.11}$$

where $\mathbf{C}(\alpha)$ was the degree of cure-dependent elastic stiffness tensor.

Johnston (1997) introduced the Cure Hardening Instantaneous Linear Elastic (CHILE) model. For isotropic materials with a constant Poisson's ratio, the CHILE model was expressed as

$$E(T^*) = \begin{cases} E^{(0)} & T^* < T_1 \\ E^{(0)} + \left(E^{(\infty)} - E^{(0)}\right) \frac{T^* - T_1}{T_2 - T_1} & T_1 \leq T^* < T_2 \\ E^{(\infty)} & T_2 \leq T^* \end{cases} \tag{2.12}$$

where $E^{(0)}$ was the Young's modulus at the glassy state, $E^{(\infty)}$ was the Young's modulus at the rubbery state and T_1 and T_2 were material constants. T^* was the difference between the temperature and the instantaneous glass transition temperature, $T^* = T - T_g(\alpha)$. CHILE models have been widely used in the literature to describe the degree of cure- and temperature-dependent elastic behavior of thermoset resins (Johnston et al., 2001; Khoun et al., 2010; Baran et al., 2014).

Ruiz and Trochu (2005b) developed a semi-empirical model to describe the Young's modulus evolution with the temperature and the degree of cure after the gel point. Figure 2.4 shows the Young's modulus evolution measured with a DMTA (Dynamic Mechanical Thermal Analysis) for a polyester resin, and the predictions of the elastic model proposed by Ruiz and Trochu (2005b). The figure shows that the model accurately describes the elastic behavior with the degree of cure and temperature variations. However, Ruiz' model relies on 15 different interpolation parameters, which complexifies its identification.

The main limitation of elastic models is that the matrix spends considerable time in the viscoelastic regime during the manufacturing process and an elastic model cannot reproduce the stress relaxation endured by these materials for high temperatures, or low degrees of cure.

Linearly viscoelastic behavior

Most thermoset materials exhibit a time-dependent response when subjected to mechanical loads, such as creep (for an applied constant stress the measured strain increases as a function of time to an applied constant stress), as shown in Figure 2.5 (a) and stress relaxation (for

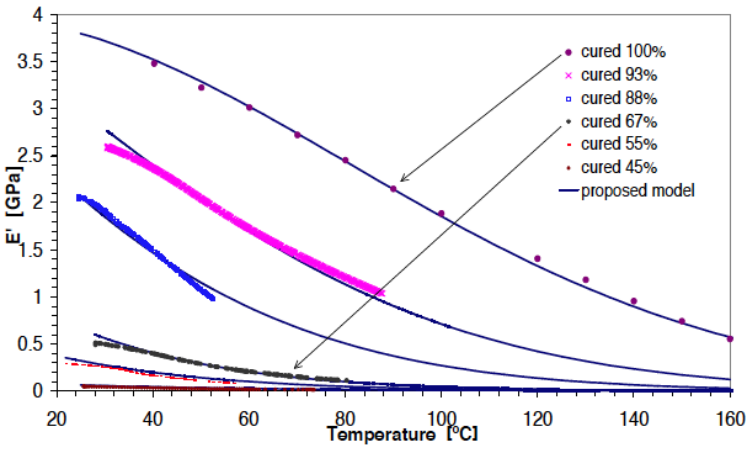

Figure 2.4 Elastic modulus evolution with the degree of cure and temperature measure experimentally and predicted with the model proposed by Ruiz and Trochu (2005b) for a polyester resin

an applied constant strain the measured stress decreases as a function of time), as shown in Figure 2.5 (b) (Schapery, 1969; Lévesque et al., 2008).

Biot (1954) formalized the linearly viscoelastic constitutive theories through a rigorous thermodynamics framework and, for stress-strain relaxation, can be expressed as

$$\boldsymbol{\sigma}(t) = \mathbf{L}^{(1)} : \boldsymbol{\varepsilon}(t) + \mathbf{L}^{(2)} : \boldsymbol{\chi}(t) \tag{2.13a}$$

$$\mathbf{B} : \dot{\boldsymbol{\chi}} + \mathbf{L}^{(3)} : \boldsymbol{\chi} + \left(\mathbf{L}^{(2)}\right)^{T} : \boldsymbol{\varepsilon} = 0 \tag{2.13b}$$

where $\boldsymbol{\chi}$ were hidden internal variables and

$$\mathbf{L} = \begin{bmatrix} \mathbf{L}^{(1)} & \mathbf{L}^{(2)} \\ (\mathbf{L}^{(2)})^{T} & \mathbf{L}^{(3)} \end{bmatrix} \tag{2.14}$$

To meet the first and second principles of thermodynamics, $\mathbf{L}$ must be a positive definite matrix. Thus, $\mathbf{L^{(1)}}$ and $\mathbf{L^{(3)}}$ are also positive definite. $\mathbf{B}$ is a $N \times N$ identity matrix.

The solution of differential equation 2.13 yielded (Luk-Cyr et al., 2013)

$$\sigma_{ij}(t) = \left(L_{ij}^{(1)} - \frac{L_{ir}^{(2)} L_{jr}^{(2)}}{L_{rr}^{(3)}} \right) \varepsilon_j(t) + \frac{L_{ir}^{(2)} L_{jr}^{(2)}}{L_{rr}^{(3)}} \int_0^t \exp\left[-\frac{L_{rr}^{(3)}}{B_{rr}} (t - \tau) \right] \frac{\mathrm{d}\varepsilon_j}{\mathrm{d}\tau} \mathrm{d}\tau \tag{2.15}$$

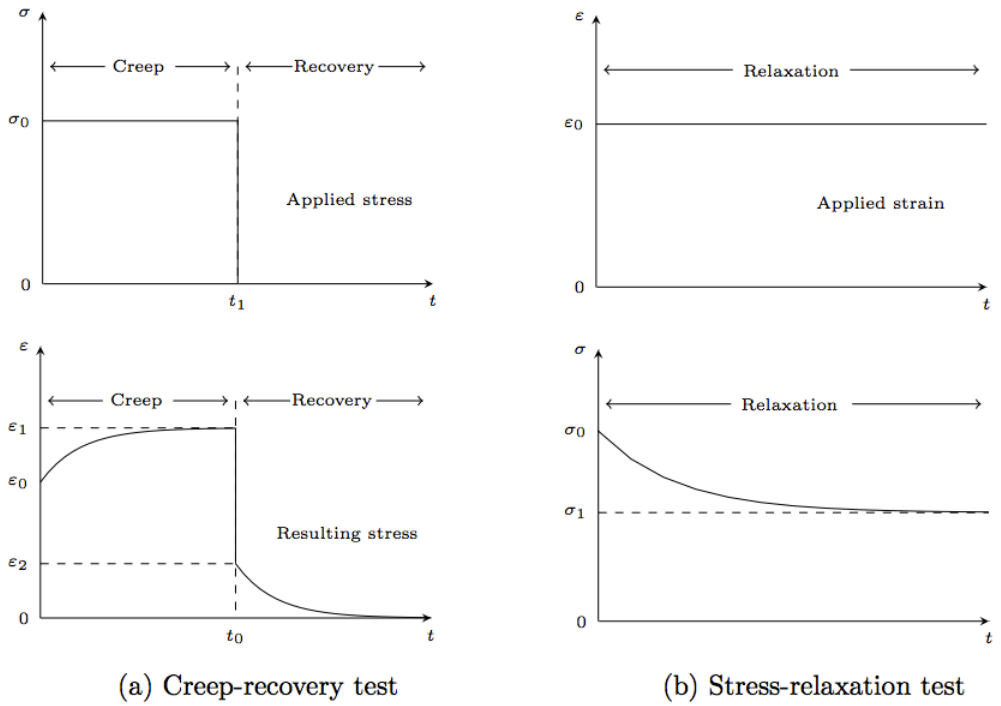

(a) Creep-recovery test (b) Stress-relaxation test

Figure 2.5 Schematic representation of the viscoelastic behavior of a material submitted to a creep-recovery test (a) and a relaxation text (b) (Crochon, 2014)

which can be reduced to

$$\boldsymbol{\sigma}(t) = \mathbf{C}^{(\infty)} : \boldsymbol{\varepsilon} + \int_0^t \sum_{k=1}^{N} \mathbf{C}^{(k)} \exp\left[-\omega^{(k)}\left(t-\tau\right)\right] : \frac{\mathrm{d}\boldsymbol{\varepsilon}}{\mathrm{d}\tau}\mathrm{d}\tau \tag{2.16}$$

where $\mathbf{C}^{(\infty)}$ was the fully relaxed tensor and $\mathbf{C}^{(k)}$ were the relaxation tensors associated to the inverted relaxation times $\omega^{(k)}$.

The viscoelastic behavior is affected, for most polymers, by both the degree of cure and temperature (Ferry, 1980; O'Brien et al., 2001; Ruiz and Trochu, 2005b; Machado et al., 2016). Temperature and degree of cure have been modeled through the Time Temperature Superposition Principle (TTSP). TTSP states, that for thermo-rheologically simple materials, an increase in temperature accelerates the viscoelastic phenomena. Thus, the time scale, $t-\tau$, from equation 2.16 was replaced by

$$\xi - \xi' = \int_0^t \frac{\mathrm{d}\gamma}{a_T(T(\gamma),\alpha(\gamma))} - \int_0^\tau \frac{\mathrm{d}\gamma}{a_T(T(\gamma),\alpha(\gamma))} \tag{2.17}$$

where a_T was a shift factor that depended on the degree of cure, α, and temperature, T.

Figure 2.6 shows the predictions of a degree of cure- and temperature-dependent linearly viscoelastic model developed by Courtois et al. (2016), when compared to the experimental data for an epoxy resin. A Q-800 DMA from TA -Instruments was used to measure the viscoelastic behavior of an epoxy resin at different temperatures. The multi-temperature relaxation test were conducted using a three point-bending set-up on fully (α=1.00) and partially cured specimens. The specimens were submitted to a constant 0.1 % strain during 90 minutes. Then, the load was removed allowing the epoxy specimens to recover. The specimens were then heated by 15 °C and the relaxation time was repeated. The figure shows that a good agreement was observed between the model and the experimental data for different degrees of cure and temperatures.

Linearly viscoelastic constitutive laws are valid as long as the applied load does not induce large changes in the microstructure at the studied temperature and degree of cure. Schapery (1969) developed a non-linear viscoelastic model by introducing loading dependent coefficients into Equation 5.15. Non-linear viscoelastic models have been used to account for the stress, temperature, degree of cure and aging behavior dependence (Adolf and Chambers, 2007; Lévesque et al., 2008; Crochon, 2014; Courtois et al., 2016).

2.3 Process modeling

The last years witnessed a growing interest in modeling the geometrical distortion triggered by the residual stresses built-up during the manufacturing process. Analytical models have been developed to accurately predict the geometrical distortion in L-shape parts and flat panels with asymmetric lay-up configuration (Radford, 1987; Ersoy et al., 2005; Carbajal et al., 2008). However, analytical models are limited to simple geometries and are out of the scope of this project.

The finite element method has been used to compute the residual stresses in the micro-mesoscopic (Zhao et al., 2006; Bayraktar et al., 2012; Brauner et al., 2012; Canal et al., 2015) and the macroscopic scales (Ruiz and Trochu, 2005a; Svanberg et al., 2005; Zeng and Raghavan, 2010; Nielsen, 2012; Baran et al., 2016) for simple and complex geometries. Commercial finite element software such as ABAQUS and ANSYS have been generally combined with user subroutines or Compro Component Architecture to capture the thermo-chemo-mechanical phenomena occurring during manufacturing (Johnston, 1997; Fernlund et al., 2002; Svanberg and Holmberg, 2004a; Ersoy et al., 2010b; Khoun et al., 2011).

In earlier works on process modeling, several authors assumed a stress-free state prior the cool-down stage (Hahn and Pagano, 1975; Hahn, 1976; Weitsman, 1979; Tseng and Osswald,

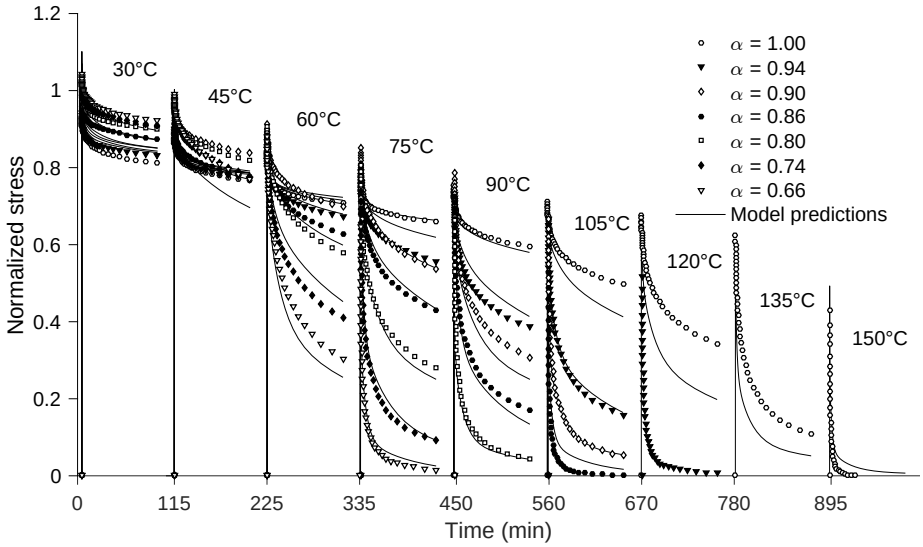

Figure 2.6 Stress relaxation evolution comparison between the experimental data and the degree of cure- and temperature-dependent linearly viscoelastic model developed by Courtois et al. (2016)

1994), thus assuming that the thermal strains were the only source of residual stresses. This approximation neglected the chemical shrinkage strains and the tool part interaction. In recent works, the stress-free state was considered to be at the resin's gel point, thus capturing the chemical, mechanical and thermal effects. A sequential modular approach, proposed by Loos and Springer (1983), has been generally used to describe the thermo-chemo-mechanical phenomena occurring during the manufacturing by autoclave (Loos and Springer, 1983; Bogetti and Gillespie Jr, 1991; White and Hahn, 1992; Johnston, 1997; Joshi et al., 1999; Ersoy et al., 2010b; Fernlund et al., 2002) and RTM (Golestanian and El-Gizawy, 2001; Kim, 2004; Ruiz and Trochu, 2005a; Khoun et al., 2011; Nielsen, 2012).

The modular approach generally used to simulate the RTM process consisted in solving a coupled thermo-chemical model yielding the temperature and degree of cure through the part at each time increment. The temperature and degree of cure obtained in the thermo-chemical model are then implemented as solution-independent variables into a mechanical model to obtain the residual stresses and geometrical distortion. Note that the RTM modular approach accounts for the phenomena occurring during the resin curing once the part is totally impregnated, thus neglecting the injection stage. To the best of the authors knowledge, the influence of the injection stage (flow model) in the RTM process modelling has never been reported.

2.3.1 Coupled thermo-chemical model

Heat transfer analysis based on the Fourier's thermal conductivity equation and the resin's cure kinetics have been combined to compute the degree of cure and temperature distribution through the part during the manufacturing process, yielding

$$\frac{\partial\left(K_x\frac{\partial T}{\partial x}\right)}{\partial x}+\frac{\partial\left(K_y\frac{\partial T}{\partial y}\right)}{\partial y}+\frac{\partial\left(K_z\frac{\partial T}{\partial z}\right)}{\partial z}+\dot{Q}_r=\rho_c\zeta_{pc}\frac{\mathrm{d}T}{\mathrm{d}t} \tag{2.18}$$

where K_i was the composite's thermal conductivity, ρ_c was the composite's density and ζ_{pc} was the composite's specific heat. $\dot{Q}_r$ represented the internal heat generation associated to the exothermic resin reaction, and has been expressed as

$$\dot{Q}_r=\rho_r\left(1-V^f\right)H_r\frac{\mathrm{d}\alpha}{\mathrm{d}t} \tag{2.19}$$

where ρ_r was the resin's density and V^f was the fabric's volume fraction.

Finite difference (Loos and Springer, 1983; Bogetti and Gillespie Jr, 1991; Ruiz and Trochu, 2005a) and finite element (Joshi et al., 1999; Cheung et al., 2004; Zeng and Raghavan, 2010) methods were used to solve Equation 2.18. Finite difference was used in simple geometries and assumed that the temperature and degree of cure only varied in the through thickness direction. For complex parts, ABAQUS finite element software has been combined with HETVAL subroutine to compute the temperature and degree of cure over the manufacturing process.

Finally, some studies assumed that the temperature was constant in thin parts (White and Kim, 1998; Svanberg et al., 2005; Nawab et al., 2013b) and equal to the mold temperature. However, Kim and White (1997) showed that the thermal gradient developed in thick parts during manufacturing could modify the part's residual stresses.

2.3.2 Mechanical model

The mechanical model has been used to compute the non-mechanical strains related to inhomogeneous volumetric variations and mechanical strains governed by the material's mechanical properties. The implementation techniques generally used in the literature for the computation of non-mechanical and mechanical strains are presented below.

Non-mechanical strains

Strains associated to chemical shrinkage were implemented as (White and Kim, 1998; Svanberg and Holmberg, 2004b; Rabearison et al., 2011)

$$\boldsymbol{\varepsilon}_C^{NM}(t+\Delta t) = \boldsymbol{\varepsilon}_C^{NM}(t) + \boldsymbol{\beta^c}(t)\Delta\alpha \tag{2.20}$$

where $\boldsymbol{\beta^c}$ was the composite's coefficients of chemical shrinkage, Δt was the time increment and $\Delta\alpha$ was the degree of cure increment.

Thermal strains ($\boldsymbol{\varepsilon}_{TH}^{NM}$) were computed from (Bogetti and Gillespie Jr, 1992; Khoun et al., 2011)

$$\boldsymbol{\varepsilon}_{TH}^{NM}(t+\Delta t) = \boldsymbol{\varepsilon}_{TH}^{NM}(t) + \boldsymbol{\theta^c}(t)\Delta T \tag{2.21}$$

where $\boldsymbol{\theta^c}$ was the composite's CTE and ΔT was the temperature increment.

Mechanical strains

Finite element softwares, such as ABAQUS or ANSYS, require the definition of the stresses tensor at the end of the increment, $\boldsymbol{\sigma}(t+\Delta t)$, and the Jacobian matrix, $(\partial\Delta\boldsymbol{\sigma}/\partial\Delta\boldsymbol{\varepsilon})$. The stresses tensor at the end of the increment and the Jacobian matrix are presented in this section for the different models generally used in the literature.

Elastic model

A degree of cure- and temperature-dependent elastic model can be obtained from Equations 2.10 and 2.12 as

$$\boldsymbol{\sigma} = \mathbf{C_e}(T^*) : \boldsymbol{\varepsilon} \tag{2.22}$$

where $\mathbf{C_e}(T^*)$ is the degree of cure- and temperature-dependent compliance tensor.

An incremental Hooke's law formulation has been usually used to implement the degree of cure- and temperature-dependent elastic model from Equations 2.22 as (Bogetti and Gillespie Jr, 1991; Zobeiry, 2006; Ding et al., 2016a)

$$\begin{aligned}\Delta\boldsymbol{\sigma} = \boldsymbol{\sigma}(t+\Delta t) - \boldsymbol{\sigma}(t) &= \mathbf{C_e}(T^*(t+\Delta t)) : \boldsymbol{\varepsilon}(\Delta t) \\ &= \mathbf{C_e}(T^* + \Delta T^*)) : \Delta\boldsymbol{\varepsilon}\end{aligned} \tag{2.23}$$

where $\Delta\boldsymbol{\sigma}$ and $\Delta\boldsymbol{\varepsilon}$ were the stresses and strains increment within the time step and $\mathbf{C_e}(T^* + \Delta T^*)$ was the degree of cure- and temperature-dependent compliance tensor at the end of the increment t.

The stress tensor at the end of the increment and Jacobian matrix were expressed as

$$\begin{aligned}\boldsymbol{\sigma}(t+\Delta t) &= \boldsymbol{\sigma}(t) + \Delta\boldsymbol{\sigma} \\ &= \boldsymbol{\sigma}(t) + \mathbf{C_e}(T^* + \Delta T^*) : \Delta\boldsymbol{\varepsilon}\end{aligned} \tag{2.24a}$$

$$\frac{\partial \Delta\boldsymbol{\sigma}}{\partial \Delta\boldsymbol{\varepsilon}} = \mathbf{C_e}(T^* + \Delta T^*) \tag{2.24b}$$

Elastic models have been shown to provide accurate geometrical distortion predictions (Johnston, 1997; Fernlund et al., 2002; David A. Darrow and Smith, 2002). Nevertheless, the validity and applicability of the elastic models and their implementation have not been proven yet.

Zobeiry (2006) simulated the stresses evolution during a free-standing post-curing process. The results revealed that the use of an elastic model yielded a significant discrepancy when compared to the predictions obtained with a viscoelastic model. Zobeiry (2006) concluded that the viscoelastic model was more representative of the reality and, thus, the elastic model was not suitable to predict the evolution of residual stresses during complex cure cycles. However, it is important to note that the presented results were not compared with any experimental data and therefore further analysis must be carried out to understand the stresses evolution during post-curing cycles.

Linearly viscoelastic model

Recursive and Finite Difference (FD) strategies have been used to implement the viscoelastic model into a FE software (Zobeiry, 2006).

Recursive strategies have been used to compute the solution of linearly viscoelastic constitutive theories (Taylor et al., 1970; Zocher et al., 1997; Zhu et al., 2001; Zobeiry, 2006; Nielsen, 2012; Machado et al., 2016). However, most of the recursive strategies exhibit a first order convergence rate. Recently, Crochon et al. (2010) developed a second order recursive strategy for a nonlinearly viscoelastic constitutive theory that increases the convergence rate of the computed solution.

Crochon (2014) solved the differential equations 2.13 with the first order Backward-Euler finite difference scheme as

$$\boldsymbol{\sigma}(t+\Delta t) = \mathbf{L}^{(1)} : \boldsymbol{\varepsilon}(t+\Delta t) + \mathbf{L}^{(2)} : \boldsymbol{\chi}(t+\Delta t) \tag{2.25}$$

where $\mathbf{L}^{(1)} = \mathbf{C}^{(\infty)} + \sum_{k=1}^{k=N} \mathbf{C}^{(k)}$ and

$$\begin{aligned} \boldsymbol{\chi}(t+\Delta t) &= \boldsymbol{\chi}(t) + \Delta t \dot{\boldsymbol{\chi}}(t+\Delta t) \\ &= \boldsymbol{\chi}(t) - \Delta t \mathbf{B}^{-1} : \left(\mathbf{L}^{(3)} : \boldsymbol{\chi}(t+\Delta t) + \left(\mathbf{L}^{(2)} \right)^T : \boldsymbol{\varepsilon}(t+\Delta t) \right) \end{aligned} \tag{2.26}$$

where $\mathbf{B}^{-1}$ was defined as a $N \times N$ identity matrix, $\mathbf{L}^{(2)}$ was a $N \times 6$ matrix expressed as

$$\mathbf{L}^{(2)} = \left(\mathbf{L}^{(2)}_{(1)} | \mathbf{L}^{(2)}_{(2)} | .... | \mathbf{L}^{(2)}_{(k)} \right) \tag{2.27}$$

in which

$$\mathbf{L}^{(2)}_{(k)} : \left(\mathbf{L}^{(2)}_{(k)} \right)^T = \omega^k \mathbf{C}^{(k)} \tag{2.28}$$

and $\mathbf{L}^{(3)}$ was a diagonal matrix of $N \times N$ constructed by 6×6 block diagonal matrices as

$$\mathbf{L}^{(3)} = \oplus_{k=1}^{k=N} [\omega^k \mathbf{I}] \tag{2.29}$$

The combination of equations 2.25 and 2.26 yielded

$$\boldsymbol{\sigma}(t+\Delta t) = \left(\mathbf{L}^{(1)} + \mathbf{L}^{(2)} : \mathbf{W}^{(2)} \right) : \boldsymbol{\varepsilon}(t+\Delta t) + \mathbf{L}^{(2)} : \mathbf{W}^{(1)} : \boldsymbol{\chi}(t) \tag{2.30}$$

where

$$\mathbf{W}^{(1)} = \left(\mathbf{I} + \Delta t \mathbf{B}^{-1} : \mathbf{L}^{(3)} \right)^{-1} \tag{2.31a}$$

$$\mathbf{W}^{(2)} = -\Delta t \mathbf{W}^{(1)} : \mathbf{B}^{-1} : \left(\mathbf{L}^{(2)} \right)^T \tag{2.31b}$$

Regrouping terms led to

$$\boldsymbol{\sigma}(t+\Delta t) = \mathbf{M}^{(1)} : \boldsymbol{\varepsilon}(t+\Delta t) + \mathbf{M}^{(2)} : \boldsymbol{\chi}(t) \tag{2.32a}$$

$$\frac{\partial \Delta \boldsymbol{\sigma}}{\partial \Delta \boldsymbol{\varepsilon}} = \mathbf{M}^{(1)} \tag{2.32b}$$

Differential strategies enable the possibility of using high-order FD schemes, such as the second order Crank-Nicholson or the fourth order Runge-Kutta (Bažant, 1972; Carpenter, 1972; Crochon et al., 2010), which leads to a high-order convergence rate of the computed solution.

Viscoelastic models have been successfully used in the literature to predict geometrical distortion and residual stresses in simple geometry parts (White and Hahn, 1992; Kim and White, 1997; Prasatya et al., 2001; Ding et al., 2016b). However, their use has been limited

due to their complexity and time consuming numerical analyses.

Path-dependent model

Svanberg and Holmberg (2004b) developed a path-dependent constitutive model derived from a viscoelastic formulation and was expressed as

$$\boldsymbol{\sigma} = \begin{cases} \mathbf{C}^{(\infty)} : \boldsymbol{\varepsilon} & T \geq T_g(\alpha) \\ \mathbf{C}^{(0)} : \boldsymbol{\varepsilon} - \mathbf{C}^{(\infty)} : \boldsymbol{\varepsilon}|_{t=t_{vit}} & T < T_g(\alpha) \end{cases} \tag{2.33}$$

where t_{vit} was the time at which the resin's evolved from rubbery to a glassy state, $\mathbf{C}^{(\infty)}$ and $\mathbf{C}^{(0)}$ were the stiffness matrix above and below the glass transition temperature, respectively. The path-dependent model, also known as pseudo-viscoelastic model, assumed that the stiffness matrix remained constant within the rubbery and the glassy states, and varied abruptly from one state to the other at the glass transition temperature (Svanberg and Holmberg, 2004b; Ersoy et al., 2010b; Ding et al., 2017) as

$$\mathbf{C}_{\text{pv}} = \begin{cases} \mathbf{C}^{(\infty)} & T \geq T_g(\alpha) \\ \mathbf{C}^{(0)} & T < T_g(\alpha) \end{cases} \tag{2.34}$$

where $\mathbf{C}_{\text{pv}}$ was the stiffness matrix for a given temperature. Finally, the incremental form of Equation 2.34 yielded to

$$\Delta\boldsymbol{\sigma} = \begin{cases} \mathbf{C}^{(\infty)} : \Delta\boldsymbol{\varepsilon} - \boldsymbol{s}(t) & T \geq T_g \\ \mathbf{C}^{(0)} : \Delta\boldsymbol{\varepsilon} & T < T_g \end{cases} \tag{2.35}$$

where $\boldsymbol{s}$ was a history state variable that accounted for the loading history and was expressed as

$$\boldsymbol{s}(t + \Delta t) = \begin{cases} 0 & T \geq T_g \\ \boldsymbol{s}(t) + \mathbf{C}^{(\infty)} : \Delta\boldsymbol{\varepsilon} & T < T_g \end{cases} \tag{2.36}$$

The stresses tensor at the end of the increment $(t + \Delta t)$ and Jacobian matrix were expressed as

$$\begin{aligned} \boldsymbol{\sigma}(t + \Delta t) &= \boldsymbol{\sigma}(t) + \Delta\boldsymbol{\sigma} \\ &= \boldsymbol{\sigma}(t) + \begin{cases} \mathbf{C}^{(\infty)} : \Delta\boldsymbol{\varepsilon} - \boldsymbol{s}(t) & T(t + \Delta t) \geq T_g \\ \mathbf{C}^{(0)} : \Delta\boldsymbol{\varepsilon} & T(t + \Delta t) < T_g \end{cases} \end{aligned} \tag{2.37a}$$

$$\frac{\partial \Delta\boldsymbol{\sigma}}{\partial \Delta\boldsymbol{\varepsilon}} = \mathbf{C}_{\text{pv}}(t + \Delta t) \tag{2.37b}$$

This model was developed to predict the effect of "frozen-in" stresses released during free-standing post-curing. Pseudo-viscoelastic models have been shown to provide accurate geometrical distortion predictions (Svanberg and Holmberg, 2004a; Ding et al., 2017). However, Svanberg and Holmberg (2004a) observed that the pseudo-viscoelastic model overestimated the phenomena occurring during the post-curing process. Finally, the validity and applicability of pseudo-viscoelastic models have not been studied yet.

2.3.3 Tool-part interaction

The effects of tool-part interaction have been modeled by several numerical modeling approaches (Johnston, 1997; Johnston et al., 2001; Fernlund et al., 2002; Twigg et al., 2004b; Svanberg and Holmberg, 2004a; Khoun et al., 2011).

Johnston et al. (2001) modeled the tool-part interaction by a shearing isotropic layer placed between the tool and the part. The results revealed that the effect of the tool-part interaction on the residual stresses depended on the shear layer properties and extensive sensitivity analyses must be carried out to reproduce the experimental results (Fernlund et al., 2002; Twigg et al., 2004b; Arafath et al., 2008).

Svanberg and Holmberg (2004a) used frictionless contact elements to simulate the tool-part interaction during the RTM manufacturing of curved parts. A comparison between the frictionless, bond-free and perfectly bond simulations revealed that the distortion predicted assuming a frictionless tool-part interaction was the most accurate when compared with the experimental measurements. Khoun et al. (2011) used the Coulomb friction empirical model where the interfacial shear stress was proportional to the contact pressure. The results showed that the friction model predicted qualitatively well the strains evolution during the RTM process. However, further analysis of the frictional model has to be done to validate this approach.

2.4 Geometrical distortion characterization techniques

Strains and geometrical instabilities have been measured over the years to calculate the residual stresses using the Classical Lamination Theory (CLT) or to validate the numerical predictions (Ruiz and Trochu, 2005a). Typically, balanced L- and C-shaped parts and flat plates with asymmetric lay-up configuration have been used to study the geometrical distortion evolution during and after the manufacturing process. The reduction of closed angles in curved parts, also known as spring-in, is governed by the difference between the in-plane and the through the thickness properties (Albert and Fernlund, 2002; Ersoy et al., 2005, 2010b;

Causse et al., 2012). Spring-in angles after manufacturing generally vary between 0.5° and 2.5° (Svanberg and Holmberg, 2001). On the other hand, the geometrical distortion developed in asymmetric plates is governed by the difference between the in-plane properties. The warpage depends on the material, plate's geometry (length and thickness), lay-up configuration and manufacturing process, among others (Ruiz and Trochu, 2005a; Palerosi and de Almeida, 2007; Kiasat and Mostofi, 2008; Stefaniak et al., 2012).

The non-destrucitve techniques generally used in the literature to quantify the individual contributions of different phenomena involved in the manufacturing process, such as chemical shrinkage, CTE and tool part interaction among others, are presented herein.

2.4.1 Chemical shrinkage

Kim and Hahn (1989) characterized the chemical shrinkage contribution in asymmetric plates by interrupting the cure cycle at different stages. During the manufacturing process, the plates were removed from the mold and cooled-down rapidly to room temperature to halt resin curing. The plates curvatures were determined by the specimen's height and chord length. White and Hahn (1992) showed, using the interrupted cure cycle method, that the contribution of chemical shrinkage to residual stresses developed in asymmetric plates accounted for 5 % of the total geometrical distortion. Ersoy et al. (2005) used the same method to study the contribution of chemical shrinkage in L-shape parts. The results revealed that the chemical shrinkage accounted for 50 % of the total angle variation. The key issue of this method is that the samples had to be cooled-down quickly to halt curing. Moreover, the studied parts had to be sufficiently thin to avoid temperature and degree of cure gradients through the thickness.

Fiber Bragg Gratting (FBG) (Khoun et al., 2011; Canal et al., 2015) and strains sensors (Wisnom et al., 2006) have been embedded into composite parts and on the mold's surface prior the manufacturing to monitor the strains evolution during the cure cycle. These methods have been used to capture the strains associated with thermal variation, chemical shrinkage and tool-part interaction (Kim and Daniel, 2002; de Oliveira et al., 2008). However, they are generally difficult to implement and the interpretation of the results remains a challenge (Ifju et al., 1999; Kim and Daniel, 2002). Furthermore, de Oliveira et al. (2008) showed that FBG measured significant experimental variations for the same processing parameters.

2.4.2 Coefficient of thermal expansion

Radford and Diefendorf (1993) developed an experimental technique to measure the spring-

in experienced by L-shape parts instantaneously with the temperature variation. Temperature and angular deflection were measured by the use of a thermocouple and a laser beam which was reflected from a mirror attached to the arm of the sample, as shown in Figure 2.7a. A linear relation was encountered between the geometrical distortion and the temperature variation. The geometrical distortion evolution related to the temperature variation is known as thermo-elastic strain, and it is temperature reversible. The results revealed that the thermo-elastic strains accounted for 50 to 65 % of the total strains developed during the manufacturing of L-shape parts, as shown in Figure 2.7b.

The thermo-elastic strains in asymmetric plates have been measured by digital image analysis (Palerosi and de Almeida, 2007) and linear displacement sensors, such as Linear Variable Differential Transducers (LVDT) (Ruiz and Trochu, 2005a; Radford, 2010), among others.

2.4.3 Tool-part interaction

The tool-part interaction has been quantified by measuring the geometrical distortion obtained after the manufacturing process (total geometric distortion) under different mold conditions (Albert and Fernlund, 2002; Twigg et al., 2004a; de Oliveira et al., 2008). Albert and Fernlund (2002) observed that the total spring-in developed in L-shape parts manufactured by autoclave could be reduced by the use of a fluorinated ethylene-propylene (FEP) film which reduced the friction between the tool and the part.

The tool material's has been demonstrated to have a significant effect in the total geometric distortion. The results showed that the geometrical distortion can be reduced if the used tool had a CTE similar to that of the manufactured composite part (Albert and Fernlund, 2002; Yang et al., 2003; de Oliveira et al., 2008).

Fernlund et al. (2002) measured the tool part interaction evolution during the autoclave manufacturing by a strain gage placed in the tool. The results suggested that the tool and the part presented a perfect adhesion during the manufacturing and a part of the cool-down. The authors stated that the tool-part interaction yielded larger residual strains during the cool-down. Similar results were obtained by Khoun et al. (2011) during the manufacturing of a composite plate by RTM instrumented with FBG.

2.4.4 Others

Viscoelastic behavior

White and Hahn (1993) measured the effect of residual stress relaxation in asymmetric plates

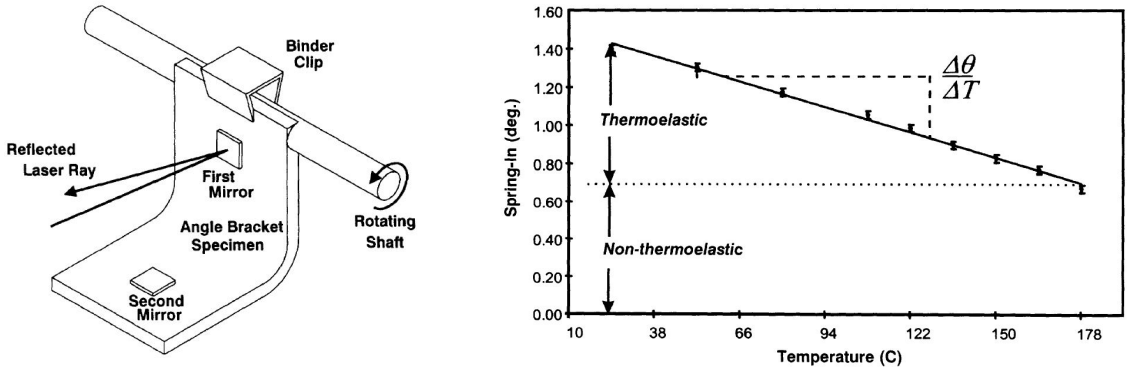

(a) (b)

Figure 2.7 Thermo-elastic strains measurements in L-shape parts Radford and Rennick (2000) : (a) Schematic representation of the experimental set-up and (b) Spring-in evolution versus temperature

by modifying the in-mold processing conditions. Slower cool-down rates enhanced a reductionof 12 % in the plates curvature. This reduction was explained by the stress relaxation experienced by the composite during the in-mold cool-down. Similar results were measured by Unger and Hansen (1993) in graphite fiber reinforced PEEK (polyetheretherketone) asymmetric laminates.

Finally, Cowley and Beaumont (1997) measured the curvature evolution with time in asymmetric plates at room temperature under constrained conditions. The specimens were stored flat to reproduce conditions of constant strain. A 20 % reduction of the warpage was measured after 5000 hours, as shown in Figure 2.8. The warpage reduction was explained by the composite's viscoelastic behavior.

Post-curing

Several authors have observed an increase of the part's distortion after being submited to a free-standing post-curing process (White and Hahn, 1993; Svanberg and Holmberg, 2001; Hubert et al., 2002; Pazdzior et al., 2004). White and Hahn (1993) suggested that this increment could be explained by an additional chemical shrinkage, the loss of moisture and by an increase in the transverse modulus. However, to the best of the author knowledge, none of this hypotheses were validated.

Figure 2.9 shows the spring-in evolution prior and after submitting L-shaped parts to a four-hour free-standing post-curing. Svanberg and Holmberg (2001) stated that this increment was related to the release of "frozen-in" stresses. Their hypothesis relied on the fact that part of the

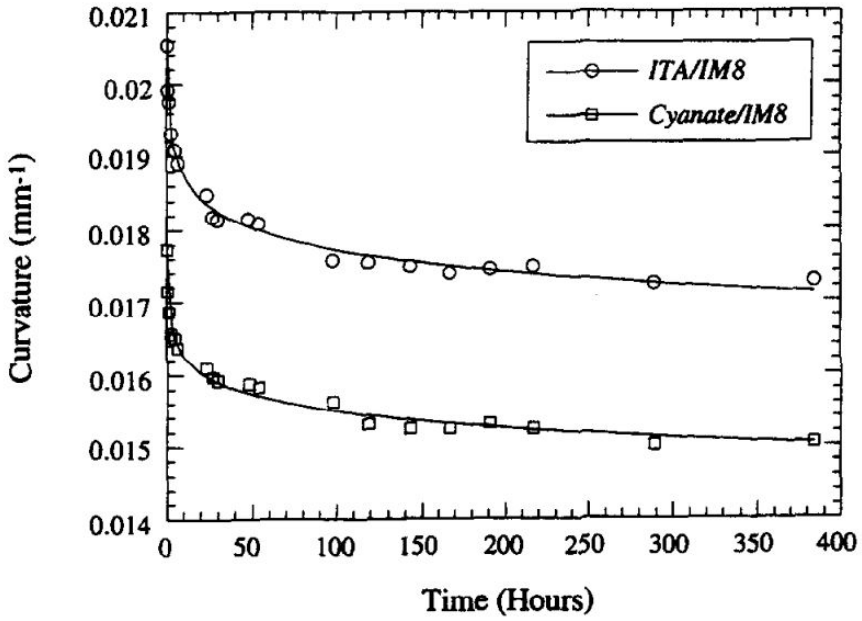

Figure 2.8 Curvature evolution of $[90_2/0]$ asymmetric laminates at room temperature under constrained conditions (Cowley and Beaumont, 1997)

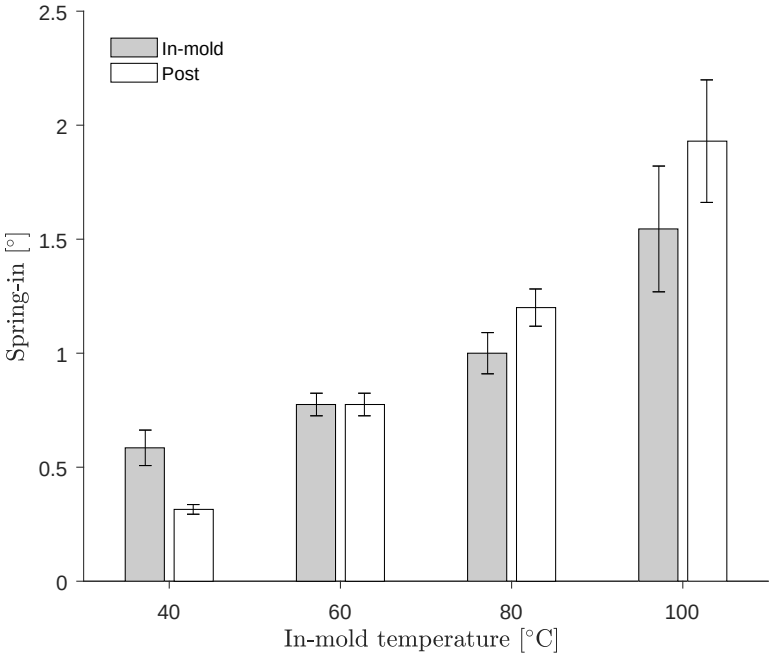

Figure 2.9 Spring-in evolution for curved parts after in-mold manufacturing and free standing post-curing (Svanberg and Holmberg, 2001)

residual stresses developed during the manufacturing process under constrained conditions cannot be released during the cool-down stage since the material evolves from rubbery to a glassy state. These unreleased stresses are considered to be "frozen" into the part (Kominar, 1996). Once the part is reheated free-standing above its glass transition temperature, the "frozen-in" stresses are totally or partially released, thus inducing an increase of the total deformation after post-curing (Kim and Daniel, 2002; Svanberg and Holmberg, 2004a,b; Kim, 2004; Minakuchi, 2015).

2.5 Summary

Table 2.1 and 2.2 recall the main mechanisms inducing residual stresses and the numerical models used to predict them, respectively, during the manufacturing and post-curing (P-C) processes.

Table 2.1 Main mechanisms inducing to residual stresses and geometrical distortion during manufacturing and post-curing processes

	Phenomena	**Contribution during manufacturing**	**Contribution during P-C**
Tool-part interaction	Physical	Significant	–
Chemical shrinkage	Chemical	Significant	Unknown
CTE mismatch	Physical	Significant	–
Viscoelastic behavior	Physical	Unknown	Unknown
"Frozen-in" strains	Phenomenological	Unknown	Unknown

Table 2.2 Numerical models generally used in the literature to predict the residual stresses and geometrical distortion developed during the manufacturing and post-curing processes. Where T= Temperature, t= time, DoC= Degree of cure, FD= Finite differences and P-C= Post-cure

	Elastic	**Viscoelastic**	**Path-Dependent**
Model development	Easy	Complex	Easy
Phenomena	T and DoC	T, t and DoC	T, DoC and "frozen-in" stress
Computational time	Fast	Long	Fast
Implementation	Instantaneous (approximation)	Recursive or FD	Similar to instantaneous
Validity	Unknown	Unknown	Unknown
Accuracy during RTM	Good	Excelent	Good
Accuracy during P-C	Unknown	Unknown	Unknown

CHAPTER 3 OBJECTIVES AND RATIONALE

The general objective of this study was to better understand the geometrical distortion evolution triggered by the residual stresses built-up during the RTM manufacturing and free-standing post-curing of 3D reinforced composites and to develop a numerical tool accounting for the different phenomena involved in the residual stresses generation that could be used for industrial applications. The literature review revealed, in that regard, that

- Residual stresses arising in composites during the manufacturing process can induce a reduction of the part's mechanical performance by matrix cracking, delamination and/or geometrical instability. The coefficient of thermal expansion mismatch between the reinforcement and the resin, the resin's chemical shrinkage and tool-part interaction are known to be the main mechanisms of residual stresses generation during the manufacturing process. The mechanisms involved in the residual stresses built-up over post-curing process must be investigated to better design the manufacturing process.
- Numerical codes have been developed to predict the geometrical distortion triggered by the residual stresses built-up during the manufacturing process. However, the validity, limitations and implementation techniques of the different mechanical models (elastic, viscoelastic and path dependent) are yet to be analyzed.
- Geometrical instability in simple parts developed during manufacturing has been successfully predicted numerically using elastic and viscoelastic models. However, the reasons behind the geometrical instabilities increase resulting from free-standing post-curing are not yet fully understood.

Based on the project objectives and the summary of the litterature survey, three sub-objectives have been defined and led to three published/submitted journal papers, namely

1 **Investigate the physical origins of process-induced residual distortion during the post-curing process.**

  The first objective explors the physical origins of the part's geometrical instability evolution when submitted to different post-curing thermal cycles. Six asymmetric epoxy plates reinforced by three dimensional interlock reinforcement were manufactured using a steel RTM mold. The part's deflection was characterized after the in-mold manufacturing at room temperature by a Linear Variable Differential Transducer (LVDT). The plates were then submitted to several free-standing 30 and 150 minute isotherms at temperatures ranging from 70 to 220 °C. The plate's geometrical deflec-

tion was measured during and after the post-curing process with digital image analysis and the LVDT, respectively.

An article entitled “Viscoelastic distortion in asymmetric plates during post curing” was accepted for publication in “Composites Part A : Applied Science and Manufacturing”. This journal publishes original research on science and technology aspects of composite materials. The author of this thesis wrote 85 % of this paper. Professors M. Lévesque and E. Ruiz and Dr. L. Marcin contributed to the redaction.

2 **Numerical code development for the prediction of geometrical instabilities developed during the RTM manufacturing process.**

The second objective consists in developing a numerical code to predict the residual stresses and geometrical instabilities built-up during the RTM process. Four constitutive laws were implemented into ABAQUS to study their validity and accuracy. Single element simulations examples exposed to thermal and mechanical cycles were used to analyze the validity of the different mechanical models. Finally, the residual stresses and geometrical distortion developed during the RTM manufacturing of asymmetric plates were computed. The numerical results were then compared with the experimental data to assess the accuracy study generated in the first sub-objective.

An article entitled “Numerical analysis of process-induced residual distortions in asymmetric plates : FE-implementation of different constitutive laws” was submitted for publication in “Journal of Composite Materials ” on December, 2017. The author of this thesis wrote 85 % of this paper. The homogenized mechanical properties used in the mechanical model were provided by Thierry Godon and Alice Courtois. Professors M. Lévesque and E. Ruiz and Dr. L. Marcin contributed to the redaction.

3 **Evaluate the developed numerical code for the prediction of geometrical instabilities arising from complex cure cycles processes.**

The third objective investigated numerically the geometrical instabilities evolution during the post-curing process with the numerical code developed during the second sub-objective. First, an asymmetric plate reinforced with 3D interlock fabric was simulated during the RTM manufacturing and free-standing post-curing cycle with elastic and viscoelastic models. The numerical results obtained during and after the post-curing cycles were compared with those measured during the first sub-objective. Then, the spring-in developed in a L-shaped part was simulated during the in-mold RTM manufacturing and free-standing post-curing cycle. The results were then compared with data from literature.

An article entitled “Numerical analysis of viscoelastic process-induced residual distor-

tions during manufacturing and post-curing" was recently accepted for publication in "Composites Part A : Applied Science and Manufacturing". The author of this thesis wrote 85 % of this paper. Professors M. Lévesque and E. Ruiz and Dr. L. Marcin contributed to the redaction.

CHAPTER 4 ARTICLE 1 : VISCOELASTIC DISTORTION IN ASYMMETRIC PLATES DURING POST CURING

M. Benavente, L. Marcin, A. Courtois, M. Lévesque, E. Ruiz (2017).

Accepted at Composite Part A : Applied Science and Manufacturing on September 29th 2017.

Abstract

This study aims at understanding the geometrical instability triggered by the residual stresses generated during the manufacturing and post-curing of composites plates. Asymmetric plates with a [0/90] configuration were manufactured by Resin Transfer Molding (RTM). Manufactured plates were reheated free standing in an convection oven to study their behavior at high temperatures. Digital image analysis was used to monitor the plates curvature evolution with time and temperature. The experimental results of this work demonstrates the impact of the resin's viscoelastic behavior on the geometrical distortion generated by residual stresses in asymmetric plates at high temperatures.

4.1 Introduction

Composite parts are subjected to thermo-chemo-mechanical phenomena during manufacturing that induce residual stresses. Residual stresses are self-balanced stresses that are present in the structure free of any external load or thermal gradient. Their presence can induce matrix cracking, delamination and/or part warpage (Ruiz and Trochu, 2005a; Bayraktar et al., 2012). The Coefficient of Thermal Expansion (CTE) mismatch between the fiber and the matrix, the matrix cure chemical shrinkage and the tool-part interaction are known to be the main causes of the residual stresses generation (Radford and Rennick, 2000; Kim and Hahn, 1989).

The geometrical distortion developed in curved balanced symmetric parts (Radford and Diefendorf, 1993; Svanberg and Holmberg, 2001; Causse et al., 2012) and asymmetric flat plates (White and Hahn, 1992; Ruiz and Trochu, 2005a; Khoun et al., 2011) has been characterized over the years after manufacturing (total warpage) (White and Hahn, 1993; Causse et al., 2012) or during manufacturing (Kim and Hahn, 1989; Ersoy et al., 2005) in 2D laminates. Post-manufacturing measurements have shown that the angle variation, also known as "spring-in" or "spring-forward", developed in curved parts was governed by the composite's anisotropy between the in-plane and through the thickness directions (Radford and Rennick,

2000). On the other hand, the deflection generated in plates with asymmetric lay-up was caused by the residual stresses triggered by the properties mismatch between the plies (Ruiz and Trochu, 2005a; Wisnom et al., 2006; Khoun et al., 2011). The main drawback of the total warpage measurement is that it is not possible to identify the individual contributions of the different phenomena involved during the manufacturing. Strain evolution has been measured during the manufacturing process by Fiber Bragg Grating (FBG) (Khoun et al., 2011; Canal et al., 2015) and strain gages (Wisnom et al., 2006). However, these methods are generally difficult to implement and the interpretation of the results remains a challenge (Ifju et al., 1999; Kim and Daniel, 2002; Canal et al., 2015). Radford and Diefendorf (1993) proposed to measure the shape evolution in corner samples simultaneously with the temperature variation by the use of a laser beam mounted on the sample arm, which enabled the distortion generated by the difference in the CTE between the in-plane and through-the-thickness directions to be estimated. Warpage evolution has been measured simultaneously with the temperature variation in asymmetric plates by a Linear Variable Differential Transducer (LVDT) (Ruiz and Trochu, 2005a) and by digital image analysis (Palerosi and de Almeida, 2007). The influence of the tool part interaction in the final warpage has been studied by modifying the mold material (Cann and Adams, 2001; Kiasat and Mostofi, 2008) or by placing strain gages in the mold (Fernlund et al., 2002). Kiasat and Mostofi (2008) compared the total warpage developed in asymmetric plates manufactured under constrained and free conditions. Their results show that the warpage developed in freely cured plates is more pronounced than that in plates cured under constrained conditions. Kominar (1996) introduced the term “frozen-in” stresses to explain this phenomenon. The author stated that the stresses developed during the in-mold manufacturing cannot be released during the cool-down since the material undergoes from a rubbery to a glassy state. These internal stresses are therefore considered as “frozen” into the part. Svanberg and Holmberg (2001) demonstrated that the “frozen-in” stresses, also known as “constrained-in” stresses, can be totally or partially recovered by heating a free standing plate above its glass transition temperature, thus increasing the part’s total warpage after cool down (Kominar, 1996; Svanberg and Holmberg, 2001; Kim and Daniel, 2002; Kim, 2004; Minakuchi, 2015). To the best of our knowledge, geometrical distortions triggered by the residual stresses built up in composites reinforced by three dimensional (3D) woven fabrics have never been reported.

Most polymers exhibit a viscoelastic behavior, such as stress relaxation (measured stress decreases as a function of time to an applied constant strain) and creep (measured strain increases as a function of time for a constant applied stress) (Schapery, 1969; Lévesque et al., 2008). For most polymers, the viscoelastic behavior is affected by both the degree of cure and temperature (Ferry, 1980; O’Brien et al., 2001; Ruiz and Trochu, 2005b; Courtois

et al., 2016). Figure 4.1 shows a typical stress evolution during a relaxation test at different temperatures. The stabilized relaxation stress corresponds to the fully relaxed behavior at which the stiffness is stabilized over time. Similar behavior can be observed during a creep test (Worgull et al., 2006).

Unger and Hansen (1993) studied the effect of the residual stresses relaxation in unsymmetrical thermoplastic laminates. They observed that the cooling rate under constrained conditions had a direct impact on the residual stresses relaxation, thus modifying the plate's final curvature. Cowley and Beaumont (1997) recorded the curvature evolution at room temperature under constrained conditions for cyanate thermoset and ITA thermoplastic asymmetric composite specimens. The residual stresses relaxation over 5000 hours led to a 20% reduction of the geometrical distortion. To the best of our knowledge, no published study related the curvature evolution of asymmetric composite plates constituted of an epoxy resin to viscoelastic behavior.

The purpose of this work was to investigate the physical origins of process-induced residual distortion in asymmetric plates during the post-curing process. The underlying hypothesis is that residual distortion generated during the post-cure under free-standing conditions can be explained through viscoelastic effects, alone. To that end, manufacturing process histories involving thermo-mechanical coupling were carefully designed to capture and clearly demonstrate viscoelastic effects.

The paper is organized as follows. Section 4.2 deals with the background on process-induced distortion in composites while the materials and the experimental methodology are presented in Section 4.3 and 4.4, respectively. Finally, the results and discussion are presented in Section 5.5.

4.2 Viscoelastic effects in manufacturing process

Process induced distortion can result from either reversible or irreversible thermo-mechanical phenomena (Radford and Rennick, 2000). Reversible distortion in asymmetric plates typically results from incompatible stress-free strains, referred herein as eigenstrains, induced by the CTEs mismatch in the in-plane direction. Moisture absorption can also result in incompatible eigenstrain (Palerosi and de Almeida, 2007). Tool-part interaction and chemical shrinkage can induce permanent distortion, also known as irreversible distortion (Radford and Rennick, 2000; Kiasat and Mostofi, 2008).

For the sake of illustration, consider Figure 4.2 that schematizes an hypothetical temperature history that could be applied to a free standing and fully cured composite part. The figure

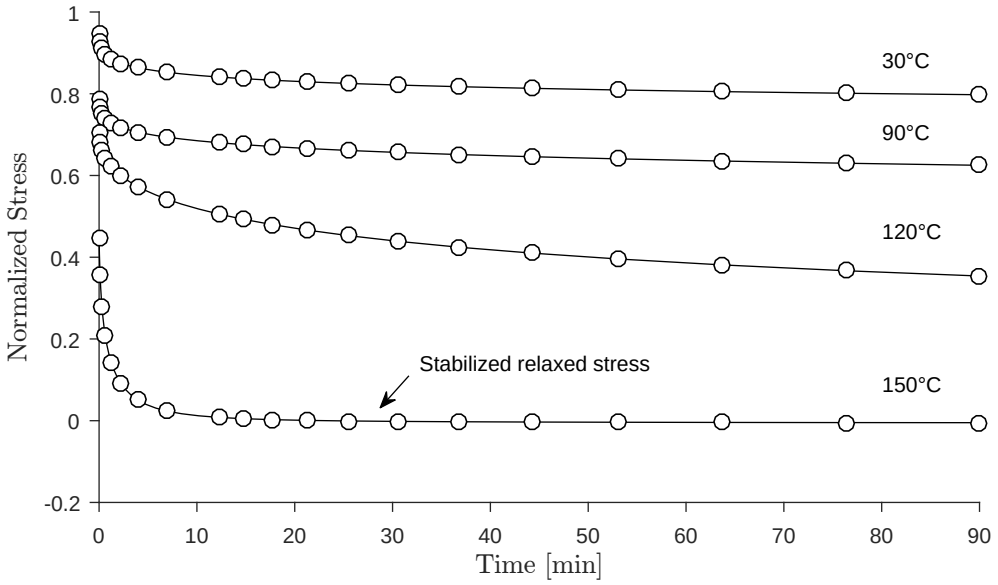

Figure 4.1 Stress relaxation for an epoxy resin at various temperature below its glass transition temperature (T_g=155 °C) (Courtois et al., 2016)

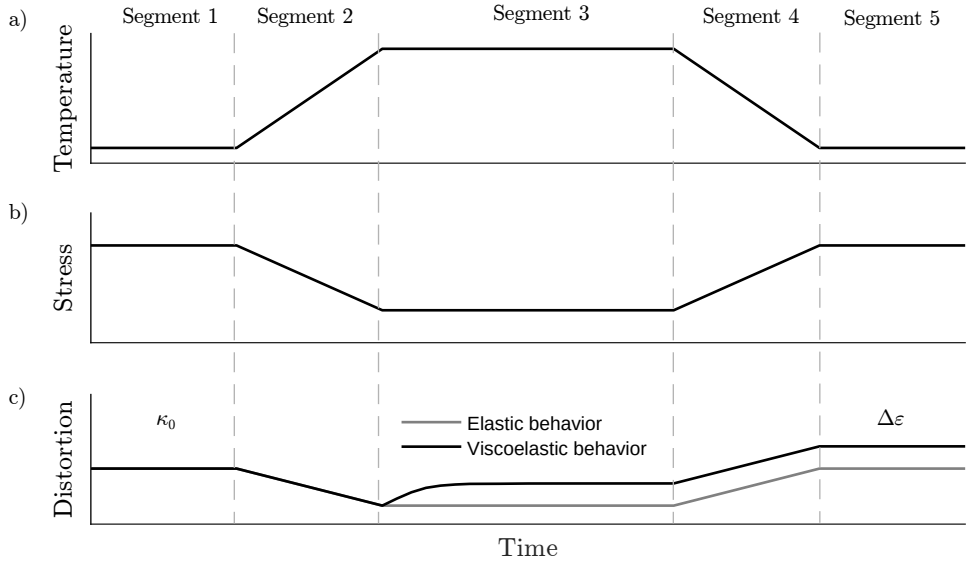

Figure 4.2 Schematic representation of the residual stresses and deformation during free standing thermal cycle in a completely cured plate. a) Temperature evolution over time, b) Theoretical stress evolution with temperature and time and c) Theoretical distortion evolution with temperature and time for an elastic (gray) and viscoelastic (black) material

also shows the overall internal stresses build up in the matrix phase (that has to be balanced by a residual stress field in the fibers) as well as the resulting overall distortion (that could be, for example, the curvature into a free standing plate that was molded flat). The post-cure cycle can be divided into five distinct phases, namely

- **Segment 1 :** A first phase where the temperature is held constant. The initial stresses and strains correspond to the residual stresses built up during the manufacturing process.
- **Segment 2 :** A heating phase where distortion as well as matrix internal stresses decrease as the temperature increases. This can be explained as follows. Over the curing process, permanent strains built up by the tool part interaction and chemical shrinkage. The fully cured plate was then cooled down to room temperature, thus introducing reversible residual stresses that increase the plate's distortion. Heating the plate again brings it closer to its flat curing stress state.
- **Segment 3 :** An isothermal phase where the temperature was held constant. In this phase, if the material was linearly elastic, both the internal stresses and distortion would remain constant (gray). However, if the temperature was sufficiently high, the matrix' viscoelastic behavior could be triggered with two consequences. On one hand, internal stresses would be redistributed between the matrix and the fibers as the matrix becomes more compliant. However, when considering that the residual stresses distribution depends on the stiffness ratio between the fibers and matrix (and will eventually stabilize even if the fibers were to be infinitely rigid) and the fact that this ratio was already very large for carbon-epoxy composites, such redistribution was expected to be negligible. On the other hand, the matrix' internal stresses would induce creep strains which, for shear dominated distortion, would increase the part's distortion over time, as shown in Figure 4.2.
- **Segment 4 :** A cool down phase that occurs sufficiently rapidly to avoid any viscoelastic effects. During this phase, residual stresses and distortion build up linearly with the temperature variation.
- **Segment 5 :** A final phase where the temperature is held constant. The final distortion shows that accounting for viscoelastic effects yields, in theory, larger final distortion ($\Delta\varepsilon$) during the post-cure than assuming a linearly elastic behavior, for the same internal residual stresses.

Based on the hypothese presented above, creep strains in the matrix resulting from free-

standing post-curing would increase the final distortion of an asymmetric composite laminate. On the other hand, stress relaxation could occur during post-curing under constrained conditions, thus reducing the part's final distortion, as observed experimentally by Cowley and Beaumont (1997).

The experimental methodology developed in this work has been specifically designed to capture and demonstrate such effects on asymmetric plates reinforced by 3D interlock fabric.

4.3 Materials and processing

A 3D woven interlock reinforcement with IM10 carbon fibers (Hexcel Fabrics) having an areal density of 3475 g/m^2 was studied. Each reinforcement ply was composed of four interlock layers. The reinforcement's architecture was such that 70 % of the fibers (in mass) was aligned along the warp direction. A commercial Diglycidyl Ether of Bisphenol F (DGEBF) one component epoxy resin from Cytec was used as matrix.

Longitudinal injections were carried out in a rectangular RTM steel mold with an internal cavity of 455 mm × 145 mm × 6.7 mm to yield laminates having volume fractions of 58 %. Two plies were stacked to obtain a [0/90] lay up configuration. Three micro thermocouples were embedded into the reinforcement at the middle of the mold at three different positions, namely : the top surface, the bottom surface and between the plies, as shown in Figure 4.3. Once the preform was draped, the mold was closed and preheated at 160 °C. The epoxy system was heated above 100 °C to reduce its viscosity and degassed for 30 minutes prior to the injection. The resin was then injected with a constant flow rate of 20 ml/min, followed by a compaction pressure of 7 bars to reduce porosity (Pupin et al., 2017). A cure cycle with two dwell phases of one hour at 160 °C and two hours at 180 °C was adopted to ensure complete resin curing. The plates were then cooled inside the mold until the laminates center reached 100 °C. Finally, the plates were released from the mold and cooled by natural convection down to room temperature.

Resin samples from composite plates were analyzed using a Q-2000 Modulated Differential Scanning Calorimeter (M-DSC) from TA Instruments to verify their complete polymerization. M-DSC analyses were carried out using aluminum pans hermetically sealed. A heating ramp of 2 °C/min, starting at 30 °C and up to 290 °C, was applied to measure the resin's total enthalpy during curing and the samples residual enthalpy. The plates degree of cure was calculated as the enthalpy measured in cured plates divided by the total enthalpy measured in the uncured resin. The average residual enthalpy measured in the plates after the manufacturing process was 2.7 ± 0.3 J/g. The results revealed that the plates were completely cured with a degree

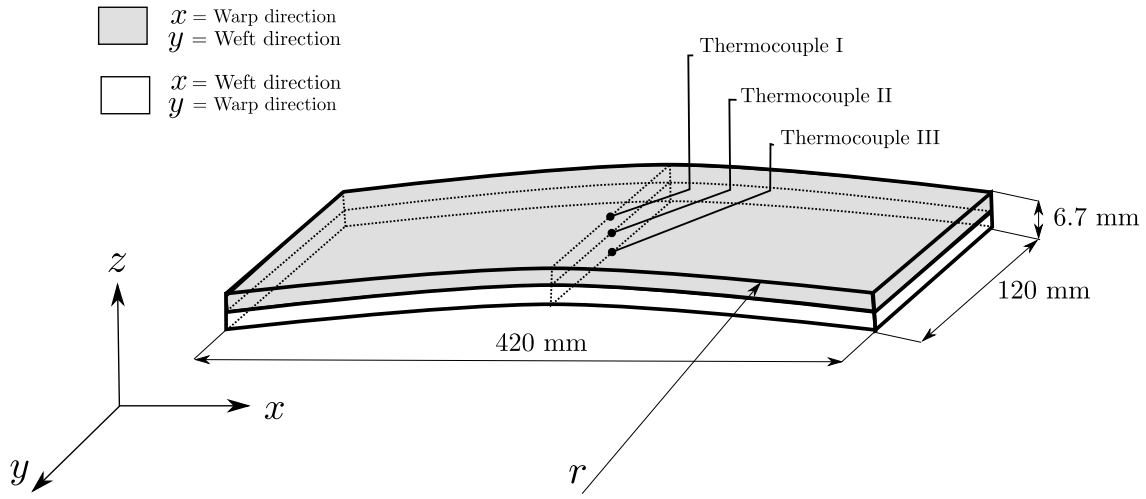

Figure 4.3 Schematic representation of the embedded thermocouples, lay-up configuration and the geometrical instability after the manufacturing of asymmetric plates

of cure of 99.2 %. The plates were finally cut with a diamond saw to dimensions of 410 mm × 120 mm × 6.7 mm.

4.4 Experimental procedure

The geometrical distortion of six plates was characterized using two measurements techniques. An electronic Linear Variable Differential Transformer, LVDT (from CDI) was used to measure the plates post manufacturing deflection at room temperature. A digital monochrome camera set to acquire images of 2448 pixels × 2048 pixels, from Point Grey, was used to monitor the plates distortion as a function of time and temperature.

The plates were submitted to the thermal history shown in Figure 4.4 and explained in the sequel. After the manufacturing, the plates deflection was measured by the LVDT at 42 locations (one per cm) along their middle longitudinal axis. The least-squares method was used to fit the best arc into the obtained points cloud to compute the curvature, $K = 1/r$, where r is the curvature radius.

The six plates were subsequently reheated free-standing during 30 minutes in a forced convection oven preheated at 70 °C. The plates were then removed from the oven and cooled-down by natural convection to room temperature. The plates deflection were measured with the LVDT. Following the same procedure, the plates were submitted to a total of fourteen isotherms each, between 80 °C and 220 °C, as shown in Phase I in Figure 4.4. Phase I was designed to identify the temperature at which the viscoelastic effects became significant.

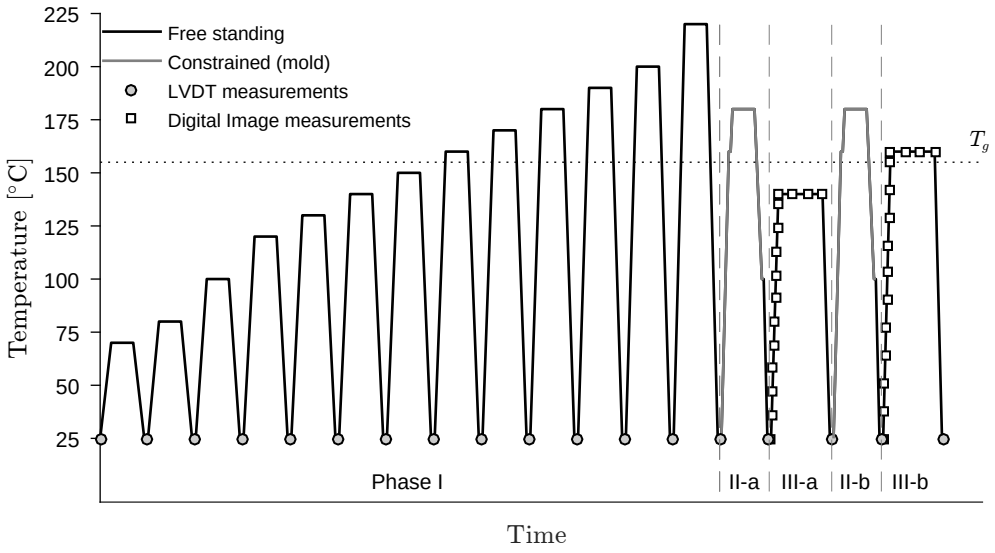

Figure 4.4 Schematic representation of the studied thermal cycle for plate C. The free standing condition refers to the thermal cycle carried out in the oven. The constrained condition refers to a plate heated inside a closed mold

Once the full measuring - heating - cooling cycle was completed, the six plates were placed, individually, inside the open manufacturing mold and reheated up to the resin's glass transition temperature at 160 °C. The mold was then closed and heated up to 180 °C. The plates were submitted to a 30-minute dwell at 180 °C inside the closed mold, as shown in Phase II-a in Figure 4.4. The mold was then cooled-down by a cold water circuit until the plates' center reached 100 °C. Phase II was designed to yield a different internal stresses distribution generated by heating the mold under constrained conditions after submitting the plates to free-standing isotherms. The plates were then removed from the mold and let naturally cool down to room temperature. Finally, the plates' distortion was measured by the LVDT.

The plates were then placed inside the preheated oven and the digital camera was aligned horizontally with respect to the sample, capturing the whole longitudinal edge. Three lamps were used to ensure proper lightening. The plates' longitudinal edges were painted in white and a black painted aluminum plate was placed inside the oven to increase the images contrast. A ruler was placed in the oven door to establish the correlation between the pixels and physical length. The plates' distortion evolution was monitored by taking one picture per second during the heating phase and a 150 minutes isotherm at the temperatures listed in the first column of Table 4.1. The plates were subsequently removed from the oven and cooled down to room temperature. The plates longitudinal distortion was measured by the LVDT. Four

Table 4.1 Thermal cycle followed by the six asymmetrical plates during the 150 minutes isotherms

	Phase III-a First 150 min isotherm	**Phase II-b** Second mold constrained	**Phase III-b** Second 150 min isotherm
Plate A	130°C	Yes	140°C
Plate B	130°C	Yes	160°C
Plate C	140 °C	Yes	160°C
Plate D	150°C	No	150°C
Plate E	150°C	No	150°C
Plate F	180°C	Yes	180°C

out of the six studied plates were placed back inside the manufacturing mold, Phase II-b. The plates were then placed inside the oven and submitted to a 150 minutes isotherm at the temperatures listed in the third column of Table 4.1. Finally, plates D and E were submitted to two consecutive 150 minutes isotherms at 150 °C, as shown in Table 4.1.

4.5 Results and discussion

4.5.1 Total curvature

The plates curvature calculated during phase I reported in Figure 4.4 are presented in Figure 4.5. The results presented in this section were normalized by the plates post-manufacturing curvature, K_0. The error bars represent 95% confidence intervals on mean for the six samples. Three regions can be identified from Figure 4.5, where T_c corresponds to the isotherm temperature, namely :

- **Region i** ($T_c << T_g$), from 20 to 130 °C. The figure shows that the combination of temperature and creep duration did not yield significant curvature changes. This is the reversible phase.
- **Region ii** ($T_c < T_g$), from 130 to 160 °C. This transition region shows that, as temperature increases, the dwell time is sufficient to allow the matrix to creep. The figure shows that, as temperature increases, the amount of creep for a fixed duration of 30 minutes increases.
- **Region iii** ($T_c \geq T_g$), above 160 °C, which corresponds to the resin's rubbery state. In this region, the dwell time is larger than that required to reach a stable creep strain.

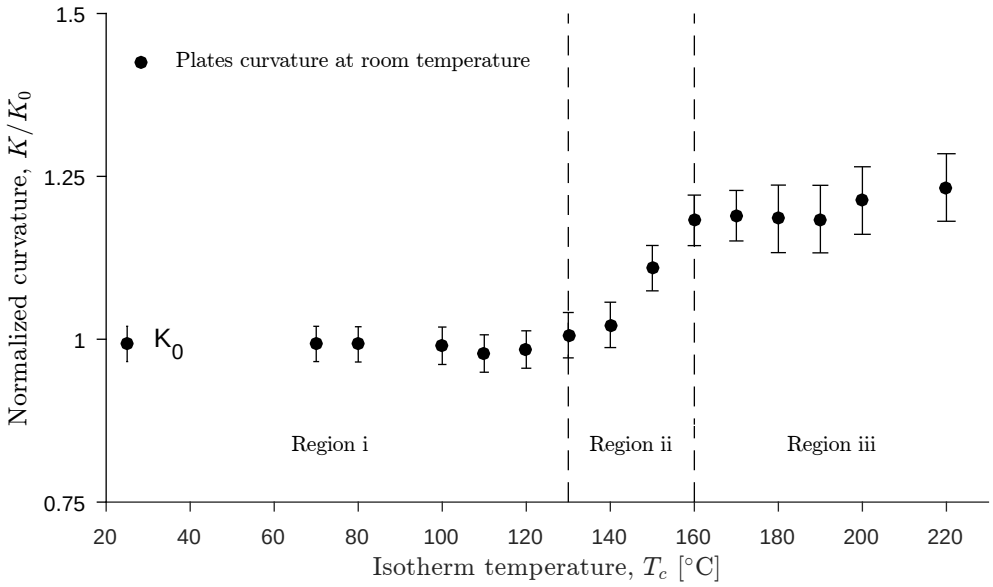

Figure 4.5 Curvature at room temperature of [0/90] plates after being submitted to 30 minutes at isotherm temperature, T_c (Phase I) normalized by the plates post-manufacturing curvature

Thus, submitting the plate to higher temperature does not increase the amount of curvature any further for a dwell time of 30 minutes.

The plates curvature at room temperature after having been constrained in the mold, during Phase II in Figure 4.4, are presented in Table 4.2. The table reveals that the normalized curvature decreased by 4 % and 6 % after the plates underwent, respectively, a first and a second temperature cycle constrained in the mold. These results suggest that the internal stresses relaxed over time when the plates were constrained inside the mold, thus decreasing the plates curvature.

Figure 4.6 shows a comparison of the curvature measured at room temperature during Phase I and III in Figure 4.4. The following experimentally measured curvatures were normalized by that measured prior to the thermal analysis to better compare the effects of temperature and isotherms duration on warpage. The curvatures obtained after submitting the plates to

Table 4.2 Normalized curvature measured at room temperature after the fabrication and after being cooled constrained in the mold once (Phase II-a) or twice (Phase II-b)

	Fabrication	**Phase II-a**	**Phase II-b**
Normalized curvature	1 ± 0.02	0.96 ± 0.02	0.94 ± 0.02

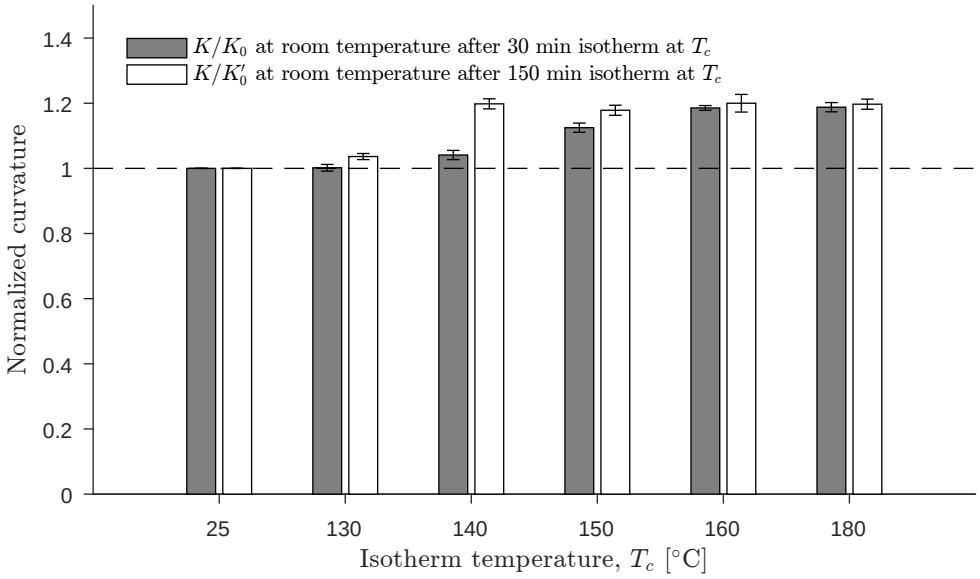

Figure 4.6 Comparison of the normalized curvature at room temperature of a [0/90] plate after heating at isotherm temperature, T_c, for 30 minutes (Phase I) or 150 minutes (Phase III)

the 30 minutes isotherms from Phase I were normalized by the curvatures measured after manufacturing, K_0. The curvatures measured after the 150 minutes isotherms of Phase III were normalized by the curvatures measured once the plates were cooled down inside the mold (Phase II). Figure 4.6 shows that maintaining the temperature at 150 °C for up to 150 minutes is sufficient to reach the same curvature as that obtained for a dwell time shorter than 30 minutes above the glass transition temperature. For isotherms above the glass transition temperature (160 °C and 180 °C), the curvatures measured after the 150 minutes isotherm were similar to those measured after 30 minutes at the same temperature. Thus, the stabilized creep strain is achieved within the first 30 minutes above the glass transition temperature and submitting the plate to a longer isotherm does not increase the amount of curvature.

4.5.2 Time-temperature deformation

Figure 4.7 shows the curvature and the temperature measurements on plate D during the first 150 minute isotherm at 150 °C (Phase III-a in Figure 4.4). The figure shows that the curvature decreased proportionally with the temperature during the temperature ramp. Then, during the isotherm, the temperature is sufficiently high to accelerate the creep phenomenon so that a stabilized state was obtained within the first 100 minutes. Figure 4.7 also shows that the reversible thermo-elastic distortion accounted for almost 95 % of the total curvature de-

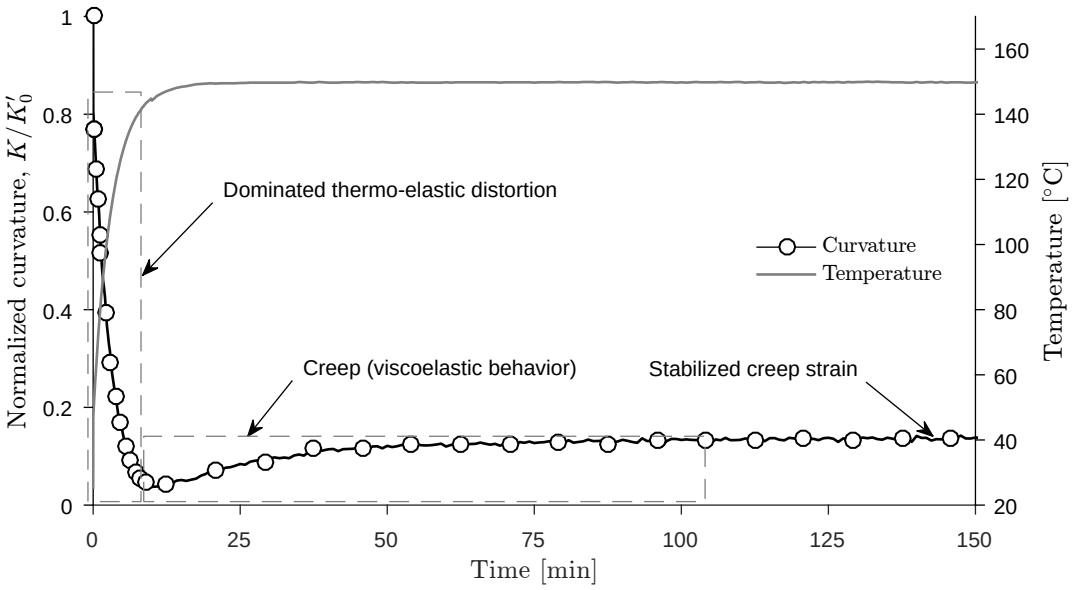

Figure 4.7 Curvature evolution of plate D during the first 150 minutes isotherm at 150°C showing its viscoelastic behavior

veloped in [0/90] asymmetric plates. Finally, although the contribution of irreversible sources (chemical shrinkage and tool-part interaction) to residual stresses was much less significant than that of reversible sources (CTE), important creep strains were measured over time when the plate was submitted to a temperature near its T_g. These creep strains, that might be due to the fact the resin's stiffness significantly reduced near T_g, increased the resulting curvature further.

The same experiment was performed for temperatures of 130, 140, 150 and 160 °C. Figure 4.8 shows the curvatures evolution for these experiments. The plates heated at 140 °C and 150 °C, respectively, reached a stabilized creep strain within the first 100 minutes, while it took less than 20 minutes for the plates heated at 160 °C. Above the resin's glass transition temperature, the matrix reaches the rubbery state, thus accelerating the creep behavior. Finally, the curvatures of the plates heated at 130 °C increased by 6 % during the 150 minutes, suggesting that the viscoelastic effect is less significant. Consequently, a longer time would be needed to reach the stabilized creep strain at this temperature, or below it.

4.5.3 Reversible distortion

Figure 4.9 presents the curvature presented in Figure 4.8 with the temperature evolution during the heating phase and the 150 minutes isotherms. A linear behavior in the curvature was observed during the heating ramps due to the reversible thermo-elastic distortion, related

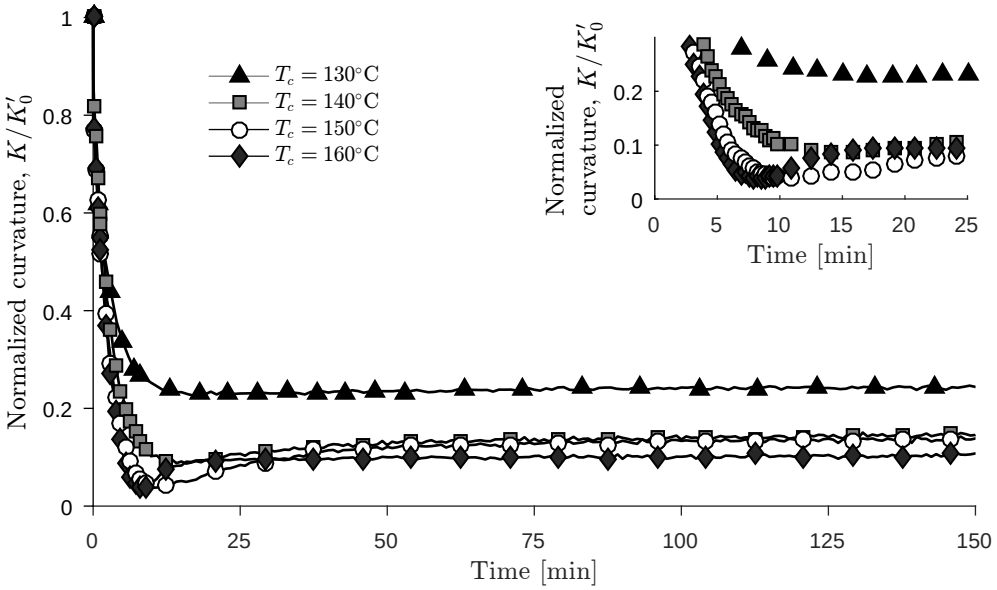

Figure 4.8 Viscoelastic behavior of [0/90] plates submitted to 150 minutes isotherms at different temperatures (Phase III). The inset shows the enlarged viscoelastic behavior within the first 25 minutes at different isotherm temperatures

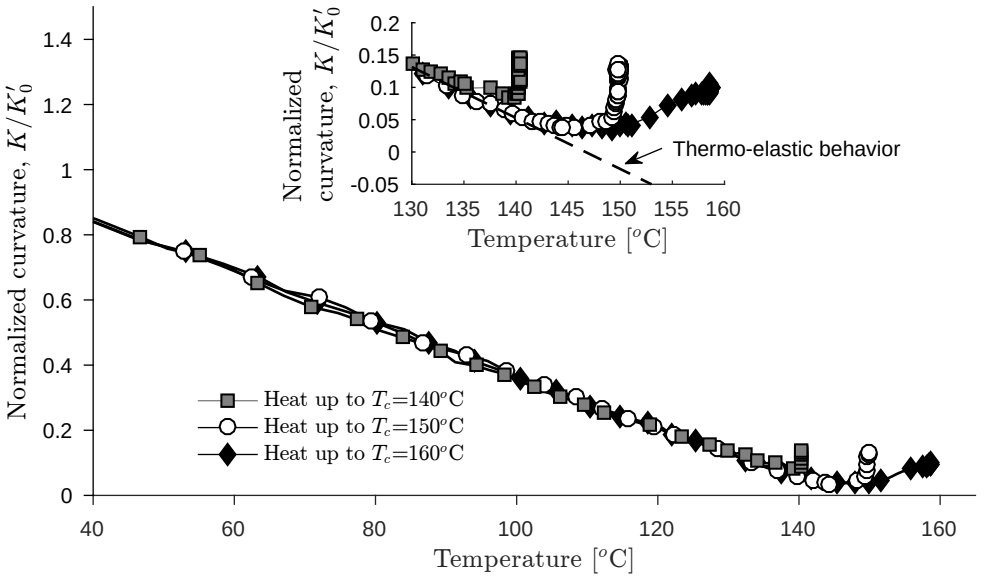

Figure 4.9 Curvature evolution of [0/90] plates during 150 minutes isotherm at different temperatures (Phase III). Inset : Thermo-elastic and creep behavior for different isotherm temperatures from 130 to 160 °C

to the coefficient of thermal expansion, from room temperature to 140 °C.

The figure also shows that the deflection increased when the plates were heated above 145 °C. The results suggest that the creep strains triggered by the viscoelastic behavior were significantly more important than those inducing reversible distortion related to the CTE above 145 °C. This phenomenon was more accentuated above 150 °C.

Figure 4.10 shows the thermo-elastic behavior of plates D and E for two consecutive 150 minutes isotherms at 150 °C. During the first cycle (Phase III-a from Figure 4.4) the curvature decreased linearly from room temperature to 140 °C. However, as seen from Figure 4.9, the plates curvature increased when they were heated above 145 °C. In addition, the plates exhibited a 20 % increase in curvature at room temperature after being submitted to the first isotherm. These results confirmed that the deformation occurring at high temperature (from 145 °C to 150 °C) corresponds to a mechanical deformation caused by the viscoelastic creep of the matrix being thermally irreversible.

The plates were then reheated to 150 °C for 150 minutes. The thermo-elastic behavior was found to be the same for the two isotherms (Phase III-a and b from Figure 4.4) from room temperature to 140 °C. Submitting the plate to high temperature for an extended period (Phase III-a) did not modify its reversible thermo-mechanical response (Phase III-b). Note that no further creep strains were measured during the second isotherm, thus confirming that the stabilized creep strain was achieved during the first isotherm at 150 °C.

Figure 4.10 also shows that a strain-free state was achieve during the first thermal cycle at 145 °C. However, during the second thermal cycle (Phase III-b), the plate presented a measurable curvature at the same temperature. This result suggests that the strain-free temperature was modified during the thermal cycles.

4.6 Conclusion

In this study, a digital image analysis was used to measure the geometrical distortion encountered in asymmetric plates during the post-curing process. The plates curvature was characterized over time and temperature in completely cured asymmetric [0/90] laminates. The plates geometry was monitored during temperature ramps and isotherms under free-standing condition. A linear evolution of the curvature with the temperature was measured during the plates heating, revealing the thermal dependence on the residual stresses (reversible distortion).

A 20 % increase in the curvature was observed after heating the plates free standing above their glass transition temperature for short times. For lower temperatures, $T_c > T_g - 20$ °C,

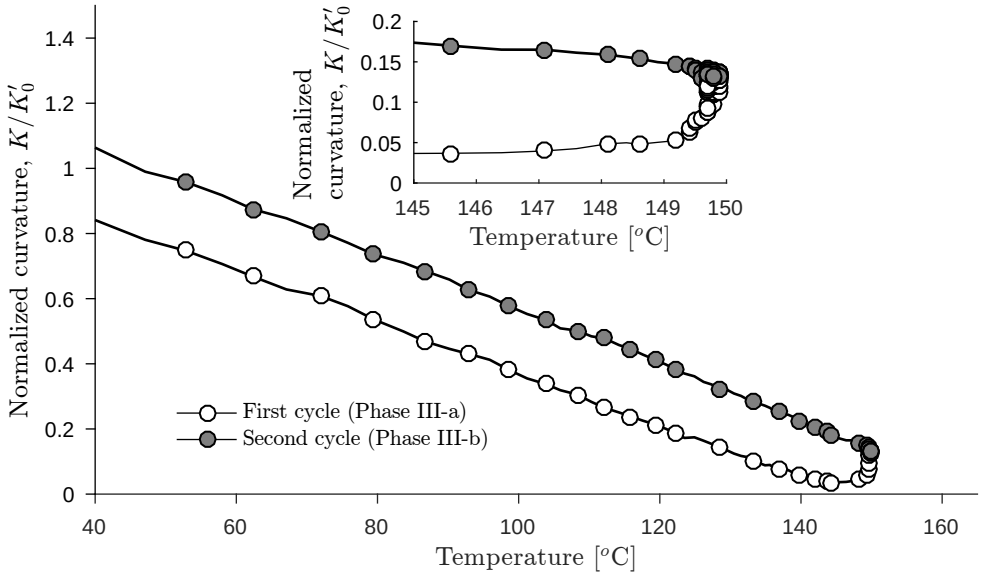

Figure 4.10 Thermo-elastic and creep behavior of plates D and E during two consecutive 150 minutes isotherm at 150°C (Phase III-a and b). The inset shows the curvature evolution zoom-in from 145 to 150 °C

a longer exposure time was needed to achieve the stabilized creep strain. The results showed a reduction of 4 to 6 % of the total curvature when the plates were submitted to in-mold constrained thermal cycle. The reduction of the curvature was explained by the internal stress relaxation occurring inside the plate by the imposed strain by the mold. Finally, it is important to note that although creep strains and stress relaxation are caused by the composite's viscoelastic behavior, creep strains yielded larger curvature (as shown during the free-standing thermal cycle from Phase I and III), while stress relaxation reduced it (as occurred during the in-mold thermal cycle from Phase II).

In previous works, this effect was explained by "frozen-in" strains generated during the manufacturing. Those "frozen-in" strains could be released when the plates were heated above the composite's glass transition temperature. However, the results presented in this article suggest that this increment in the curvature is caused by the composite's viscoelastic behavior at high temperature. The viscoelastic effect was proved to have an important impact on the plates curvature, even for temperatures below the glass transition temperature. These results therefore suggests that "frozen-in" strains can be explained through viscoelastic effects.

In conclusion, viscoelastic behavior can be triggered for manufacturing process where there is an out-of-mold post-cure. This situation can increase irreversibly the geometric distortion to up to 20 %. A viscoelastic model is then needed to accurately predict the geometric distortion

caused by the residual stresses.

Acknowledgments

The authors would like to acknowledge Safran Group and the Canada Research Chair program for the financial support and for providing the resin and reinforcements used in this work. The National Science and Engineering Research Council (NSERC) of Canada, the Fonds Québécois pour la Recherche sur la Nature et les Technologies (FQRNT), the Canada Foundation for Innovation (CFI) and of the Ministère de l'Éducation du Québec are gratefully acknowledge for their contribution with the infrastructure and expenses of the composite laboratory. The authors also thank the contribution of Jesus Fernandez and Jon Zubimendi for their technical support.

CHAPTER 5 ARTICLE 2 : NUMERICAL ANALYSIS OF PROCESS-INDUCED RESIDUAL DISTORTIONS IN ASYMMETRIC PLATES : FE-IMPLEMENTATION OF DIFFERENT CONSTITUTIVE LAWS

M. Benavente, L. Marcin, T. Godon, A. Courtois, M. Lévesque, E. Ruiz (2017).

Submitted to Journal of Composite Materials on December 6th 2017.

Abstract

A review of the elastic, viscoelastic and path-dependent constitutive laws and their implementation into a FE program are presented. The validity of the models was analyzed by computing the stress and strain evolution during single elements simulations examples exposed to thermal and mechanical cycles constituted of creep and relaxation periods. The residual stresses and geometrical distortion developed during the manufacturing of an asymmetric plate reinforced by a 3D interlock fabric by RTM were computed using four different models available in the literature and compared with experimental results. Finally, the limitations and accuracy of the implemented models were presented.

5.1 Introduction

Residual stresses built-up during the manufacturing of composite structures are known to induce geometrical distortions and/or matrix delamination (Ruiz and Trochu, 2005a). The matrix' chemical shrinkage during its curing, the coefficient of thermal expansion mismatch between the reinforcement and the matrix, as well as the tool-part interaction are known to be the main causes of the residual stresses generation Radford and Rennick (2000); Wisnom et al. (2006). The last thirty years witnessed a growing interest in the modeling of laminated composites properties evolution over the manufacturing process to assess the residual stresses build-up Bogetti and Gillespie Jr (1992); Fernlund et al. (2002); Canal et al. (2015). Elastic, viscoelastic and path-dependent models have been developed to describe the mechanical properties evolution with the degree of cure and temperature variations during the manufacturing processes Zobeiry (2006); Ding et al. (2016a); Baran et al. (2016). Johnston (1997) proposed a Cure Hardening Instantaneous Linear Elastic (CHILE) model to represent the resin's stiffness evolution with the degree of cure and temperature. Several authors have adopted CHILE models to predict satisfactorily the geometrical distortion developed during

manufacturing Ruiz and Trochu (2005a); Khoun et al. (2011); Causse et al. (2012). However, the main limitation of this approach lies in the fact that the matrix exhibits a viscoelastic behavior for most of the process. Elastic models, alone, cannot account for the stress relaxation occurring at the processing temperature and over the resin's degree of cure evolution.
Degree of cure- and temperature-dependent viscoelastic models have been developed for epoxy resins used in aerospace composites O'Brien et al. (2001); Ruiz and Trochu (2005b); Courtois et al. (2016). Early viscoelastic analyses showed that stress relaxation can occur during the manufacturing and cool-down stages Wang et al. (1992); White and Hahn (1992); Kim and White (1997). However, their use in the literature has been limited by the fact that an extensive material characterization and a complex numerical implementation are required.
Svanberg and Holmberg (2004b) introduced a modified phenomenological path dependent model that accounted for the stresses evolution during post-curing. Svanberg and Holmberg (2004a) observed that curved parts experienced an increase of the total spring-in angle when submitted to free-standing post curing above their glass transition temperature. This phenomenon was explained by the presence of "frozen-in" residual stresses developed during the manufacturing under constrained conditions. Benavente et al. (2017a) have recently shown that "frozen-in" stresses were in fact viscoelastic creep strains.
This paper compares distortion predictions resulting from two elastic, a viscoelastic and a path-dependent implementation strategies over the whole manufacturing process. The underlying objective was to rigorously discriminate the models physical relevance when submitted to complex thermo-mechanical load histories. The models predictions and limitations were exemplified first on single element simulations where complex thermo-mechanical histories were applied. As a demonstration case, the models were then used to simulate the Resin Transfer Molding (RTM) manufacturing of asymmetric plates reinforced by three-dimensional (3D) interlock fabric composites. Finally, the numerical predictions obtained with the different models were compared to experimentally measured distortion reported in a previous work Benavente et al. (2017a).
The paper is organized as follows : The theoretical background for the numerical methodology and the main constitutive laws used in the literature are recalled. The experimental methodology and the models implementation strategies are then presented. The results and discussion conclude this work.
The modified Voigt notation has been adopted to represent tensors. Symmetric second-order tensors were expressed as six component vectors and symmetric fourth-order tensors were expressed as 6×6 matrices. Scalar quantities were denoted by light-faced letters (i.e., a, α, A), second order tensors were represented by boldfaced lowercase Greek letters (i.e., $\boldsymbol{\sigma}$) while

fourth-order tensors were represented by boldfaced capital Roman letters (i.e., $\mathbf{C}$).

5.2 Theoretical background

A sequentially modular approach was proposed by Loos and SpringerLoos and Springer (1983) to simulate the thermo-chemo-mechanical phenomena involved in the manufacturing of composites. The approach consisted first in running a coupled thermo-chemical model yielding the temperature and degree of cure distribution within the part as a function of time. These temperature and degree of cure fields as a function of time were sequentially input as solution-independent conditions into a mechanical model where the composite's properties evolved as a function of temperature and degree of cure (and thus time).

5.2.1 Coupled thermo-chemical models

Heat transfer and cure kinetics models were combined by numerous authors based on the energy conservation law (Bogetti and Gillespie Jr, 1992; Kim and White, 1997; Joshi et al., 1999) and led to

$$\rho_c \zeta_{pc} \frac{\mathrm{d}T}{\mathrm{d}t} = \frac{\mathrm{d}}{\mathrm{d}x_i}\left(\kappa_{ij}\frac{\mathrm{d}T}{\mathrm{d}x_j}\right) + \dot{Q}_r \qquad \text{(no sum on } c \text{ index)} \tag{5.1}$$

where ρ_c, ζ_{pc} and κ were the composite's density, specific heat at a constant pressure and thermal conductivity tensor, respectively. $\dot{Q}_r$ represented the internal heat generation and was computed as

$$\dot{Q}_r = \rho_r \left(1 - V^f\right) H_r \frac{\mathrm{d}\alpha}{\mathrm{d}t} \tag{5.2}$$

where ρ_r was the resin's density, V^f was the fabric's volume fraction, H_r was the total reaction's enthalpy and $\mathrm{d}\alpha/\mathrm{d}t$ was the kinetic's reaction rate. The resin's kinetic has been generally calculated by the Kamal-Sourour phenomenological model as

$$\frac{\mathrm{d}\alpha}{\mathrm{d}t} = \left(k_1 + k_2\alpha^m\right)(1-\alpha)^n F(\alpha) \tag{5.3}$$

where m and n were a material constant and k_1 and k_2 were the chemical reaction rate constants described by Arrhenius equation as

$$k_i = A_i \exp\left(\frac{-E_i}{RT}\right) \tag{5.4}$$

where A_i, E_i, R and T were the Arrhenius constant, the Arrhenius activation energy, the ideal gas constant and the temperature, respectively.

$F(\alpha)$ was an empirical formula that accounted for diffusion phenomena, and for a DGEBF epoxy resin was expressed byPupin et al. (2017) as

$$F(\alpha) = \frac{1}{1 + \exp(B_1(\alpha - B_2))} \tag{5.5}$$

where B_1 and B_2 were material constants.

5.2.2 Mechanical models

Non-mechanical strains

The chemical shrinkage of thermoset matrices was modeled by Khoun et al. (2010) as a temperature independent linear relationship between the matrix volume change and the degree of cure as

$$\beta^r = \begin{cases} 0 & \alpha \leq \alpha_{gel} \\ (\sqrt[3]{1 + V_s^r} - 1)\alpha_1 & \alpha > \alpha_{gel} \end{cases} \tag{5.6}$$

where β^r was the resin's coefficient of chemical shrinkage, V_s^r was the resin's volume variation caused by the chemical shinkage, α_{gel} was the degree of cure at which the resin transformed from a viscous liquid to an elastic rubbery state and $\alpha_1 = \frac{\alpha - \alpha_{gel}}{1 - \alpha_{gel}}$.

Composite's longitudinal and transverse chemical shrinkage strains have been determined for UD laminates using the Chamis equations by Nielsen (2012) as

$$\beta_1^c = \frac{\beta^r E^r (1 - V^f)}{E^f V^f + E^r (1 - V^f)} \tag{5.7a}$$

$$\beta_2^c = \beta_3^c = (\beta^r + \nu_{12}^r \beta^r)(1 - V^f) - (\nu_{12}^f V^f + \nu_{12}^r (1 - V^f))\beta_1^c \tag{5.7b}$$

where β_1^c and β_2^c were the composite's chemical shrinkage in the longitudinal and transverse direction, respectively. E^r and E^f were the resin and fibers Young's modulus and ν_{12}^r and ν_{12}^f were the resin and fibers Poisson's ratio, respectively.

The coefficient of thermal expansion in composites has been modeled as a function of the glass transition temperature by Svanberg and Holmberg (2004b) as

$$\boldsymbol{\theta}^c = \begin{cases} \boldsymbol{\theta}_g^c & T < T_g(\alpha) \\ \boldsymbol{\theta}_r^c & T \geq T_g(\alpha) \end{cases} \tag{5.8}$$

where $\boldsymbol{\theta}_g^c$ and $\boldsymbol{\theta}_r^c$ were the coefficients of thermal expansion in the glassy and rubbery states, respectively. $T_g(\alpha)$ was obtained from the DiBenedetto equation as

$$\frac{T_g(\alpha) - T_g^{(0)}}{T_g^{(\infty)} - T_g^{(0)}} = \frac{\lambda\alpha}{1-(1-\lambda)\alpha} \tag{5.9}$$

where T_g^0 and $T_g^{(\infty)}$ were the monomer's and fully cured resin's glass transition temperatures, respectively, and λ was a material constant.

Mechanical strains

Elastic model

In a linearly elastic solid, stresses $\boldsymbol{\sigma}$ are related to strains $\boldsymbol{\varepsilon}$ through

$$\boldsymbol{\sigma} = \mathbf{C} : \boldsymbol{\varepsilon} \tag{5.10}$$

in which $\boldsymbol{\varepsilon} = \boldsymbol{\varepsilon}^T - (\boldsymbol{\varepsilon}_C^{NM} + \boldsymbol{\varepsilon}_{TH}^{NM})$, where $\boldsymbol{\varepsilon}^T$ is the total strain and $\boldsymbol{\varepsilon}_C^{NM}$ and $\boldsymbol{\varepsilon}_{TH}^{NM}$ are the stress-free strains associated to the chemical shrinkage and thermal dilatation, respectively. $\mathbf{C}$ is the stiffness tensor (Loos and Springer, 1983; Bogetti and Gillespie Jr, 1992). Johnston (1997) introduced the Cure Hardening Instantaneously Linear Elastic model (CHILE) in which the stiffness tensor evolved with the degree of cure and the temperature. This model accounted for temperature-softening and cure-hardening effects that can occur simultaneously during the manufacturing process. For isotropic materials with constant Poisson's ratio, the degree of cure and temperature dependent elastic Young's modulus was expressed by Khoun et al. (2010) as

$$E(T^*) = \begin{cases} 0 & \alpha < \alpha_{gel} \\ E^{(1)} & T^* < T_1 \\ E^{(2)} + \left(E^{(1)} - E^{(2)}\right)\frac{T^*-T_2}{T_1-T_2} & T_1 \leq T^* < T_2 \\ E_e^{(3)} + \left(E^{(2)} - E^{(3)}\right)\frac{T^*-T_3}{T_2-T_3} & T_2 \leq T^* < T_3 \\ A\exp\left(-KT^*\right) & T_3 \leq T^* < T_4 \\ E^{(4)} & T^* \geq T_4 \end{cases} \tag{5.11}$$

where $E^{(1)}$ was the Young's modulus at the glassy state, $E^{(4)}$ was the Young's modulus at the rubbery state and T_1, $E^{(2)}$, T_2, $E^{(3)}$, T_3, T_4, A and K were material constants. T^* was the difference between the temperature and the instantaneous glass transition temperature, $T^* = T - T_g(\alpha)$. Figure 5.1 schematizes the Young's modulus evolution proposed by Khoun et al. (2010).

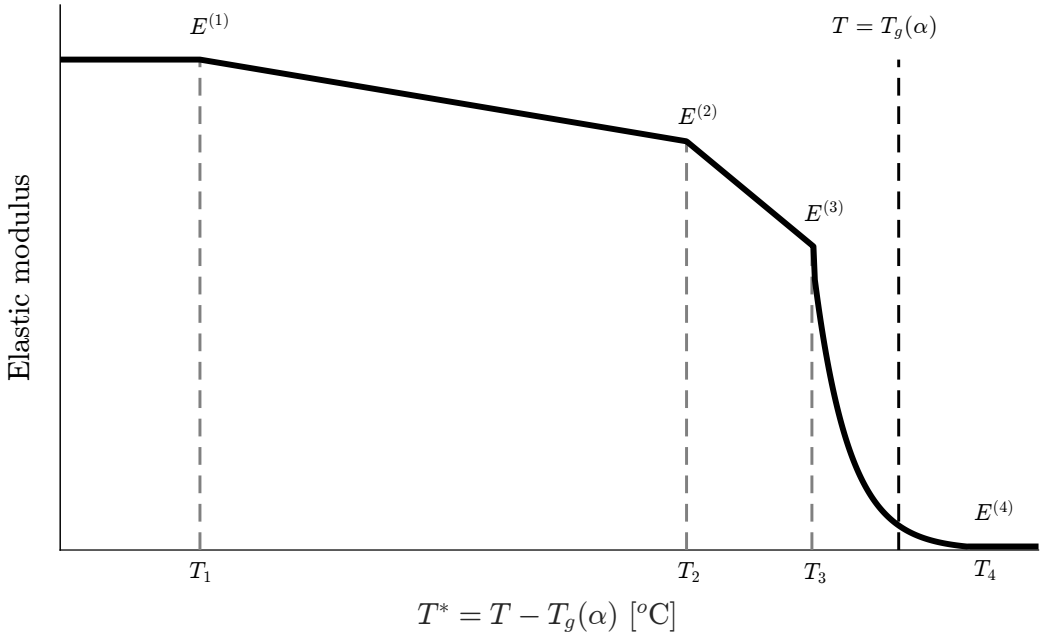

Figure 5.1 Young's modulus evolution for an isotropic material as a function of the temperature and the degree of cure (Khoun et al., 2010)

Linearly viscoelastic model

Linearly viscoelastic constitutive theories were derived from a rigorous thermodynamics framework (Biot, 1954; Lévesque et al., 2008) and, for stress relaxation, can be expressed as

$$\boldsymbol{\sigma}(t) = \mathbf{L}^{(1)} : \boldsymbol{\varepsilon}(t) + \mathbf{L}^{(2)} : \boldsymbol{\chi}(t) \tag{5.12a}$$

$$\mathbf{B} : \dot{\boldsymbol{\chi}} + \mathbf{L}^{(3)} : \boldsymbol{\chi} + \left(\mathbf{L}^{(2)}\right)^T : \boldsymbol{\varepsilon} = 0 \tag{5.12b}$$

where $\boldsymbol{\chi}$ were hidden internal variables and

$$\mathbf{L} = \begin{bmatrix} \mathbf{L}^{(1)} & \mathbf{L}^{(2)} \\ (\mathbf{L}^{(2)})^T & \mathbf{L}^{(3)} \end{bmatrix} \tag{5.13}$$

where $\mathbf{L}$ had be positive definite (which implies that $\mathbf{L^{(1)}}$ and $\mathbf{L^{(3)}}$ have this property) to meet the first and second principles of thermodynamics. $\mathbf{B}$ was a N $\times$ N identity matrix.

The solution of differential equations 5.12 yielded (Luk-Cyr et al., 2013)

$$\sigma_{ij}(t) = \left(L_{ij}^{(1)} - \frac{L_{ir}^{(2)} L_{jr}^{(2)}}{L_{rr}^{(3)}} \right) \varepsilon_j(t) + \frac{L_{ir}^{(2)} L_{jr}^{(2)}}{L_{rr}^{(3)}} \int_0^t \exp\left[-\frac{L_{rr}^{(3)}}{B_{rr}} (t-\tau) \right] \frac{\mathrm{d}\varepsilon_j}{\mathrm{d}\tau} \mathrm{d}\tau \tag{5.14}$$

which could be reduced to

$$\boldsymbol{\sigma}(t) = \mathbf{C}^{(\infty)} : \boldsymbol{\varepsilon} + \int_0^t \sum_{k=1}^{N} \mathbf{C}^{(k)} \exp\left[-\omega^{(k)} (t-\tau) \right] : \frac{\mathrm{d}\boldsymbol{\varepsilon}}{\mathrm{d}\tau} \mathrm{d}\tau \tag{5.15}$$

where $\mathbf{C}^{(\infty)}$ was the fully relaxed tensor and $\mathbf{C}^{(k)}$ were the relaxation tensors associated to the inverted relaxation times $\omega^{(k)}$.

The Time Temperature Superposition Principle (TTSP) has been generally used to incorporate the degree of cure and temperature changes into equation 5.15 by replacing $(t-\tau)$ by (Ferry, 1980; O'Brien et al., 2001; Ruiz and Trochu, 2005a)

$$\xi - \xi' = \int_0^t \frac{\mathrm{d}\gamma}{a_T(T(\gamma), \alpha(\gamma))} - \int_0^\tau \frac{\mathrm{d}\gamma}{a_T(T(\gamma), \alpha(\gamma))} \tag{5.16}$$

where a_T was a shift factor that depended on the degree of cure and temperature.

Path-dependent model

The path-dependent model assumed that the stresses $\boldsymbol{\sigma}$ were expressed as

$$\boldsymbol{\sigma} = \begin{cases} \mathbf{C}^{(\infty)} : \boldsymbol{\varepsilon} & T \geq T_g(\alpha) \\ \mathbf{C}^{(0)} : \boldsymbol{\varepsilon} - \mathbf{C}^{(\infty)} : \boldsymbol{\varepsilon}|_{t=t_{vit}} & T < T_g(\alpha) \end{cases} \tag{5.17}$$

where t_{vit} was the time at which the resin's evolved from rubbery to a glassy state. The path-dependent model assumed that the stiffness matrix remained constant within the rubbery and the glassy states, and varied abruptly from one state to the other at the glass transition temperature (Svanberg and Holmberg, 2004b; Ding et al., 2017).

5.3 Experimental data

The warpage developed in asymmetric epoxy plates reinforced with a 3D interlock carbon woven fabric has been recently characterized by Benavente et al. (2017a). The 3D interlock woven reinforcement has four interlock layers and IM10 carbon fibers from Hexcel. The reinforcement has an unbalanced warp/weft ratio, where 70 % of the fibers are aligned along

the warp direction. A commercial Diglicidyl Ether of Bisphenol F (DGEBF) one component epoxy resin was used as the matrix.

A rectangular steel mold with an internal cavity of 455 mm × 145 mm × 6.7 mm was used to manufacture six plates with a [0/90] lay up configuration and a 58 % fiber volume fraction. Three thermocouples were embedded into the mold prior to injection to monitor the temperature evolution during manufacturing. A one hour dwell at 160 °C followed by two hours at 180 °C was used to ensure the complete curing of the resin. The plates were then cooled inside of the mold until their centers reached 100 °C. The plates were then released from the mold and cooled by natural convection down to room temperature.

The plates were then cut with a diamond saw to 410 mm × 120 mm × 6.7 mm. Finally, the plates' curvature was measured by an electronic Linear Variable Differential Transformer (LVDT) at room temperature.

5.4 Implementation

The modular approach proposed by Loos and Springer (1983) has been adopted in this work to simulate the RTM manufacturing process. Figure 5.2 depicts the modelling approach.
A multi-scale homogenization strategy was used to compute the material behavior of the 3D woven laminate. A micro-scale homogenization based on the properties of the elementary constituents, carbon fibers and epoxy matrix, was carried out to obtain the yarns' mechanical properties. The degree of cure- and temperature-dependent mechanical model for the epoxy resin presented by Courtois et al. (2016) was used. The results from the micro-scale model were then used at the meso-scale level to obtain the macroscopic homogenized mechanical properties. A voxelized FE mesh obtained from Computed Tomography observations was used to account for the reinforcement architecture (Schneider et al., 2009; Hello et al., 2014). The input properties were normalized for confidentiality reasons and are presented in Appendix A.

Mechanical models

Non-mechanical strains

The non-mechanical strains associated with the chemical and thermal expansions were computed from a user subroutine UEXPAN in ABAQUS.

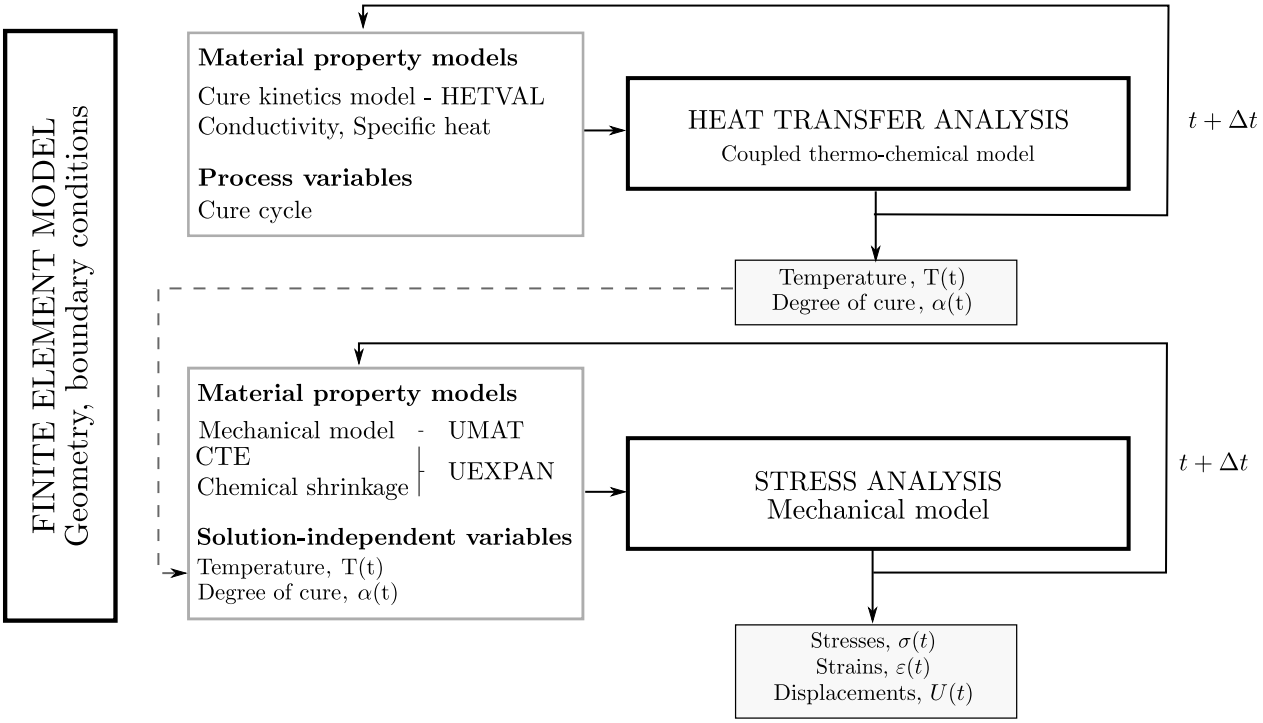

Figure 5.2 Process modelling modular approach flow diagram

The chemical shrinkage strains were computed as

$$\boldsymbol{\varepsilon}_C^{NM}(t + \Delta t) = \boldsymbol{\varepsilon}_C^{NM}(t) + \boldsymbol{\beta^c}(t)\Delta\alpha \tag{5.18}$$

where Δt was the time increment and $\Delta\alpha$ was the degree of cure increment computed from equation A.1. The Chamis expressions presented in equations 5.7 were used to compute the shrinkage coefficients.

The coefficients of thermal expansion were obtained from three-dimensional numerical homogenization and will be the focus of a forthcoming paper.

The strains associated with the CTE ($\boldsymbol{\varepsilon}_{TH}^{NM}$) were computed from

$$\boldsymbol{\varepsilon}_{TH}^{NM}(t + \Delta t) = \boldsymbol{\varepsilon}_{TH}^{NM}(t) + \boldsymbol{\theta^c}(t)\Delta T \tag{5.19}$$

where ΔT was the temperature increment.

Mechanical strains

A total of four UMAT user subroutines were implemented into ABAQUS to predict the mechanical strains. Note that finite element codes like ABAQUS require the user to provide the stress tensor at the end of the increment and the Jacobian matrix ($\partial\Delta\boldsymbol{\sigma}/\partial\Delta\boldsymbol{\varepsilon}$). The following subsections provide the details of these computations.

Elastic models

A simplified CHILE model was developed to describe the stiffness tensor evolution with the temperature and degree of cure as

$$\mathbf{C_e}(T^*) = \begin{cases} \mathbf{C}^{(0)} & T^* < T_0 \\ \mathbf{C_e}^{(1)} + \left(\mathbf{C}^{(0)} - \mathbf{C_e}^{(1)}\right) \frac{T^*-T_1}{T_0-T_1} & T_0 \leq T^* < T_1 \\ \mathbf{C}^{(\infty)} + \left(\mathbf{C_e}^{(1)} - \mathbf{C}^{(\infty)}\right) \frac{T^*-T_\infty}{T_1-T_\infty} & T_1 \leq T^* < T_\infty \\ \mathbf{C}^{(\infty)} & T^* \geq T_\infty \end{cases} \tag{5.20}$$

where $\mathbf{C}_e^{(1)}$, T_0, T_1 and T_∞ were material constants. $\mathbf{C}^{(0)}$ and $\mathbf{C}^{(\infty)}$ were the orthotropic stiffness tensors at glassy and rubbery states, respectively.

Equations 5.10 and 5.20 yielded

$$\boldsymbol{\sigma} = \mathbf{C_e}(T^*) : \boldsymbol{\varepsilon} \tag{5.21}$$

The elastic model from equation 5.21 has been implemented through two methods, namely

- Thermo-elastic model

  Equation 5.21 was written under an incremental formulation as

$$\begin{aligned} \Delta\boldsymbol{\sigma} = \boldsymbol{\sigma}(t+\Delta t) - \boldsymbol{\sigma}(t) &= \mathbf{C_e}(T^*(t+\Delta t)) : \boldsymbol{\varepsilon}(t+\Delta t) - \mathbf{C_e}(T^*(t)) : \boldsymbol{\varepsilon}(t) \\ &= \mathbf{C_e}(T^* + \Delta T^*) : (\boldsymbol{\varepsilon} + \Delta\boldsymbol{\varepsilon}) - \mathbf{C_e}(T^*) : \boldsymbol{\varepsilon} \\ &= (\mathbf{C_e}(T^*) + \Delta\mathbf{C_e}(T^*)) : (\boldsymbol{\varepsilon} + \Delta\boldsymbol{\varepsilon}) - \mathbf{C_e}(T^*) : \boldsymbol{\varepsilon} \\ &= \mathbf{C_e}(T^* + \Delta T^*) : \Delta\boldsymbol{\varepsilon} + \Delta\mathbf{C_e}(T^*) : \boldsymbol{\varepsilon} \end{aligned} \tag{5.22}$$

  where $\Delta\mathbf{C_e}(T^*) = \mathbf{C_e}(T^*(t+\Delta t)) - \mathbf{C_e}(T^*(t))$.

  Finally, the stresses at time $t+\Delta t$ and Jacobian matrix for the cure- and temperature-dependent elastic model were expressed as

$$\begin{aligned} \boldsymbol{\sigma}(t+\Delta t) &= \boldsymbol{\sigma}(t) + \Delta\boldsymbol{\sigma} \\ &= \boldsymbol{\sigma}(t) + \mathbf{C_e}(T^* + \Delta T^*) : \Delta\boldsymbol{\varepsilon} + \Delta\mathbf{C_e}(T^*) : \boldsymbol{\varepsilon} \end{aligned} \tag{5.23a}$$

$$\frac{\partial \Delta \boldsymbol{\sigma}}{\partial \Delta \boldsymbol{\varepsilon}} = \mathbf{C_e}(T^* + \Delta T^*) \tag{5.23b}$$

- Instantaneous-elastic model :
  Many authors (Bogetti and Gillespie Jr, 1992; Johnston, 1997; Fernlund et al., 2002; Zobeiry, 2006; Ersoy et al., 2010b; Ding et al., 2016a) have written equation 5.21 under an (approximate) incremental form as

$$\Delta \boldsymbol{\sigma} = \boldsymbol{\sigma}(t + \Delta t) - \boldsymbol{\sigma}(t) = \mathbf{C_e}(T^* + \Delta T^*) : \Delta \boldsymbol{\varepsilon} \tag{5.24}$$

  which is quite different from equation 5.22 because the term $\Delta \mathbf{C_e}(T^*(t)) : \boldsymbol{\varepsilon}(t)$ is missing. The incremental form of equation 5.24 will only lead to equation 5.22 if $\mathbf{C_e}$ remains constant throughout the whole simulation. We have nevertheless implemented this formulation for comparing its accuracy with respect to the rigorous implementation of equations 5.23. The stress at the end of an increment, as well as the Jacobian matrix, were therefore implemented as

$$\begin{aligned} \boldsymbol{\sigma}(t + \Delta t) &= \boldsymbol{\sigma}(t) + \Delta \boldsymbol{\sigma} \\ &= \boldsymbol{\sigma}(t) + \mathbf{C_e}(T^* + \Delta T^*) : \Delta \boldsymbol{\varepsilon} \end{aligned} \tag{5.25a}$$

$$\frac{\partial \Delta \boldsymbol{\sigma}}{\partial \Delta \boldsymbol{\varepsilon}} = \mathbf{C_e}(T^* + \Delta T^*) \tag{5.25b}$$

Linearly viscoelastic model

The laminate was assumed to have an orthotropic degree of cure- and temperature-dependent linearly viscoelastic behavior composed of thirteen relaxation times ranging from 10^{-9} to 10^{3} minutes and evenly distributed on a logarithmic scale. The implemented constitutive theory reads

$$\boldsymbol{\sigma}(t) = \mathbf{C}^{(\infty)} : \boldsymbol{\varepsilon} + \int_0^t \sum_{k=1}^{N} \mathbf{C}^{(k)} \exp\left[-\omega^{(k)} (\xi - \xi')\right] : \frac{\mathrm{d}\boldsymbol{\varepsilon}}{\mathrm{d}\tau} \mathrm{d}\tau \tag{5.26}$$

where $\mathbf{C}^{(k)}$ were obtained by numerical homogenization and satisfied

$$\mathbf{C}^{(0)} = \mathbf{C}^{(\infty)} + \sum_{k=1}^{N} \mathbf{C}^{(k)} \tag{5.27}$$

where $\mathbf{C}^{(0)}$ and $\mathbf{C}^{(\infty)}$ were the instantaneous and fully relaxed stiffness tensors, respectively, and were equivalent to the glassy and rubbery stiffness tensors used in the elastic model.

The degree of cure and temperature dependency was accounted for through the shift factor

$a_T(T,\alpha)$, as

$$\log(a_T(T,\alpha)) = \begin{cases} \frac{H_1}{(\ln 10)R}\left(\frac{1}{T} - \frac{1}{T_g(\alpha)}\right) & T \geq T_g(\alpha) \\ \frac{H_2}{(\ln 10)R}\left(\frac{1}{T} - \frac{1}{T_g(\alpha)}\right) & T < T_g(\alpha) \end{cases} \tag{5.28}$$

where $H_1 > H_2$ were the resin's activation energies [KJ/mol] calculated by Courtois et al. (2016) and the temperature was expressed in Kelvins.

Equation 5.26 was expressed under the shape of equations 5.12 and solved by a backward Euler first-order Finite Difference (FD) scheme according to the methodology of Crochon et al. (2010). The stresses were expressed as

$$\boldsymbol{\sigma}(t+\Delta t) = \mathbf{L}^{(1)} : \boldsymbol{\varepsilon}(t+\Delta t) + \mathbf{L}^{(2)} : \boldsymbol{\chi}(t+\Delta t) \tag{5.29}$$

where $\mathbf{L}^{(1)} = \mathbf{C}^{(\infty)} + \sum_{k=1}^{k=N} \mathbf{C}^{(k)}$ and

$$\begin{aligned} \boldsymbol{\chi}(t+\Delta t) &= \boldsymbol{\chi}(t) + \Delta t \dot{\boldsymbol{\chi}}(t+\Delta t) \\ &= \boldsymbol{\chi}(t) - \Delta t \mathbf{B}^{-1} : \left(\mathbf{L}^{(3)} : \boldsymbol{\chi}(t+\Delta t) + \left(\mathbf{L}^{(2)}\right)^T : \boldsymbol{\varepsilon}(t+\Delta t)\right) \end{aligned} \tag{5.30}$$

where $\mathbf{L}^{(2)}$ was a $N \times 6$ matrix expressed as

$$\mathbf{L}^{(2)} = \left(\mathbf{L}^{(2)}_{(1)} | \mathbf{L}^{(2)}_{(2)} | .... | \mathbf{L}^{(2)}_{(k)}\right) \tag{5.31}$$

in which

$$\mathbf{L}^{(2)}_{(k)} : \left(\mathbf{L}^{(2)}_{(k)}\right)^T = \omega^{(k)} \mathbf{C}^{(k)} \tag{5.32}$$

and $\mathbf{L}^{(3)}$ was a $N \times N$ diagonal matrix constructed by 6×6 block diagonal matrices as

$$\mathbf{L}^{(3)} = \oplus_{k=1}^{k=N} [\omega^{(k)} \mathbf{I}] \tag{5.33}$$

The degree of cure and temperature dependency was introduced through

$$\mathbf{A} = \frac{1}{a_T(T,\alpha)} \mathbf{B}^{-1} \tag{5.34}$$

The combination of equations 5.29, 5.30 and 5.34 yields

$$\boldsymbol{\sigma}(t+\Delta t) = \left(\mathbf{L}^{(1)} + \mathbf{L}^{(2)} : \mathbf{W}^{(2)}\right) : \boldsymbol{\varepsilon}(t+\Delta t) + \mathbf{L}^{(2)} : \mathbf{W}^{(1)} : \boldsymbol{\chi}(t) \tag{5.35}$$

where

$$\mathbf{W}^{(1)} = \left(\mathbf{I} + \Delta t \mathbf{A} : \mathbf{L}^{(3)}\right)^{-1} \tag{5.36a}$$

$$\mathbf{W}^{(2)} = -\Delta t \mathbf{W}^{(1)} : \mathbf{A} : \left(\mathbf{L}^{(2)}\right)^T \tag{5.36b}$$

Regrouping terms leads to

$$\boldsymbol{\sigma}(t+\Delta t) = \mathbf{M}^{(1)} : \boldsymbol{\varepsilon}(t+\Delta t) + \mathbf{M}^{(2)} : \boldsymbol{\chi}(t) \tag{5.37a}$$

$$\frac{\partial \Delta \boldsymbol{\sigma}}{\partial \Delta \boldsymbol{\varepsilon}} = \mathbf{M}^{(1)} \tag{5.37b}$$

Path-dependent model

The path-dependent model also assumed an orthotropic behavior in which the mechanical properties varied stepwise at the degree of cure-dependent instantaneous glass transition temperature $T_g(\alpha)$ as

$$\mathbf{C}_{\text{pd}}(t+\Delta t) = \begin{cases} \mathbf{C}^{(\infty)} & T(t+\Delta t) \geq T_g(\alpha) \\ \mathbf{C}^{(0)} & T(t+\Delta t) < T_g(\alpha) \end{cases} \tag{5.38}$$

The path-dependent model has been written under an incremental formulation as (Svanberg and Holmberg, 2004b; Nielsen, 2012; Ding et al., 2017)

$$\Delta \boldsymbol{\sigma} = \begin{cases} \mathbf{C}^{(\infty)} : \Delta \boldsymbol{\varepsilon} - \boldsymbol{s}(t) & T(t+\Delta t) \geq T_g \\ \mathbf{C}^{(0)} : \Delta \boldsymbol{\varepsilon} & T(t+\Delta t) < T_g \end{cases} \tag{5.39}$$

where $\boldsymbol{s}$ was a history state variable that accounted for the loading history and was expressed as

$$\boldsymbol{s}(t+\Delta t) = \begin{cases} 0 & T(t+\Delta t) \geq T_g \\ \boldsymbol{s}(t) + \mathbf{C}^{(\infty)} : \Delta \boldsymbol{\varepsilon} & T(t+\Delta t) < T_g \end{cases} \tag{5.40}$$

It was through the history state variable, $\boldsymbol{s}$, that the "frozen-in" strains were accounted for. The "frozen-in" strains were set to zero above the glass transition temperature to simulate the material's complete "relaxed" state.

Finally, the stresses at the end of the increment and the Jacobian matrix were expressed as

$$\begin{aligned} \boldsymbol{\sigma}(t+\Delta t) &= \boldsymbol{\sigma}(t) + \Delta \boldsymbol{\sigma} \\ &= \boldsymbol{\sigma}(t) + \begin{cases} \mathbf{C}^{(\infty)} : \Delta \boldsymbol{\varepsilon} - \boldsymbol{s}(t) & T(t+\Delta t) \geq T_g \\ \mathbf{C}^{(0)} : \Delta \boldsymbol{\varepsilon} & T(t+\Delta t) < T_g \end{cases} \end{aligned} \tag{5.41a}$$

$$\frac{\partial \Delta \boldsymbol{\sigma}}{\partial \Delta \boldsymbol{\varepsilon}} = \mathbf{C}_{pd}(t+\Delta t) \tag{5.41b}$$

Table 5.1 summarizes the implemented stress at the end of the increment, as well as the Jacobian matrix, for the four selected models.

5.4.1 Case studies

Models comparisons under uniaxial stress states

A fully cured composite cube (α=1) was subjected to simultaneous temperature changes and mechanical loads. The cube was modeled in ABAQUS using an eight-node brick element (C3D8). Figure 5.3 shows the schematic representation of the boundary conditions. A time discretization of one minute per increment was fixed (see Section 5.4.1). It was assumed that the composite was fully cured, and hence the chemical shrinkage and the mechanical properties evolution with the degree of cure were neglected.

Monotonous tension tests

The composite's mechanical behavior was computed by simulating monotonous tension test at temperatures ranging from 20 to 200 °C. A strain rate of 0.2 % per minute was imposed in the warp direction. A total of 76 simulations were carried out, nineteen simulations per implementation model.

Blocks of relaxation periods

The stress evolution over a linear temperature ramp at 0.5 °C/min from 20 to 180 °C was computed with the four implemented models. The element was preloaded with a uniaxial strain of 0.2 % in the warp direction prior the ramp. This strain was maintained over the whole simulation.

Linear heating at constant strain

Figure 5.4 shows the applied thermal and stress cycle as presented by Svanberg and Holmberg (2004b). The simulation was constituted of five segments in which :

- **Segment 1 :** The element was heated from 20 °C to 160 °C, above the resin's glass transition temperature, within the first 100 minutes.
- **Segment 2 :** The element was subjected to an isotherm at 160 °C for 100 minutes. A stress of 3 MPa was applied during this period.
- **Segment 3 :** The applied stress in 2 was held constant during this segment while the element was cooled-down to 20 °C.

Table 5.1 Stress at the end of an increment $(t + \Delta t)$ and the Jacobian matrix for the implemented models

	$\boldsymbol{\sigma}(t + \Delta t)$
Thermo-elastic	$\boldsymbol{\sigma}(t) + \mathbf{C_e}(T^* + \Delta T^*) : \Delta\boldsymbol{\varepsilon} + \Delta\mathbf{C_e}(T^*) : \boldsymbol{\varepsilon}$
Instantaneous-elastic	$\boldsymbol{\sigma}(t) + \mathbf{C_e}(T^* + \Delta T^*) : \Delta\boldsymbol{\varepsilon}$
Viscoelastic	$\mathbf{M}^{(1)} : \boldsymbol{\varepsilon}(t + \Delta t) + \mathbf{M}^{(2)} : \boldsymbol{\chi}(t)$
Path depedent	$\boldsymbol{\sigma}(t) + \begin{cases} \mathbf{C}^{(\infty)} : \Delta\boldsymbol{\varepsilon} - \boldsymbol{s}(t) & T(t + \Delta t) \geq T_g \\ \mathbf{C}^{(0)} : \Delta\boldsymbol{\varepsilon} & T(t + \Delta t) < T_g \end{cases}$

	Jacobian matrix $\left(\frac{\partial \Delta\boldsymbol{\sigma}}{\partial \Delta\boldsymbol{\varepsilon}}\right)$
Thermo-elastic	$\mathbf{C_e}(T^* + \Delta T^*)$
Instantaneous-elastic	$\mathbf{C_e}(T^* + \Delta T^*)$
Viscoelastic	$\mathbf{M}^{(1)}$
Path depedent	$\mathbf{C}_{\mathrm{pd}}(t + \Delta t)$

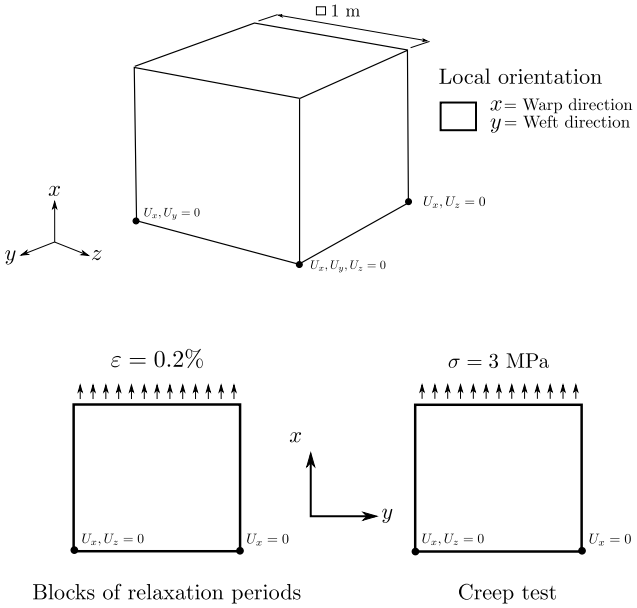

Figure 5.3 Orientation and boundary conditions applied to a fully cured composite element

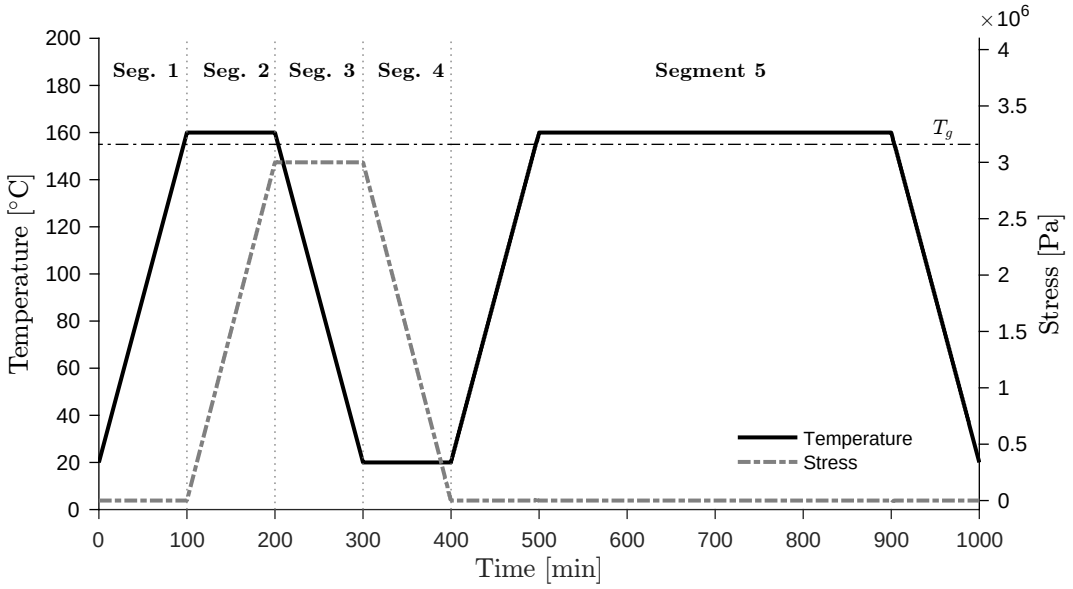

Figure 5.4 Thermal and stress cycle applied in a completely cured cube in the warp direction during the blocks of creep periods

- **Segment 4 :** The stress was released.
- **Segment 5 :** The element was heated to 160 °C for 400 minutes to recover the residual strains, if needed.

RTM manufacturing of an asymmetric plate simulation

The stresses and warpage developed during the manufacturing of asymmetric plates reinforced with the 3D woven interlock fabric were computed following the manufacturing methodology explained in Section 5.3. The [0/90] asymmetric lay up configuration was implemented by dividing the plate into two equidistant sections through the thickness, each of them having a different material orientation, as shown in Figure 5.5. Linear eight-noded brick elements DC3D8 and C3D8 were used in the thermo-chemical and mechanical models, respectively.

Process simulation

The manufacturing process was modeled in a two-step procedure as :

- **Segment 1 :** The uncured plate was submitted to a thermal cycle inside the mold.
  - Thermo-chemical model : The temperature measured experimentally during the RTM process by Benavente et al. (2017a) was imposed on the plate's surface as thermal boundary conditions.

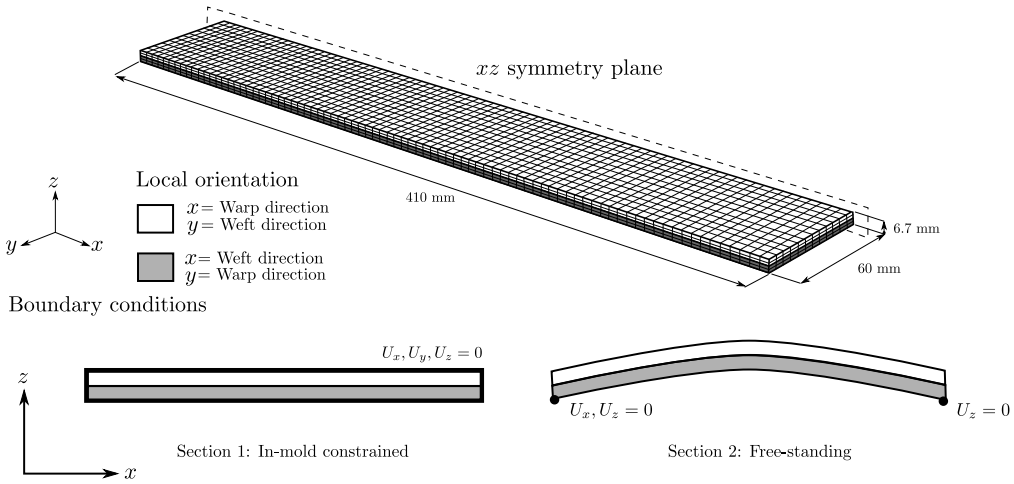

Figure 5.5 Mesh and schematic boundaries conditions applied in the first and second segments for the RTM manufacturing simulation of an asymmetric plate reinforced with 3D interlock fabric

— Mechanical model : The plate was assumed to be fully constrained by the mold during this period, as shown in Figure 5.5.

- **Segment 2 :** The plate was released from the mold and cooled-down by natural convection to room temperature.
  - — Thermo-chemical model : A surface film was used as thermal boundary condition. Several cool-down simulations were carried out to select the surface film condition properties, by varying the film coefficient between 5 to 15 $Wm^{-2}K^{-1}$, that best matched the experimentally measured temperature. Figure 5.6 shows that a film coefficient and sink temperature of 7.5 $Wm^{-2}K^{-1}$ and 25 °C, respectively, predicted the closest temperature evolution when compared to the experimental measurements.
  - — Mechanical model : The plate was submitted to displacement boundary conditions to prevent rigid body motions while ensuring free standing conditions, as shown in Figure 5.5.

Mesh and convergence analyses

A convergence analysis, based on the computed maximal deflection, was carried out with the viscoelastic model to select the mesh size, number of elements per layer and the largest time increment. A total of fifteen simulations were carried out to conduct the convergence analysis in which the mesh size and number of elements per layer varied, as shown in Table 5.2. The element size was imposed by the number of elements per layer, with a maximum ratio of 5 :1

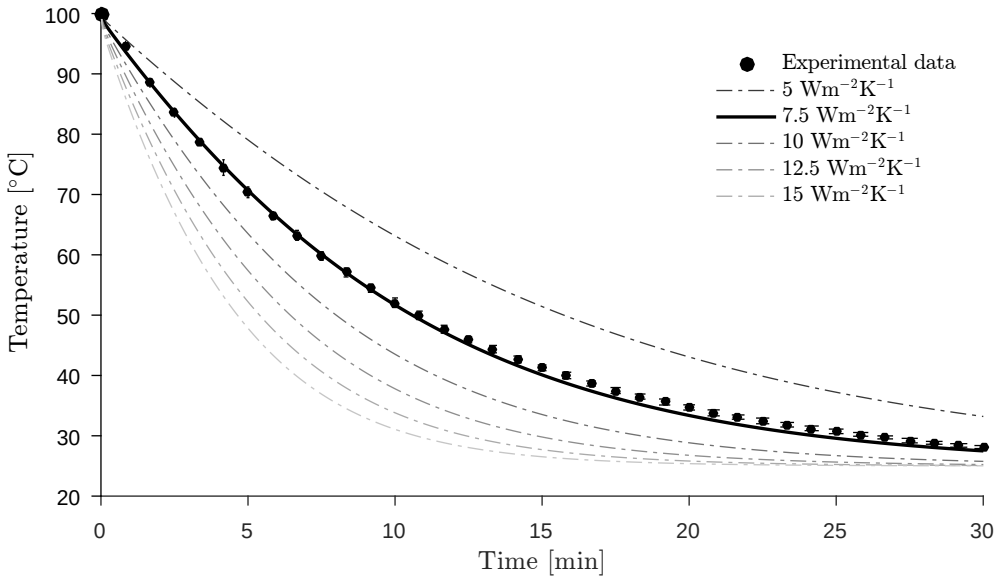

Figure 5.6 Temperature evolution at the center of an asymmetric plate during natural convection cool-down (Segment 2). Continuous lines represent simulated responses while the experimental data is represented by dots

between the element length and thickness. Figure 5.7 shows the curvature relative error when compared to the converged curvature computed with quadratic brick (C3D20) elements with four elements per layer and a mesh size of 3.4 mm. Figure 5.7 reveals that a mesh size of 3.4 mm with two C3D8 elements per layer led to a relative error of 1.5 %, which was deemed acceptable.

The largest time increment in the coupled thermo-chemical model was selected by imposing a convergence condition of 1 °C per time increment during the analysis. Seven analyses were carried out with the viscoelastic model with different time steps ranging from 0.1 to 20 minutes. Figure 5.8 shows the curvature relative error for different time increments (Δt), when compared to that obtained with a time increment of 0.1 minute. The relative error decreased linearly with the time increment with a slope of one which is consistent with the first order Euler scheme implemented. Based on the convergence analysis, the largest time increment was selected to be one minute to reduce the computational running time.

Table 5.2 Parameters studied in the mesh size convergence analysis with C3D8 elements

One element/layer

Mesh type	C3D8				
Mesh size [mm]	16.8	13.4	10	6.7	3.4
Number of nodes	375	465	882	1,860	7,011
Number of elements	192	240	492	1,098	4,392

Two elements/layer

Mesh type	C3D8			
Mesh size [mm]	8.4	6.7	5	3.4
Number of nodes	2,000	3,100	5,330	11,685
Number of elements	1,372	2,196	3,888	8,784

Three elements/layer

Mesh type	C3D8		
Mesh size [mm]	5.6	4.5	3.4
Number of nodes	6,216	9,016	16,359
Number of elements	4,818	7,098	13,176

Four elements/layer

Mesh type	C3D8		C3D20
Mesh size [mm]	4.2	3.4	3.4
Number of nodes	13,230	21,033	21,033
Number of elements	10,864	17,568	17,568

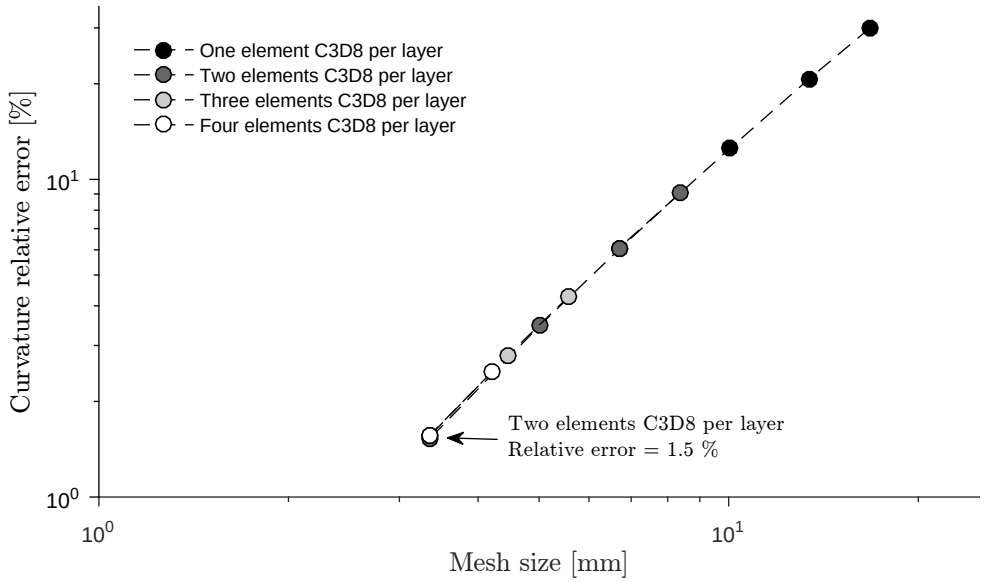

Figure 5.7 Normalized curvature of an asymmetric plate at room temperature with respect to various mesh sizes and elements per layer after the manufacturing process simulation

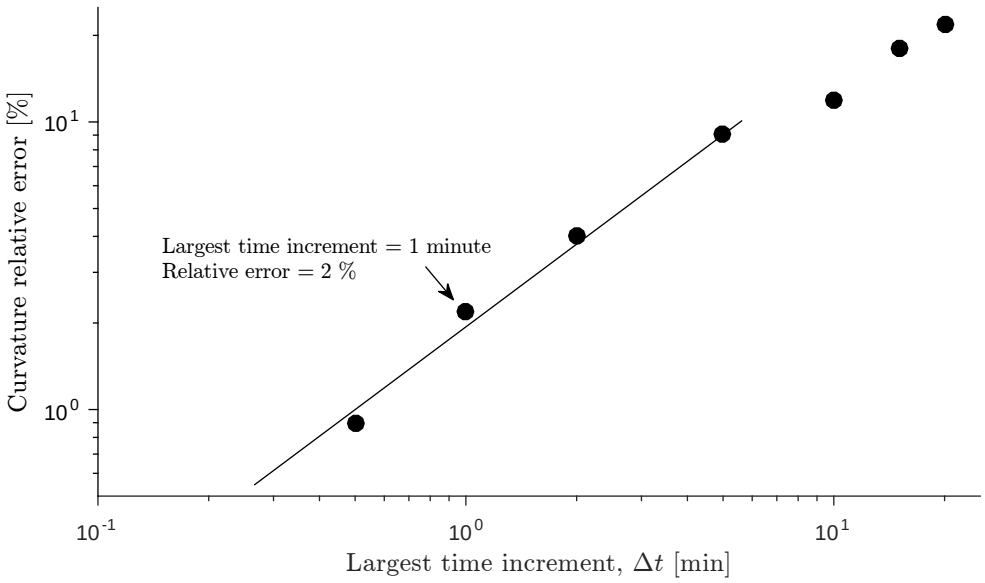

Figure 5.8 Normalized curvature for different time-step (Δt) sizes used during the manufacturing simulation of an asymmetric plate

5.5 Results and discussions

5.5.1 Models comparisons under uniaxial stress states

Monotonous tension tests

Figure 5.9 shows the mechanical response of a single element subjected to an isothermal monotonous tensile tests. Each point corresponds to one simulation at a given temperature with a 0.2 % strain. The figure shows that the stress evolution with the temperature were equal for the thermo- and instantaneous-elastic models. The stresses computed by the path-dependent model were constant through the glassy ($T > T_g$) and rubbery ($T > T_g$) states and varied stepwise at the glass transition temperature. The figure also shows that the stresses computed at 20 °C and at high temperatures, above 170 °C, for the four models were the same. This can be explained by the fact that it was assumed that the composite behaved in the glassy state as an unrelaxed material and as a completely relaxed material in the rubbery state. Thus, the four models had the same $\mathbf{C}^{(0)}$ and $\mathbf{C}^{(\infty)}$ and therefore the same behavior at those states.

Finally, the viscoelastic model computed a higher level of stresses than the thermo-elastic and instantaneous-elastic models, for temperatures ranging from 120 to 170 °C. This can be explained by the fact that the rate at which the time-dependent stiffness decreased with the

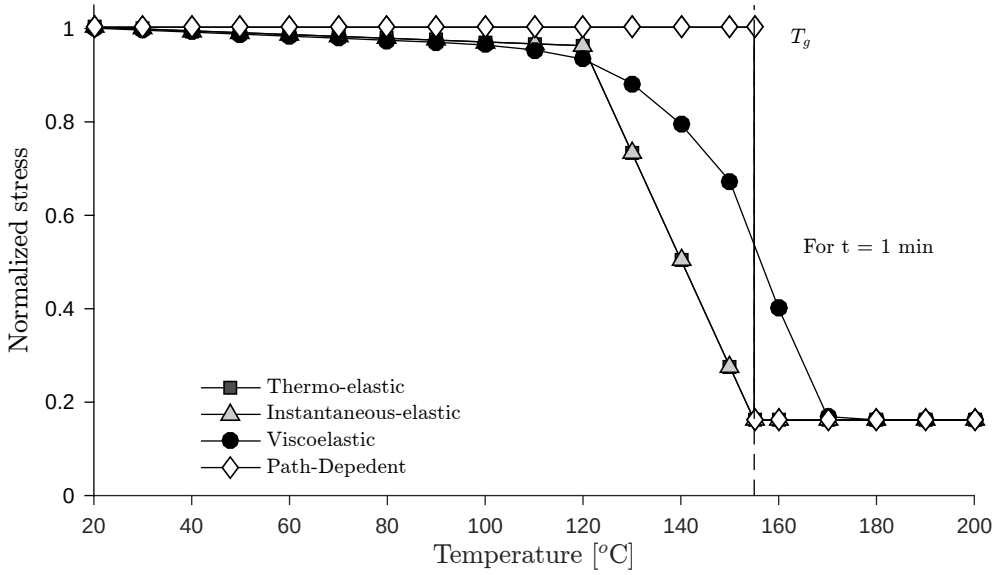

Figure 5.9 Normalized stress in the warp direction as a function of temperature for a completely cured composite after being submitted to isotherm monotonous traction tests at different temperatures. The results were normalized by the stresses computed at 20 °C

viscoelastic model, for the studied load history, was slower than that predicted by the other models as a function of the (time-dependent) temperature. It is important to note that the stresses computed with the viscoelastic model are time-dependent and therefore other load histories could have led to a different trend.

The same tendencies were observed for the weft and out-of-plane directions (not reported here).

Linear heating at constant deformation

Figure 5.10 shows the stress evolution with the temperature for the four implemented models. The figure shows that the thermo-elastic model predicted a decrease of the computed stresses with an increase of temperature, which was caused by the stiffness reduction shown in Figure 5.9. On the other hand, the instantaneous-elastic model computed a constant stress during the heating-up. This is due to the fact that equation 5.25 does not account for the stiffness tensor evolution with the temperature within a time increment under a constant load. This simplification should be avoided in simulations where temperature variations are involved. The viscoelastic model predicted a stress relaxation during the heating phase. This behavior was more accentuated above 120 °C. The completely relaxed state was reached at the end of the simulation at 180 °C. Finally, the path-dependent model reproduced the stress

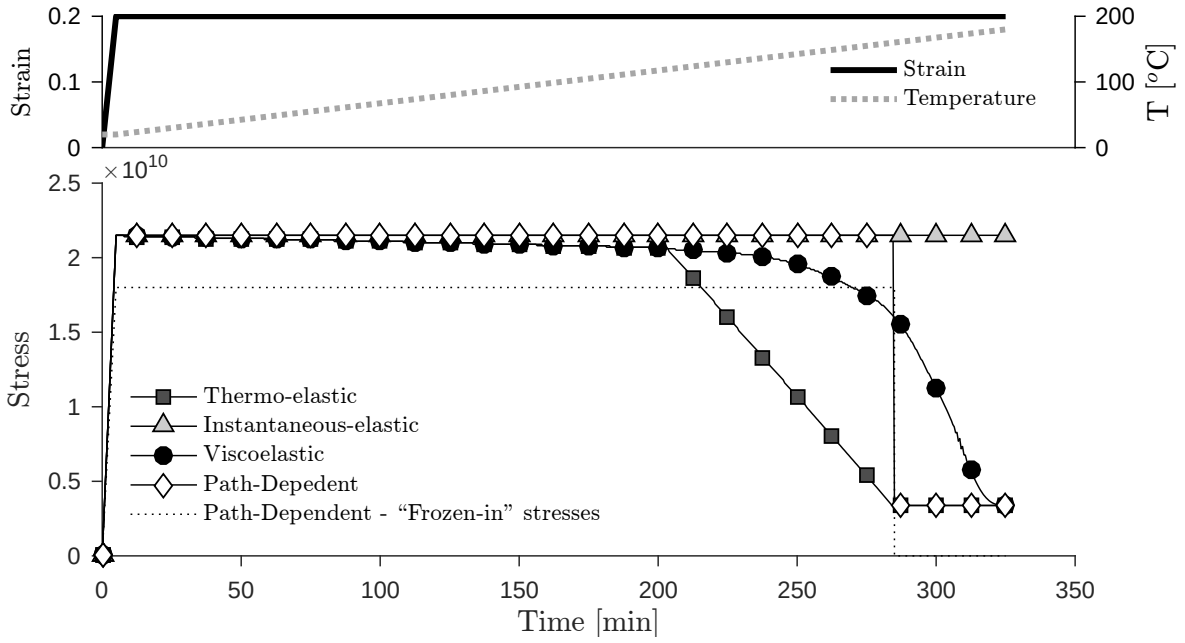

Figure 5.10 Stress evolution in the warp direction as a function of temperature for a completely cured composite during a linear heating at a constant deformation of 0.2 %

decrease that occurred at the glass transition temperature at 155 °C. However, the stress decrease was caused by the release of "frozen-in" stresses and not the stiffness variation itself, as shown in equation 5.41a. Note that the path-dependent model was a phenomenological model developed to account for the "frozen-in" stresses generated during a constrained cool-down from above the glass transition temperature. However, Figure 5.10 shows that the path-dependent model predicted that "frozen-in" stresses were generated during the strain application at 20 °C. This result suggests that this model did not reproduce correctly the "frozen-in" stresses phenomenon. Moreover, as shown in equation 5.41a, the path-dependent model does not account for the stiffness tensor evolution with temperature within a time increment under a constant load, as the instantaneous elastic implementation (eq. 5.25). Thus, the path-dependent model should be avoided in simulations with temperature variations.

Blocks of creep periods

Figure 5.11 shows the total and mechanical strains, $\boldsymbol{\varepsilon}^T$ and $\boldsymbol{\varepsilon}$, respectively, for the applied stress and temperature cycles. The figure reveals that

- **Segment 1 :** The total strains increased linearly during the heating phase from 20 to 160 °C. The cube reached its glass transition temperature after 96 minutes. The total

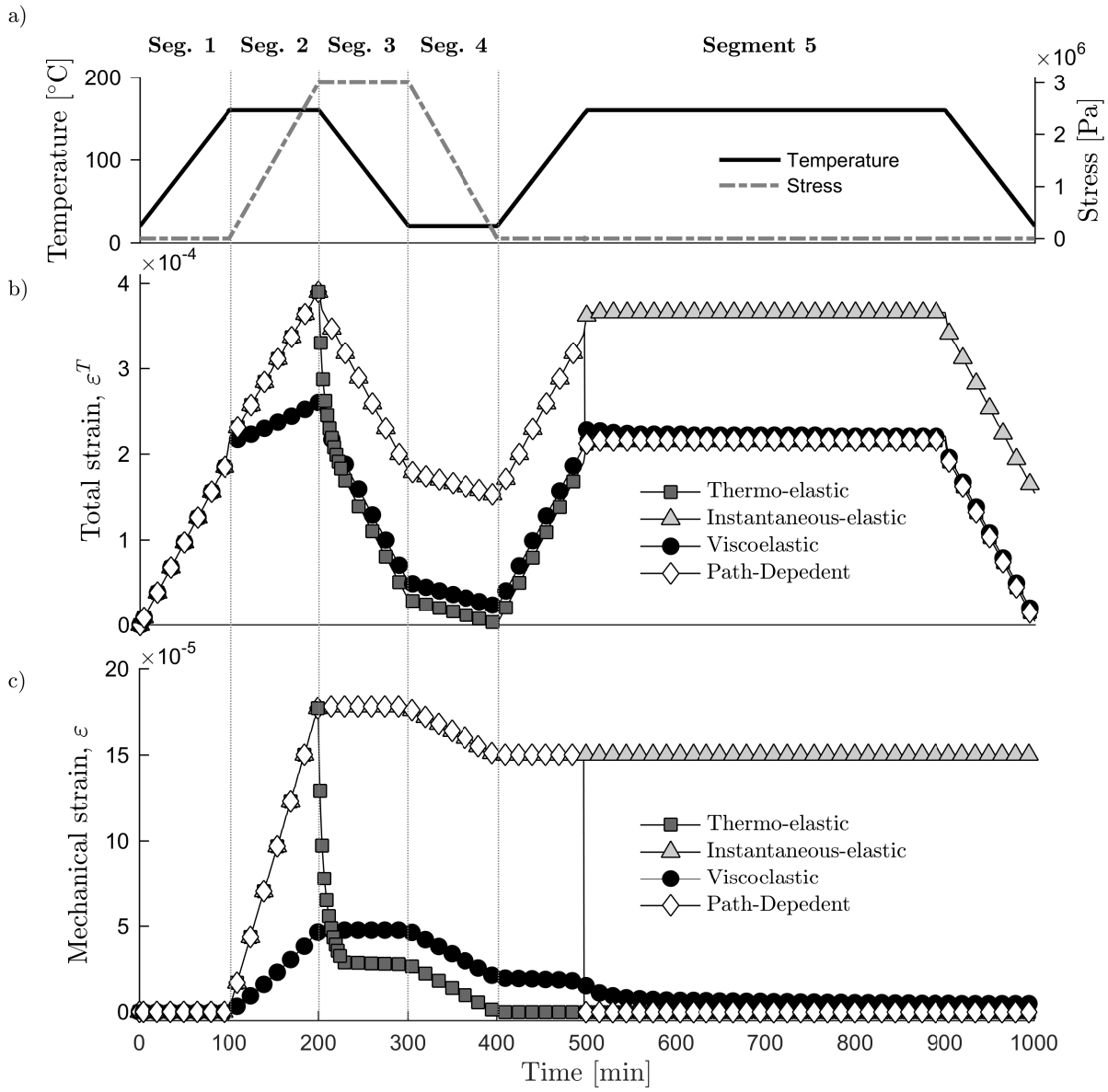

Figure 5.11 Applied temperature and stresses in the warp direction(a) and the computed total (b) and mechanical (b) strains in the warp direction during the blocks of creep periods in a completely cured cube with the four implemented models

strains variation corresponds to that of the CTE when it evolved from glassy ($\boldsymbol{\theta}_g^c$) to rubbery ($\boldsymbol{\theta}_r^c$). The mechanical strains remained constant and equal to zero with the temperature variation.

- **Segment 2 :** The figure shows that the strains varied linearly with the applied stress at 160 °C for the thermo-elastic, instantaneous-elastic and path-dependent models during the isotherm. The creep behavior triggered by the elevated temperature was predicted by the viscoelastic model during this stage.
- **Segment 3 :** The figure shows that the total strains decreased linearly with the temperature for the instantaneous-elastic, viscoelastic and path-dependent models. The thermo-elastic model predicted a decrease in the mechanical strains, caused by an increase in the stiffness during cool-down. The figure also shows that the mechanical strains computed by the viscoelastic, instantaneous-elastic and path-dependent models remained constant.
- **Segment 4 :** The strains decreased linearly with the stresses for the four implemented models. The thermo-elastic model predicted zero strains once the element was stress-free at 20 °C (400 minutes). The figure shows that the viscoelastic model predicted residual strains associated with the creep occurred in Segment 2. The instantaneous-elastic and path-dependent models predicted a permanent deformation once the element was returned to its initial condition. These results suggest that instantaneous-elastic and path-dependent models do not yield results that would be physically expected.
- **Segment 5 :** The total strains increased linearly with the temperature during the heating phase. The viscoelastic model predicted the creep strains recovery during the heating phase, reducing the residual strains to zero. The mechanical strains predicted by the thermo-elastic and instantaneous-elastic models remained constant during the thermal cycle. Finally, the path-dependent model predicted a drop in the mechanical strains once the temperature was above the glass transition temperature. This drop was caused by the “release" of the “frozen-strains".

These results confirm that the instantaneous-elastic and path-dependent models did not account for stiffness variation during the heating-up, when submitted to an imposed load (Segment 3). The models predicted a residual strain at the end of Segment 4 once the load was removed at lower temperature and returned to the initial conditions (load free at 20 °C). Based on the conservation of energy law, the total energy of an insulated system should remain constant. Since the part did not exhibit any permanent transformation during the analysis (from liquid to solid or plastic deformation) it would have been expected that the part went back to a zero strain state when returned to its initial conditions. Thus, it can be

concluded those implementation strategies are not suitable for analyses involving mechanical properties variation.
The viscoelastic model predicted residual creep strains after removing the load (Segment 4). The creep strains were recovered with time and by heating the part in a stress-free condition. It is important to recall that equations 6.13 were derived from a rigorous thermodynamics framework and that the creep strains computed by the viscoelastic model will be recovered over time.

5.5.2 RTM manufacturing of an asymmetric plate

Figure 5.12 shows the plates's center temperature and degree of cure (a), the in-plane longitudinal stresses (b) and the displacement through the thickness (c) evolution during the manufacturing process. The manufacturing process can be divided in two segments, where

- **Segment 1 :** The plate was in-mold constrained and the stresses evolved with the degree of cure and temperature variation. The four models predicted a zero displacement during this segment. This segment can be divided in four subsegments as
  - **Subsegment 1.1 :** The temperature remained constant while the resin cured. The gel point (α_{gel}) was reached after 50 minutes, thus increasing the internal stresses triggered by chemical shrinkage.
  - **Subsegment 1.2 :** The temperature increase induced material expansion, thus reducing the internal stresses generated in subsegment 1.1.
  - **Subsegment 1.3 :** The plate was completely cured and set to an isotherm at 180 °C. The stresses remained constant.
  - **Subsegment 1.4 :** The stresses increased during the cool-down period due to the CTE mismatch between the plies and boundary conditions. The higher stresses computed by the viscoelastic model during the first period of the cool-down inside the mold (from 180 to 130 °C) can be explained by the higher stiffness properties, as shown in Figure 5.9. After 260 minutes, the thermo-elastic model predicted a higher level of stresses than the viscoelastic model. This can be explained by the fact that the thermo-elastic model did not accounted for the residual stresses relaxation that occurred during the cool-down inside the mold, and therefore a higher level of stresses would be expected from a elastic model when compared to a viscoelastic model. Thermo-elastic, instantaneous-elastic and path-dependent models computed the same stresses during the cool-down above the glass transition temperature (from 200 to 240 minutes). This is explained by the fact that the stiffness tensor above glass transition temperature was constant and equal for the three models. The instantaneous-elastic model led to the lower internal stresses

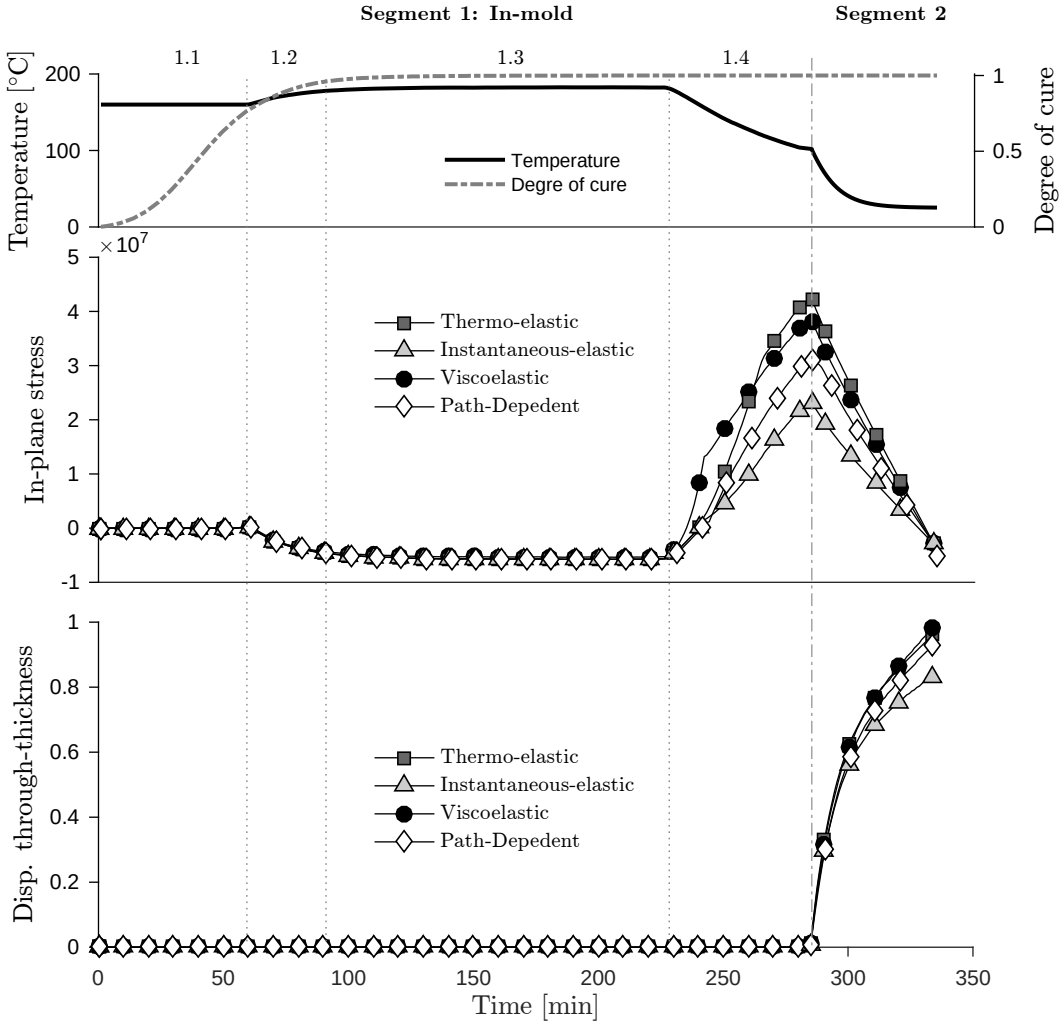

Figure 5.12 Temperature and degree of cure (a), the in-plane longitudinal stresses (b) and the normalized displacement through the thickness (c) evolution at the plate's center during the RTM manufacturing, for the four implemented models

after 240 minutes.

- **Segment 2 :** The plate was released from the mold once it was cooled-down to 100 °C. This condition led to a reduction of the internal stresses. The four implemented models led to similar stresses after the manufacturing process.

The plate's curvature experimentally measured by Benavente et al. (2017a) was compared to those predicted by the models. Figure 5.13 shows the relative difference between the curvature predicted by the implemented models and that experimentally measured. The figure shows that the thermo-elastic, path-dependent and viscoelastic models led to discrepancies lower than 5 %, when compared to the experimental data. The instantaneous-elastic model underestimated the warpage by 16 %. Note that the plate was completely constrained during segment 1, meaning that the displacement in the three directions were set to zero, to simulate the tool-part interaction. This simplification could have induced a higher level of residual stress relaxation predicted by the viscoelastic model during the in-mold manufacturing, thus yielding a lower geometrical deformation.

5.6 Conclusions

The elastic, viscoelastic and path-dependent constitutive laws have been implemented in ABAQUS. The validity of the models was studied in two test cases where an element was submitted to different thermal and load cycles. The results reveal that the instantaneous-elastic implementation strategy generally used in the literature did not account for the stiffness decrease that occurred during temperature variations under an imposed mechanical load. The model led to non-zero strains once the element returned to its initial conditions in the block of creep periods. Based on the conservation energy law the final strains should be fully recovered. This result suggests that this model is not in agreement with the conservation of energy law and was therefore considered as not thermodynamically admissible.

Svanberg and HolmbergSvanberg and Holmberg (2004b) stated that "frozen-in" stresses are induced into the part when the material transform from rubbery (above glass transition temperature) to glassy state (below T_g) during constrained conditions. However, the results obtained with the path dependent model during the temperature ramp at a constant deformation reveals that the "frozen-in" stresses are generated during the strain application at 20 °C. This result is not in agreement with the "frozen-in" stress definition and hence the validity of the path-dependent model could be questioned. In addition, the path-dependent implementation strategy is similar to the instantaneous-elastic implementation. Thus, the stiffness evolution that occurrs during temperature variations under an imposed mechanical load is not accounted for. Based on those results, it can be concluded that the thermo-elastic

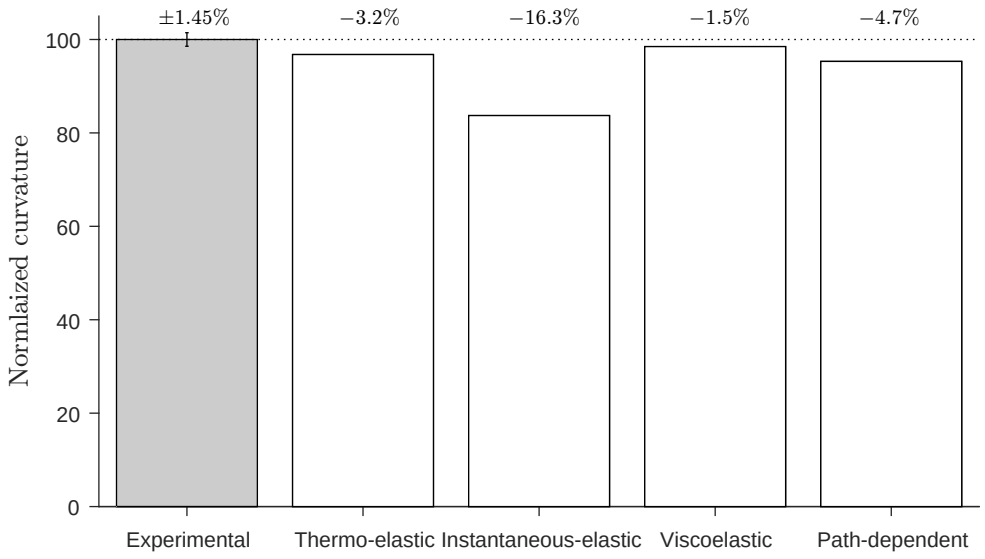

Figure 5.13 Comparison of warpage developed during the manufacturing of asymmetric plates reinforced with 3D interlock fabric between the experimental and numerical models

and path-dependent models are not suitable to predict the residual stresses developed in composite parts during the RTM manufacturing.

The residual stresses developed during the manufacturing of an asymmetric plate have been analyzed using the different constitutive laws. The result revealed that the four implemented models led to discrepancies lower than 16 %, when compared to experimental measurements. Thermo-elastic and viscoelastic models led to the most accurate predictions for the studied cure cycle.

The results presented in this paper show that the viscoelastic model predicted a significant viscoelastic behavior during the blocks of creep periods at high temperatures. The simulations carried out to predict the geometrical distortion and residual stresses showed that the viscoelastic model yielded to the most accurate predictions. However, it was observed that the thermo-elastic model, which neglected the viscoelastic behavior, yielded similar residual stresses and geometrical distortion, when compared with the viscoelastic model for the studied cure cycle. Future works will deal with the advantages and limitations of the thermo-elastic and viscoelastic models during post-curing analyses.

Acknowledgments

The authors would like to acknowledge Safran Group and the Canada Research Chair program for the financial support and for providing the resin and reinforcements used in this work. The National Science and Engineering Research Council (NSERC) of Canada, the Fonds Québécois pour la Recherche sur la Nature et les Technologies (FQRNT), the Canada Foundation for Innovation (CFI) and of the Ministère de l'Éducation du Québec are gratefully acknowledge for their contribution with the infrastructure and expenses of the composite laboratory.

CHAPTER 6 ARTICLE 3 : NUMERICAL ANALYSIS OF VISCOELASTIC PROCESS-INDUCED RESIDUAL DISTORTIONS DURING MANUFACTURING AND POST-CURING

M. Benavente, L. Marcin, A. Courtois, M. Lévesque, E. Ruiz (2017).

Accepted at Composite Part A : Applied Science and Manufacturing on January 4th 2018

Abstract

Degree of cure- and temperature-dependent elastic and viscoelastic models were implemented into ABAQUS to compute the geometrical distortion developed during the RTM manufacturing and post-curing of asymmetric plates and corner shaped parts. Comparisons between the predicted and experimental geometrical distortion for an asymmetric plate reinforced with 3D interlock woven fabric are presented. The results showed that the parts can experience creep behavior when submitted to free-standing post-curing, increasing the total geometrical distortion up to 30 %, depending on post-curing cycle and part geometry. The numerical results of this work demonstrate that a temperature-dependent viscoelastic model is needed to accurately predict the geometrical distortion evolution developed during cure cycles where post-curing processes are involved.

6.1 Introduction

Residual stresses arising in the manufacturing of thermoset composites have been widely studied in the last four decades (Hahn, 1976; Bogetti and Gillespie Jr, 1991; White and Hahn, 1993; Ruiz and Trochu, 2005a). Their presence can induce a reduction of the part's mechanical performance by matrix cracking, delamination and/or geometrical distortion, thus limiting the use of composites for structural parts (Novak and DeCrescente, 1970; White and Hahn, 1993; Ruiz and Trochu, 2005a). Residual stresses can be triggered by the thermal mismatch between the fibers and the matrix, the chemical shrinkage occurring during the curing stage and the tool-part interaction (Radford and Rennick, 2000; Svanberg and Holmberg, 2001; Potter et al., 2005; Radford, 2010).

The geometrical distortion in balanced curved parts and in flat plates with asymmetric lay-up configuration has been characterized during and/or after the manufacturing process to estimate the internal residual stresses at the macro-scale level (Wisnom et al., 2006; Khoun et al., 2011; Ruiz and Trochu, 2005a; Palerosi and de Almeida, 2007). The reduction of closed

angles in curved parts, also known as spring-in, has been measured after the manufacturing process to establish the effect of part thickness, tool part interaction and lay-up configuration, among others (Svanberg and Holmberg, 2001; Fernlund et al., 2003; Wisnom et al., 2006). The spring-in varies, generally, from 0.5 to 2 °.

The contribution of chemical shrinkage to the total distortion has been characterized through interrupted cure cycles (White and Hahn, 1992; Gigliotti et al., 2003; Ersoy et al., 2005). The results showed that chemical shrinkage accounted for 5 % of the curvature developed in flat plates with an asymmetric lay-up (White and Hahn, 1992; Gigliotti et al., 2003) and 50 % of the spring-in developed in "L" or "C" shaped parts (Ersoy et al., 2005). The geometrical distortion in curved parts and asymmetric plates have been simulataneouly measured with the temperature variation, thus measuring the contribution of the Coefficient of Thermal Expansion (CTE) (Radford and Diefendorf, 1993; Ruiz and Trochu, 2005a; Palerosi and de Almeida, 2007). Several studies suggested that the geometrical distortion was governed by the in-plane and through-the-thickness properties for corner shaped parts and by the in-plane properties for asymmetric plates (White and Hahn, 1992; Fernlund et al., 2003; Wisnom et al., 2006; Ersoy et al., 2005; Radford, 2010).

Svanberg and Holmberg (2001) measured the evolution of the spring-in prior and after a free-standing post-curing. Their results showed a 30 % increase in the spring-in after submitting the part to a four-hour free-standing post-curing at 120°C, above its glass transition temperature. This phenomenon was explained by the release of "frozen-in" stresses. Kominar (1996) stated that the stresses developed during the manufacturing cannot be released during the in-mold cool-down, thus leaving the part with "unreleased" or "frozen-in" stresses (Kim and Daniel, 2002; Svanberg and Holmberg, 2004a; Kim, 2004; Minakuchi, 2015). Recently, Benavente et al. (2017a) measured the curvature evolution of asymmetric plates reinforced with three-dimensional (3D) interlock fabric during and after submiting the parts to different free-standing post-curing conditions. Their results showed that the "frozen-in" stresses were in fact related to viscoelastic creep strains occurring at high temperature. Viscoelastic effects accounted for 20 % of the total deflection in their studied parts.

Numerical models have been developed over the last three decades to simulate the different stages and phenomena involved during the in-mold manufacturing of composites (Johnston, 1997; Fernlund et al., 2002; Ruiz and Trochu, 2005a; Zobeiry, 2006; Canal et al., 2015). Elastic, viscoelastic and path-dependent models have been used to describe composites mechanical evolution with the degree of cure and temperature (Johnston, 1997; Svanberg and Holmberg, 2004b; Ding et al., 2016b,a). Cure Hardening Instantaneous Linear Elastic (CHILE) models have been widely used in the literature to represent the elastic stiffness evolution with

the temperature and degree of cure. Several authors have shown that CHILE models can satisfactorily predict the geometrical distortion developed in simple geometries during the manufacturing process (Zobeiry, 2006; Ding et al., 2016a; Benavente et al., 2017b). The main drawback of CHILE models is that they cannot account for stress relaxation occurring during manufacturing and cool-down (Wang et al., 1992; White and Hahn, 1992; Kim and White, 1997). Moreover, Zobeiry (2006) showed that CHILE models were not suitable to predict stresses evolution during the post-curing process.

Degree of cure- and temperature-dependent linearly viscoelastic models (O'Brien et al., 2001; Courtois et al., 2016) has been used to describe composites viscoelastic behavior and can account for stress relaxation (Wang et al., 1992; White and Hahn, 1992; Kim and White, 1997). However their use has been limited by the fact that an extensive material characterization and a complex numerical implementation are needed.

Recent studies (Zobeiry, 2006; Ding et al., 2016a; Benavente et al., 2017b) have shown that elastic and viscoelastic models can predict similar residual stresses and geometrical distortion in corner parts and asymmetric plates after specific manufacturing cycles. However, their use and limitations in complex cure cycles, where the part is submitted to a free-standing post-curing treatment, have not been reported yet, to the best of the authors knowledge.

The purpose of this work was to compute the overall geometrical distortion evolution occurring during the RTM manufacturing and free standing post-curing processes of an asymmetric plate and a L-shaped part. To that end, degree of cure- and temperature-dependent elastic and viscoelastic models representing the mechanical behavior of composites reinforced with three dimensional fabric have been implemented into ABAQUS 6.14. The predictions obtained with the elastic and viscoelastic models were compared to experimentally measured data of asymmetric plates submitted to different post-curing conditions. The limitations of the implemented models to compute the process induced distortion in complex cure cycles (in-mold manufacturing and free-standing post-curing) have been studied.

The paper is organized as follows. Section 2 deals with the background on process induced distortion evolution during the post-curing process. Section 3 deals with the experimental background while the implementation theory and methodology used for the finite element model are presented in Section 4. The results and conclusions are presented in Sections 5 and 6, respectively.

6.2 Origins of process induced distortion during post-curing

Several authors have observed that submitting a composite part to a free-standing post-

curing process could increase the post-manufacturing distortion by up to 30 % (White and Hahn, 1993; Svanberg and Holmberg, 2001; Hubert et al., 2002; Pazdzior et al., 2004). White and Hahn (1993) investigated the effect of the post-curing process on plates' distortion by subjecting partially cured specimens to a four-hour dwell above their glass transition temperatures. The results revealed that the plates' curvature increased after the post-curing process for all the studied specimens. White and Hahn (1993) suggested that this increment was caused by an additional chemical shrinkage. Svanberg and Holmberg (2001) measured the spring-in evolution prior and after a four-hour post-curing process in L-shaped parts. The results showed that the specimens with a higher in-mold cure temperature, and hence a higher degree of cure prior the post-curing process, presented a larger increase of the spring-in after post-curing. The authors concluded that these results stem from additional mechanisms occurring during the post-curing process that induce the increase of the part's distortion. It was suggested that the increase of the process induced distortion in completely cured parts was caused by the total or partial release of the "frozen-in" strains. Kominar (1996) stated that the stresses developed during the manufacturing cannot be released during the in-mold manufacturing, thus leaving the part with "unreleased" or "frozen-in" strains. The "frozen-in" strains can be totally or partially released by heating a free standing plate above its glass transition temperature, increasing its distortion after a post-curing process Kim and Daniel (2002); Svanberg and Holmberg (2004a); Kim (2004); Minakuchi (2015).

Benavente et al. (2017a) characterized the process induced distortion during and after different free-standing post-curing conditions in completely cured asymmetric plates reinforced by a three-dimensional (3D) fibre architecture. The results showed that the plates' distortion was time and temperature dependent and that it increased after a free-standing post-curing below their glass transition temperature. The authors demonstrated that the increase in process induced distortion during post-curing of completely cured parts was caused by creep strains occurring at high temperature, and not by the "frozen-in" strains.

6.3 Experimental methodology

Six asymmetric plates of 410 mm × 120 mm × 6,7 mm with a [0/90] lay-up configuration were manufactured in a RTM steel mold. An aerospace Diglycil Ether of Bisphenol F (DGEBF) epoxy resin and a three-Dimensional (3D) woven interlock fabric with IM10 carbon fibers from Hexcel Fabrics were used as matrix and reinforcement, respectively. The fabric was composed by four interlock layers and had an unbalanced architecture where 70 % of the fibers were aligned along the warp direction.

A cure cycle with two isotherm dwell of one hour at 160 °C followed by two hours at 180 °C

was adopted to ensure complete curing Pupin et al. (2017). The plates were then cooled down inside the closed mold. Once the laminates centers reached 100 °C, the mold was opened and the plates were released and let cool-down by natural convection to room temperature.

Resin samples from the composite plates were analyzed using a Q-2000 Modulated Differential Scanning Calorimeter (M-DSC) from TA Instruments. The results revealed that the plates were completely cured with a degree of cure of 99.2 % and a final glass transition temperature of 156 °C.

Finally, the plates' deflections were measured at room temperature after the manufacturing process by an electronic Linear Variable Differential Transformer (LVDT).

After manufacturing, the plates were submitted to different free-standing thermal cycles to characterize the effect of creep strains. The curvature evolution of the plates was characterized during the different thermal cycles by digital image analysis Benavente et al. (2017a). The effect of the isotherm duration and temperature on the plates' curvature was characterized by submitting the plates to 30- and 150-minute isotherms at temperatures ranging from 70 to 220 °C. The plates were removed from the oven and cooled by natural convection down to room temperature, after each thermal cycle. The plates' deflection was finally measured with a LVDT at room temperature.

6.4 Finite element model

The modified Voigt notation was adopted in this section to represent tensors. Symmetric second-order and fourth-order tensors were expressed as a six-component vector and a 6 × 6 matrix, respectively. Scalar quantities were denoted by light-lower case letters (*i.e.,* a, α, E), second order tensors were denoted by boldfaced lower case Greek letters (*i.e.,* $\boldsymbol{\sigma}$, $\boldsymbol{\varepsilon}$) and fourth order tensors were denoted by boldfaced capital Roman letters (*i.e.,* $\mathbf{C}$).

6.4.1 Implementation background

The thermo-chemo-mechanical phenomena inducing residual stresses during the manufacturing process have been generally modeled by a sequentially modular approach (Loos and Springer, 1983; Svanberg and Holmberg, 2004b; Zeng and Raghavan, 2010; Baran et al., 2016). The modular approach used for modeling the RTM process consisted first in solving a coupled thermo-chemical analysis yielding the temperature and degree of cure distribution through the part, at each time increment. The temperature and degree of cure as a function of time were then implemented into a mechanical model to compute the composites mechanical properties yielding to the residual stresses and geometrical distortion. The diagram of

the modeling approach used in this work is shown in Figure 6.1.

Coupled thermo-chemical model

Fourier's heat transfer and cure kinetics equations have been combined to compute the temperature and degree of cure evolution during the manufacturing process as (Bogetti and Gillespie Jr, 1992; Kim and White, 1997; Joshi et al., 1999)

$$\rho_c \zeta_{pc} \frac{\mathrm{d}T}{\mathrm{d}t} = \frac{\mathrm{d}}{\mathrm{d}x_i}\left(\kappa_{ij}\frac{\mathrm{d}T}{\mathrm{d}x_j}\right) + \dot{Q}_r \qquad \text{(no sum on } c \text{ index)} \tag{6.1}$$

where T was the temperature, ρ_c was the composite density, ζ_{pc} was the composite specific heat at a constant pressure and κ_{ij} was the composite thermal conductivity tensor. The internal heat generation, $\dot{Q}_r$, represented the exothermic reaction associated to the resin curing as

$$\dot{Q}_r = \rho_r \left(1 - V^f\right) H_r \frac{\mathrm{d}\alpha}{\mathrm{d}t} \tag{6.2}$$

where ρ_r, V^f, H_r were the resin's density, the fabric's volume fraction and the total reaction's enthalpy, respectively. α was the degree of cure and $\mathrm{d}\alpha/\mathrm{d}t$ the cure reaction rate.

Pupin et al. (2017) has recently modeled the kinetic's cure reaction of a DGEBF epoxy resin by a Kamal-Sourour phenomenological model as

$$\frac{\mathrm{d}\alpha}{\mathrm{d}t} = \left(k_1 + k_2\alpha^m\right)(1-\alpha)^n F(\alpha) \tag{6.3}$$

where m and n were a material constant and k_1 and k_2 were the chemical reaction rate constants described by Arrhenius equation as

$$k_i = A_i \exp\left(\frac{-E_i}{RT}\right) \tag{6.4}$$

where R was the gas constant, A_i was the Arrhenius constant and E_i was the Arrhenius activation energy. Finally, $F(\alpha)$ was an empirical function that described the diffusion phenomena occurring at the end of the reaction and was expressed as

$$F(\alpha) = \frac{1}{1 + \exp(B_1(\alpha - B_2))} \tag{6.5}$$

where B_1 and B_2 were material constants accounting for the chemical diffusion. The input properties for the cure kinetics, the conductivity and specific heat models were normalized for confidentiality reasons and are presented in Appendix A

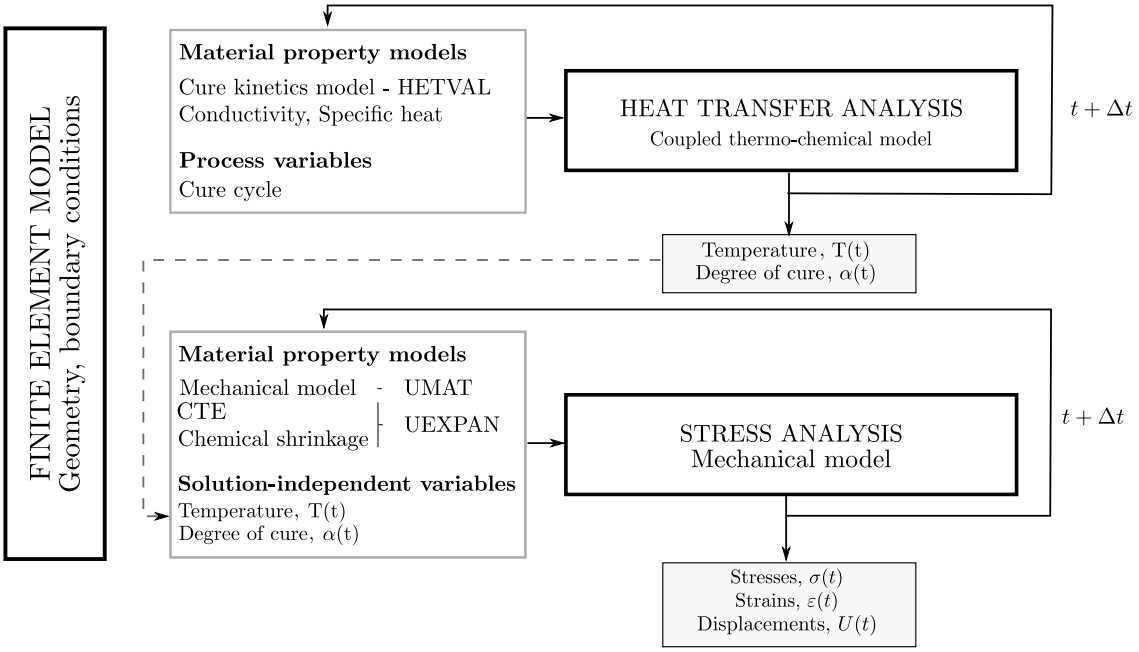

Figure 6.1 Diagram flow of the thermo-chemical and mechanical modular approach

Mechanical model

The mechanical properties input in the models were obtained from a three-dimensional numerical multi-scale homogenization strategy and will be the focus of a forthcoming paper. The normalized homogenized properties are presented in Appendix A.

Non-mechanical strains

The thermal strains tensor, $\boldsymbol{\varepsilon}_{TH}^{NM}$, has been calculated as (Bogetti and Gillespie Jr, 1992; Svanberg and Holmberg, 2004b; Ding et al., 2016b)

$$\boldsymbol{\varepsilon}_{TH}^{NM}(t + \Delta t) = \boldsymbol{\varepsilon}_{TH}^{NM}(t) + \boldsymbol{\theta}^{c}(t)\Delta T \tag{6.6}$$

where ΔT was the temperature increment within the time step and $\boldsymbol{\theta}^{c}$ was the composite's coefficient of thermal expansion tensor and was expressed as

$$\boldsymbol{\theta}^{c} = \begin{cases} \boldsymbol{\theta}_{g}^{c} & T < T_{g}(\alpha) \\ \boldsymbol{\theta}_{r}^{c} & T \geq T_{g}(\alpha) \end{cases} \tag{6.7}$$

where $\boldsymbol{\theta}_{g}^{c}$ and $\boldsymbol{\theta}_{r}^{c}$ were the composite's coefficients of thermal expansion in the glassy and rubbery states, respectively. $T_{g}(\alpha)$ was the degree of cure-dependent glass transition temperature

obtained from the DiBenedetto equation as

$$\frac{T_g(\alpha) - T_g^{(0)}}{T_g^{(\infty)} - T_g^{(0)}} = \frac{\lambda\alpha}{1-(1-\lambda)\alpha} \tag{6.8}$$

where T_g^0 and $T_g^{(\infty)}$ were the uncured ($\alpha = 0$) and fully cured ($\alpha = 1$) resin's glass transition temperatures, respectively, and λ was a material constant.

The strains associated with chemical shrinkage, $\boldsymbol{\varepsilon}_C^{NM}$, were defined as (Bogetti and Gillespie Jr, 1992; White and Kim, 1998; Rabearison et al., 2011)

$$\boldsymbol{\varepsilon}_C^{NM}(t+\Delta t) = \boldsymbol{\varepsilon}_C^{NM}(t) + \boldsymbol{\beta}^c(t)\Delta\alpha \tag{6.9}$$

where $\Delta\alpha$ was the degree of cure increment within the time step and $\boldsymbol{\beta}^c$ was the composite's coefficient of chemical shrinkage.

Mechanical strains

Based on the macroscopic homogenized mechanical properties, elastic and linearly viscoelastic models were developed and implemented into ABAQUS by two UMAT user subroutines to predict the mechanical strains. The stress tensor at the end of the increment, $\boldsymbol{\sigma}(t+\Delta t)$, and the Jacobian matrix, $\frac{\partial\Delta\boldsymbol{\sigma}}{\partial\Delta\boldsymbol{\varepsilon}}$, required to compute the mechanical stresses and strains are detailed in the following subsections.

Elastic model

The stresses $\boldsymbol{\sigma}$ are related to the strains $\boldsymbol{\varepsilon}$ in a linearly elastic solid through

$$\boldsymbol{\sigma} = \mathbf{C} : \boldsymbol{\varepsilon} \tag{6.10}$$

where $\mathbf{C}$ is the stiffness tensor (Harper and Weitsman, 1981; Loos and Springer, 1983; Bogetti and Gillespie Jr, 1992). A Cure Hardening Instantaneous Linear Elastic (CHILE) model, first introduced by Johnston (1997), has been widely used in the literature to account for the stiffness evolution with the degree of cure and temperature (Fernlund et al., 2002; Ruiz and Trochu, 2005b; Ersoy et al., 2005; Ding et al., 2016a). A simplified cure hardening linearly elastic model was developed to describe the composite's stiffness tensor evolution with the

temperature and degree of cure as

$$\mathbf{C}_e(T^*) = \begin{cases} \mathbf{C}^{(0)} & T^* < T_0 \\ \mathbf{C}_e^{(1)} + \left(\mathbf{C}^{(0)} - \mathbf{C}_e^{(1)}\right) \frac{T^* - T_1}{T_0 - T_1} & T_0 \leq T^* < T_1 \\ \mathbf{C}^{(\infty)} + \left(\mathbf{C}_e^{(1)} - \mathbf{C}^{(\infty)}\right) \frac{T^* - T_\infty}{T_1 - T_\infty} & T_1 \leq T^* < T_\infty \\ \mathbf{C}^{(\infty)} & T^* \geq T_\infty \end{cases} \tag{6.11}$$

with $T^* = T - T_g(\alpha)$ and where $\mathbf{C}^{(0)}$ and $\mathbf{C}^{(\infty)}$ were the orthotropic stiffness tensors at glassy and rubbery states, respectively, and $\mathbf{C}_e^{(1)}$, T_0, T_1 and T_∞ were material constants.

The stress tensor at time $t + \Delta t$ and Jacobian matrix, $\frac{\partial \Delta \boldsymbol{\sigma}}{\partial \Delta \boldsymbol{\varepsilon}}$, for the elastic model were implemented by Benavente et al. (2017b) as

$$\begin{aligned} \boldsymbol{\sigma}(t + \Delta t) &= \boldsymbol{\sigma}(t) + \Delta \boldsymbol{\sigma} \\ &= \boldsymbol{\sigma}(t) + \mathbf{C_e}(T^* + \Delta T^*) : \Delta \boldsymbol{\varepsilon} + \Delta \mathbf{C_e}(T^*) : \boldsymbol{\varepsilon} \end{aligned} \tag{6.12a}$$

$$\frac{\partial \Delta \boldsymbol{\sigma}}{\partial \Delta \boldsymbol{\varepsilon}} = \mathbf{C_e}(T^* + \Delta T^*) \tag{6.12b}$$

Linearly viscoelastic model

Courtois et al. (2016) have recently adapted the linearly viscoelastic theories derived from a rigorous thermodynamics framework (Biot, 1954; Lévesque et al., 2008) for a temperature and degree of cure dependent linearly viscoelastic model expressed as

$$\boldsymbol{\sigma}(t) = \mathbf{L}^{(1)} : \boldsymbol{\varepsilon}(t) + \mathbf{L}^{(2)} : \boldsymbol{\chi}(t) \tag{6.13a}$$

$$\mathbf{A} : \dot{\boldsymbol{\chi}} + \mathbf{L}^{(3)} : \boldsymbol{\chi} + \left(\mathbf{L}^{(2)}\right)^T : \boldsymbol{\varepsilon} = 0 \tag{6.13b}$$

where $\boldsymbol{\chi}$ were hidden variables,

$$\mathbf{L} = \begin{bmatrix} \mathbf{L}^{(1)} & \mathbf{L}^{(2)} \\ (\mathbf{L}^{(2)})^T & \mathbf{L}^{(3)} \end{bmatrix} \tag{6.14}$$

where $\mathbf{L^{(1)}}$ and $\mathbf{L^{(3)}}$ must be positive definite to meet the first and second principles of thermodynamics. $\mathbf{A}$ was a symmetric and positive semi-definite matrix, expressed as

$$\mathbf{A} = \frac{1}{a_T(T, \alpha)} \mathbf{B}^{-1} \tag{6.15}$$

where $a_T(T, \alpha)$ was the degree of cure- and temperature-dependent shift factor. $\mathbf{B}$ was a N $\times$ N identity matrix.

The solution of differential Eq. 6.13 yielded (Luk-Cyr et al., 2013; Courtois et al., 2016)

$$\boldsymbol{\sigma}(t) = \mathbf{C}^{(\infty)} : \boldsymbol{\varepsilon} + \int_0^t \sum_{k=1}^{N} \mathbf{C}^{(k)} \exp\left[-\omega^{(k)}\left(\xi - \xi'\right)\right] : \frac{\mathrm{d}\boldsymbol{\varepsilon}}{\mathrm{d}\tau}\mathrm{d}\tau \tag{6.16}$$

where $\mathbf{C}^{(k)}$ were the relaxations tensors associated to the inverted relaxation times $\omega^{(k)}$ and $\xi - \xi'$ was the reduced time expressed by the Time Temperature Superposition Principle as

$$\xi - \xi' = \int_0^t \frac{\mathrm{d}\gamma}{a_T(T(\gamma), \alpha(\gamma))} - \int_0^\tau \frac{\mathrm{d}\gamma}{a_T(T(\gamma), \alpha(\gamma))} \tag{6.17}$$

The degree of cure- and temperature-dependent viscoelastic behavior of the composite used in this work was computed using the viscoelastic correspondence principle (Lévesque et al., 2007) and the numerical multi-scale homogenization method explained above. The composite was assumed to have an orthotropic linearly viscoelastic behavior composed by thirteen relaxation times, one per decade, ranging from 10^{-9} to 10^{3} min. The degree of cure- and temperature-dependence was accounted for through the shift factor as

$$\log(a_T(T, \alpha)) = \begin{cases} \frac{H_1}{(\ln 10)R}\left(\frac{1}{T} - \frac{1}{T_g(\alpha)}\right) & T \geq T_g(\alpha) \\ \frac{H_2}{(\ln 10)R}\left(\frac{1}{T} - \frac{1}{T_g(\alpha)}\right) & T < T_g(\alpha) \end{cases} \tag{6.18}$$

where $H_1 > H_2$ were the resin's activation energies [KJ/mol] calculated by Courtois et al. (2016) and the temperature was expressed in Kelvins.

The stresses at time $t + \Delta t$ and Jacobian matrix, $\frac{\partial \Delta \boldsymbol{\sigma}}{\partial \Delta \boldsymbol{\varepsilon}}$, were computed using a backward Euler first-order Finite Difference by Crochon (2014) as

$$\boldsymbol{\sigma}(t + \Delta t) = \left(\mathbf{L}^{(1)} + \mathbf{L}^{(2)} : \mathbf{W}^{(2)}\right) : \boldsymbol{\varepsilon}(t + \Delta t) + \mathbf{L}^{(2)} : \mathbf{W}^{(1)} : \boldsymbol{\chi}(t) \tag{6.19a}$$

$$\frac{\partial \Delta \boldsymbol{\sigma}}{\partial \Delta \boldsymbol{\varepsilon}} = \mathbf{L}^{(1)} + \mathbf{L}^{(2)} : \mathbf{W}^{(2)} \tag{6.19b}$$

where

$$\mathbf{W}^{(1)} = \left(\mathbf{I} + \Delta t \mathbf{A} : \mathbf{L}^{(3)}\right)^{-1} \tag{6.20a}$$

$$\mathbf{W}^{(2)} = -\Delta t \mathbf{W}^{(1)} : \mathbf{A} : \left(\mathbf{L}^{(2)}\right)' \tag{6.20b}$$

where Δt was the time increment and $\mathbf{I}$ a N $\times$ N identity matrix.

6.4.2 Methodology

Asymmetric plate

The geometrical distortion triggered by the residual stresses developed in a flat plate with a [0/90] lay-up configuration during the RTM and free standing post-curing processes was computed using the modular approach described in Figure 6.1.

Due to the symmetry of the geometry, only one fourth of the plate was modeled, as shown in Figure 6.2. The [0/90] lay up configuration was taken into account by two equidistant sections through the thickness with different orientation configuration.

The process simulation was divided into the following three steps

- **Segment 1 : In-mold manufacturing.** The plate was submitted to a thermal cycle inside the rigid mold.
  - Thermo-chemical model : The temperature measured experimentally by Benavente et al. (2017a) during the two-dwell cure cycle and cool-down to 100 °C was imposed as thermal boundary conditions on the plate's surface.
  - Mechanical model : The plate was assumed to be fully constrained by the mold, as shown in Figure 6.2.
- **Segment 2 : Free-standing cool-down.** The plate was released from the mold and let cool-down to room temperature.
  - Thermo-chemical model : The natural convection cool-down was simulated by a film coefficient and sink temperature of 7.5 $Wm^{-2}K^{-1}$ and 25 °C, respectively, to reproduce the thermal evolution measured experimentally (Benavente et al., 2017a).
  - Mechanical model : The mechanical boundary conditions were modified to ensure free standing conditions while preventing rigid body motions, as shown in Figure 6.2.
- **Segment 3 :Free-standing post-curing cycle.** The isothermal free-standing post-curing was simulated next.
  - Thermo-chemical model : A surface film condition with a 24 $Wm^{-2}K^{-1}$ film coefficient and the isotherm temperature as the sink temperature was imposed during the heat-up and isotherm to simulate the preheated convection oven. The natural convection cool down was simulated using the conditions used in segment 2.
  - Mechanical model : The boundary conditions were identical to those of Segment 2.

The effect of the post-curing temperature and duration on the geometrical distortion was

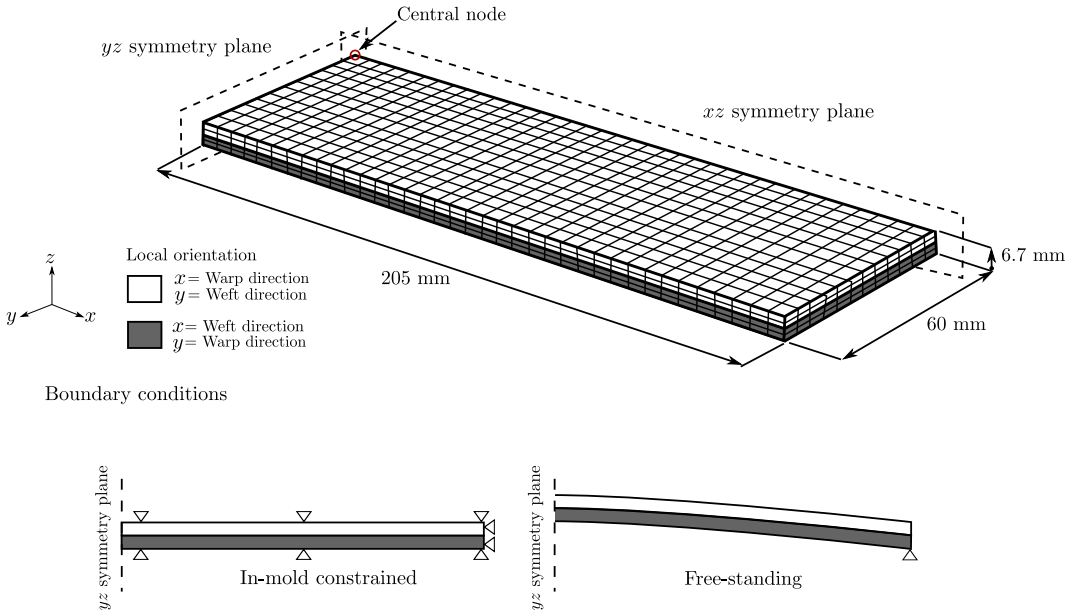

Figure 6.2 Geometry model, mesh and boundary conditions used for the asymmetric plate finite element simulations

studied through 45 simulations, the parameters of which can be found in Table 6.1. Seven 30-minute and three 150-minute isotherm simulations were carried out with the elastic model to study the effect of the post-curing temperature and duration. The isotherm temperature, ranging from 70 to 150 °C, and its duration, ranging from 30 to 200 minutes, have been modified during the different simulations carried out using the viscoelastic model to study the effect of creep strains occurring below the glass transition temperature during the post-curing process.

Table 6.1 Studied post-curing parameters, post-curing temperature and isotherm length, for the elastic and viscoelastic models

	Temperature	**Total time**	**Simulations**
Elastic	from 70 to 150 °C	30 min	7
	140 °C	150 min	1
Viscoelastic	from 70 to 120 °C	30 min and 150 min	8
	130, 140 and 150 °C	30 to 200 min	27

L-shaped part

A numerical study of the spring-in developed in L-shaped parts during the manufacturing and post-curing processes have been carried out following the methodology explained in 6.4.2. The effect of the post-curing temperature was studied through seven simulations, all of them carried out using the viscoelastic model. The isotherm duration was fixed to 30 minutes while the temperature, ranging from 70 to 150 °C, was modified during the different simulations.

Figure 6.3 shows the geometry, mesh and local orientations used in the L-shaped part model. The part was reinforced by a single ply of 3D woven reinforcement with the warp tows oriented longitudinally along the part, as shown in Figure 6.3.

The aim of the simulation in a L-shaped part was to validate if the increase of the spring-in angle measured experimentally by Svanberg and Holmberg (2001) after submitting the composite part to a free standing post-curing could be simulated using a linearly viscoelastic model.

6.5 Results

6.5.1 Asymmetric plate

The numerically predicted deflections of an asymmetric plate during different thermal cycles using the elastic and viscoelastic models are compared to the experimental measurements presented by Benavente et al. (2017a). The stresses and geometrical distortion evolution during the manufacturing process of asymmetric plates were presented and discussed in a previous paper Benavente et al. (2017b). The results revealed that the geometrical distortion predicted by the elastic and viscoelastic models after the studied RTM cycle led to 3.2 and 1.5 % discrepancies, respectively, when compared with the experimental data. However, it is important to note that the elastic model did not account for the stress relaxation that can occur during the RTM process, thus other manufacturing cycles could lead to different results. The results obtained numerically and experimentally during and after the post-curing process (segment 3) are presented and discussed herein.

The presented results were normalized by the plate's curvature measured or calculated at room temperature after the manufacturing process for the experimental and numerical data, respectively. The error bars represent 95 % confidence intervals on mean for the six samples.

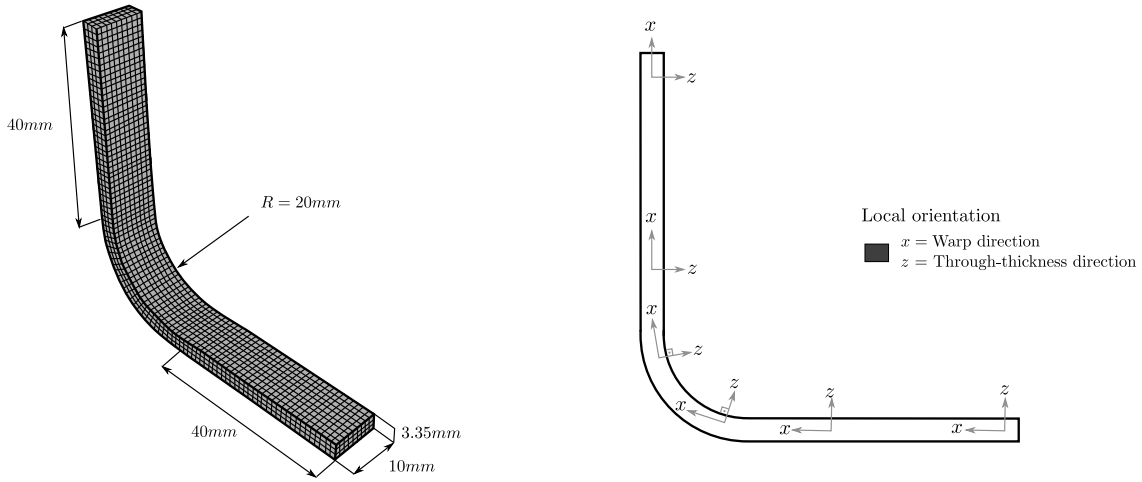

Figure 6.3 Geometry model, mesh (left) and local orientations (right) used for the L-shaped part finite element simulations

Total deformation

The curvature of asymmetric plates reinforced with 3D woven interlock fabric measured by Benavente et al. (2017a) after fabrication (T_c = 25 °C) and after being submitted to 30 minutes free-standing isotherms at different temperatures are shown in Figure 6.4 and compared with the predicted values using the elastic and viscoelastic models.

The experimental data revealed that the curvature increases after submitting the completely cured asymmetric plates to a 30-minute isotherm above 130 °C. Benavente et al. (2017a) suggested that this increment was caused by creep strains occurring during the isotherm at high temperatures. As expected, the numerical results obtained with the elastic model predicted that the geometrical distortion remained constant after submitting the plate to a 30-minute isotherm at any of the studied temperatures. On the other hand, the results obtained with the viscoelastic model predicted a curvature increment of 10 % after submitting the plate to a 30-minute isotherm at 150 °C, which was in agreement with the experimental data. Figure 6.4 shows that the elastic model predicted more accurately the curvature evolution during the 30-minute isotherm at low temperatures. This can be explained by the fact that the combination of temperature and isotherm duration did not yield significant creep strains that could increase the plates' curvature. However, the numerical results revealed that the plate's curvature evolution after being reheated at high temperatures (above 130 °C) can be predicted using a viscoelastic model.

Figure 6.5 shows the normalized curvature measured experimentally after submitting the plates to 150-minute free-standing isotherms at different temperatures. Two samples were

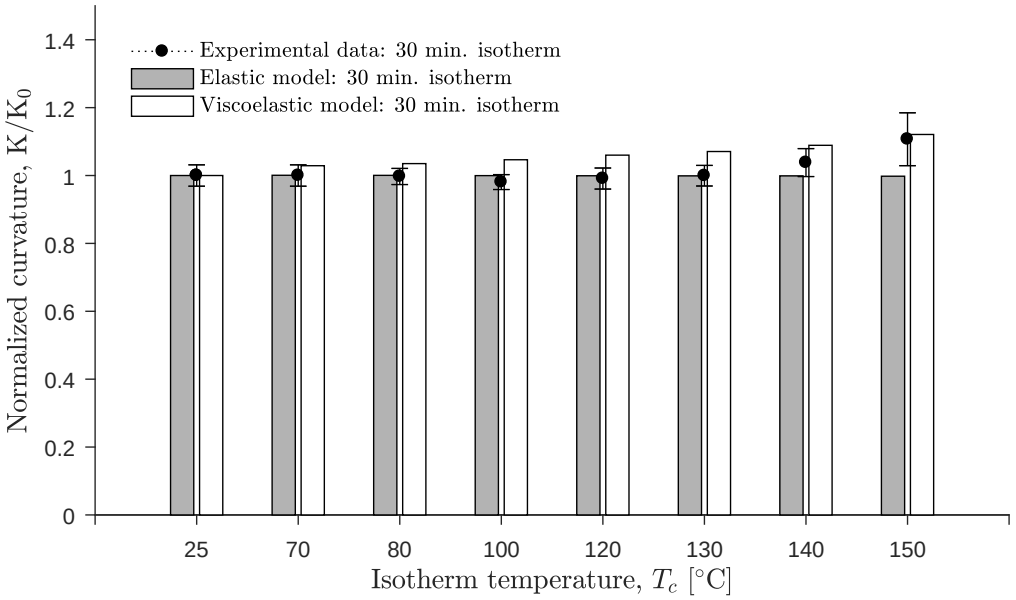

Figure 6.4 Comparison of the normalized curvature at room temperature of [0/90] plates after 30-minute at isotherm temperature, T_c, obtained experimentally and numerically with the elastic and viscoelastic models

experimentally characterized after being submitted to a 150-minute free-standing isotherm at each isotherm temperature to characterize the time-temperature effect on the plate's curvature. The experimental results revealed that, for the same isotherm temperature T_c, the curvature increased for longer isotherms (i.e. $T_c = 140°C$). This phenomenon can be explained by the fact that longer isotherms lead to higher creep strains, and hence a higher increase of the plates curvature. The numerical results revealed that the elastic model predicted that the curvature did not evolve with any post-curing cycle. On the other hand, the viscoelastic model captured the time-dependent curvature evolution phenomenon observed experimentally. These results confirm that the increase in the process induced distortion during post-curing is caused by the creep strains and not by the release of "frozen-in" strains or an extra resin curing, as proposed by Svanberg and Holmberg (2001) and White and Hahn (1993) . Thus, a viscoelastic model is needed to predict the plate's process induced distortion after being submitted to a free-standing post-curing cycle.

Figure 6.6 shows the plate's curvature evolution at room temperature after being submitted to different isotherms whose durations ranged from 30 to 200 minutes, at 130 °C, 140 °C and 150 °C predicted by the viscoelastic model. These results show that the general trend of the curvature after being submitted to different thermal cycles was well predicted with by the viscoelastic model. However, it also shows that the viscoelastic model overestimated

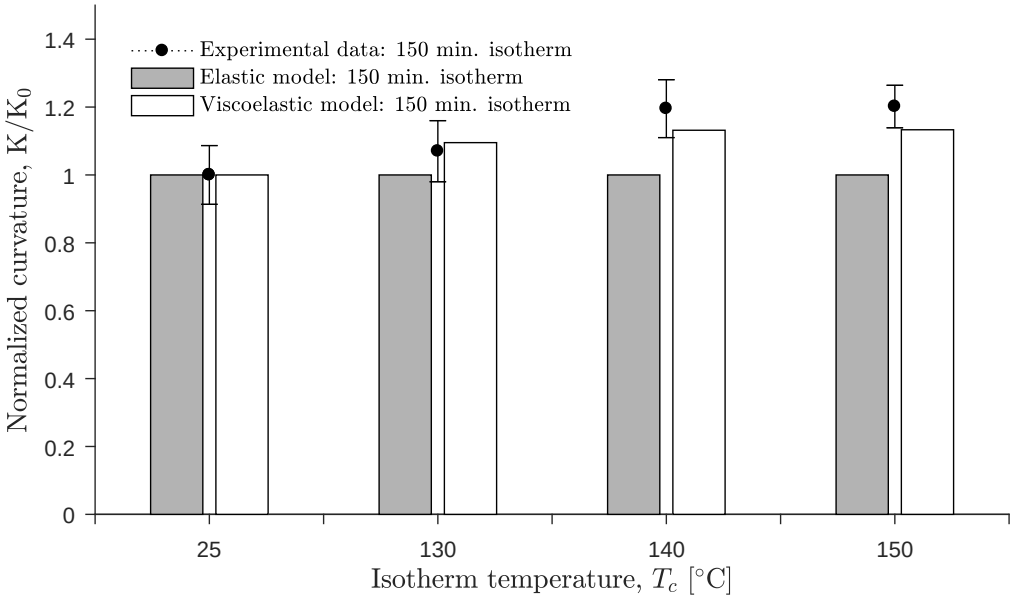

Figure 6.5 Comparison of the normalized curvature at room temperature of [0/90] plates after 150-minute at isotherm temperature, T_c obtained experimentally and numerically with the elastic and viscoelastic model

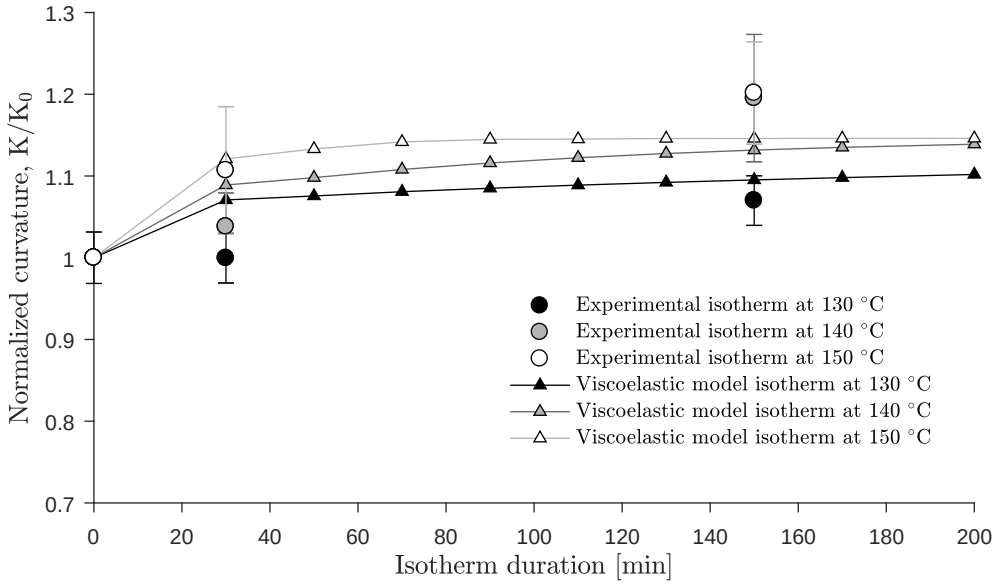

Figure 6.6 Relative curvature increment predictions at room temperature after being submitted at different isotherms lengths at 130 °C, 140 °C and 150 °C

by 7 % the creep behaviour at low temperatures (130 °C) in the 30-minute isotherms when compared to the experimental measurements, while it underestimated it by 5 to 7 % at high temperatures (140 and 150 °C) for the 150-minute isotherms. On-going works focus on improving the viscoelastic model's accuracy.

The numerical results suggest that a stabilized creep strain could be achieved after 100 minutes at 150 °C. Thus, submitting the plate to a longer isotherm did not increase the amount of curvature. This result is in agreement with the experimental data where a stabilized creep strain was achieved after a 150-minute dwell at 150 °C Benavente et al. (2017a).

The figure also reveal that at 130 °C the creep strains evolution with time predicted by the viscoelastic model is relatively slow, increasing the curvature by only 3 % from 30 to 200 minutes. However, a more significant viscoelastic behavior was computed at 150 °C where the curvature increased rapidly at first (isotherms from 30 to 100 minutes) and reached a stabilized curvature soon after. The analysis carried out at 140 °C showed that the curvature was highly dependent of the isotherm duration.

These results confirm that creep strains can be stabilized during an isotherm at a given temperature. Thus, a reduction on the geometric distortion dispersion between different parts would be expected if the post-curing heating parameters were to be designed to achieve the stabilized creep strains. On the other hand, time-dependent distortion could occur over long periods of time at lower temperatures if the post-curing did not stabilize the creep strains. This could lead to important parts recalls at the production floor.

Time-temperature deformation

Figure 6.7 shows the curvature evolution for the 150 minutes isotherms at 140 °C measured experimentally and predicted by the elastic and viscoelastic models.

The studied isotherms can be divided in two phases, namely

- **Segment 1 :** A heating phase where the plate's curvature decreased as the temperature increased. This resulted from the material's thermo-elastic behavior related to the coefficient of thermal expansion. Figure 6.7 shows that the curvature in the asymmetric plate was reduced by 90 % when it was heated to 140 °C, for the viscoelastic model and the experimental data.
- **Segment 2 :** An isotherm phase where the temperature was held constant. A curvature increase was measured experimentally over time, caused by a creep phenomenon. This phenomenon was also predicted by the viscoelastic model. On the other hand, the elastic model predicted a constant curvature once the temperature was stabilized.

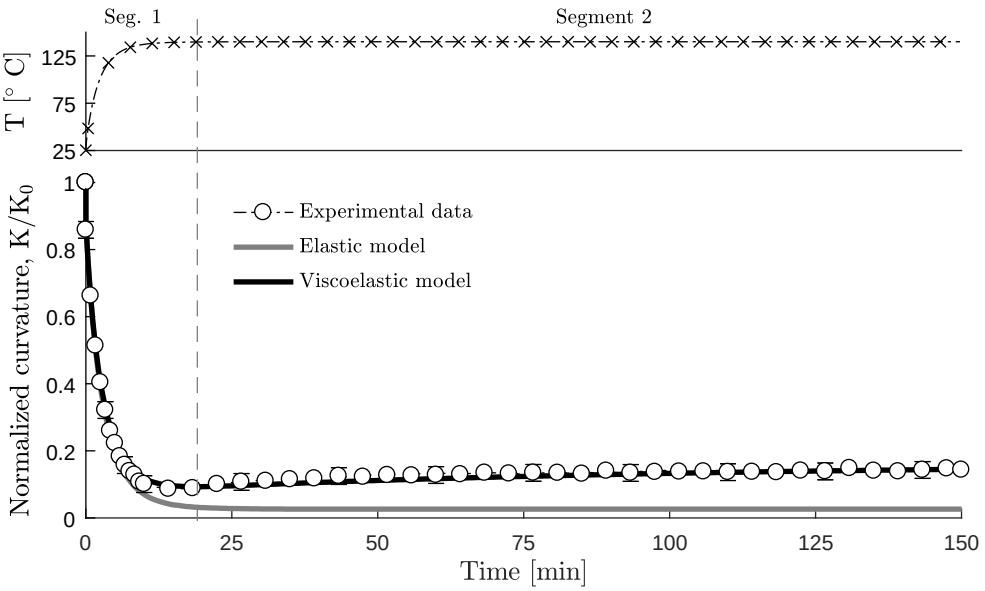

Figure 6.7 Temperature and curvature evolution of a [0/90] plate during the heating up and isotherm at 140 °C for 150 minutes measured experimentally and predicted by the elastic and viscoelastic models

This result confirmed the hypothesis presented by Benavente et al. (2017a) where it was stated that the increment in the curvature during the post-curing process was related to the composite's viscoelastic behavior at high temperature.

Figure 6.8 shows the curvature presented in Figure 6.7 with the temperature evolution during the heating and isotherm phases. The results show that the numerical models predict accurately the thermo-elastic distortion measured experimentally in asymmetric plates. Figure 6.8 also shows that the experimental and numerical viscoelastic model presented a non-linear relationship between the temperature and the curvature during the heating phase above 80 °C. On the other hand, the elastic model predicted a linear thermo-elastic distortion, as it is expected from a purely thermo-elastic analysis, from 20 to 140 °C. These results suggested that instantaneous creep behavior occurred during the heating phase. The inset of Figure 6.8 also shows that the experimental data and the viscoelastic model predicted the same curvature tendency at 140 °C.

The measured curvature evolution during the 150-minute isotherms at 130, 140 and 150 °C are presented in Figure 6.9 and compared with the numerical results obtained with the viscoelastic model. The results reveal that the viscoelastic model predicts accurately the curvature tendency over time during the 150 minutes isotherm at 130 and 140 °C. However, the creep strains predicted at 150 °C was much lower than those measured experimentally. Further analyses have to be carried out to improve the theoretical homogenization model,

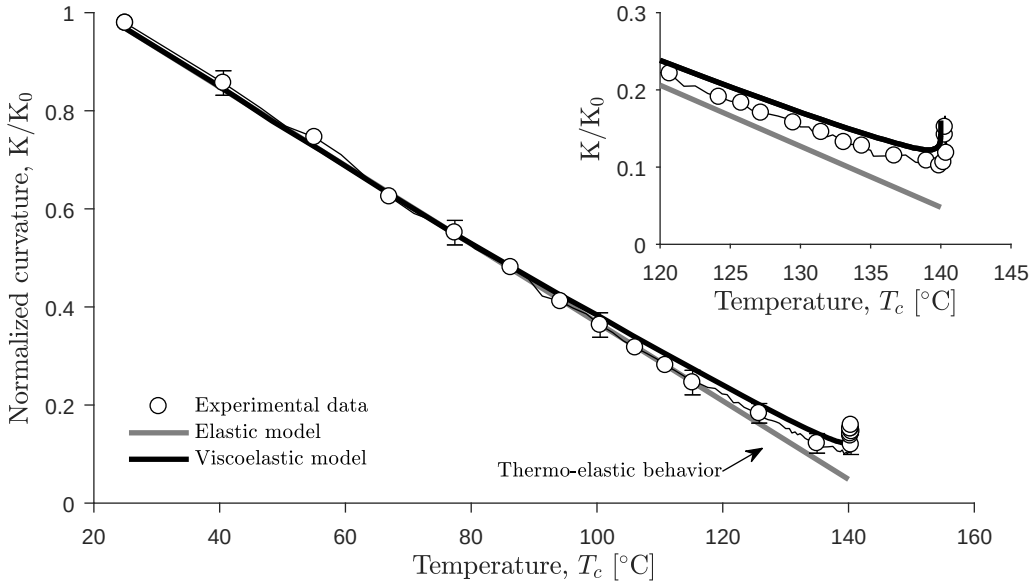

Figure 6.8 Curvature evolution of a [0/90] plate during 150 minutes isotherm at 140 °C measured experimentally and predicted by the elastic and viscoelastic models. Inset : Thermo-elastic and creep behavior from 100 to 140 °C

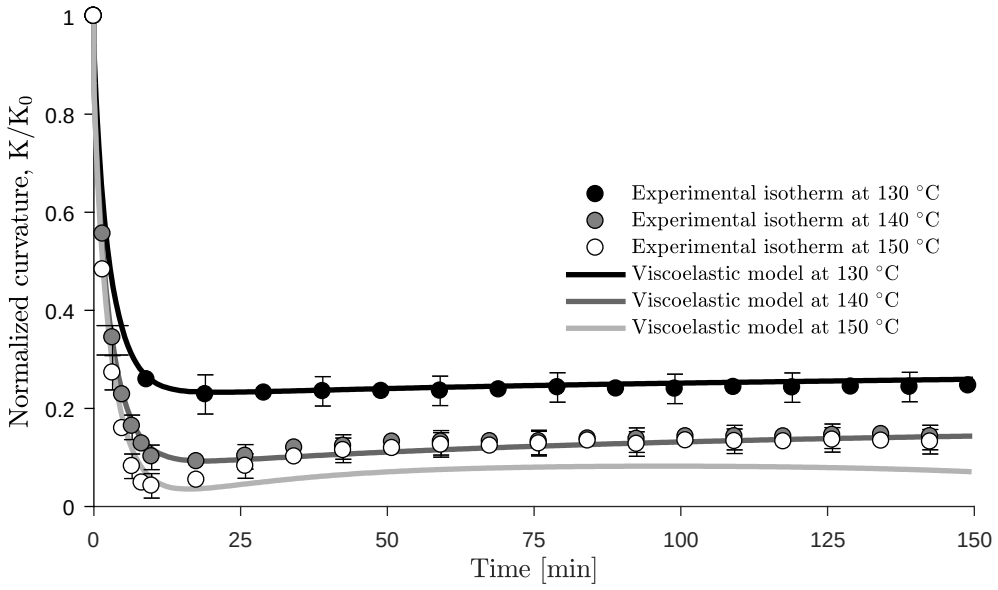

Figure 6.9 Curvature evolution of a [0/90] plate during the heating up and 150 minutes isotherm at 130, 140 and 150 °C measured experimentally and predicted by the viscoelastic models

and hence the viscoelastic model. Nevertheless, the FE model captured the overall trend as well as the time-scale over which the creep phase occurred.

It should be noted that Benavente et al. (2017a) experimentally observed that residual stresses induce time- and temperature-dependent creep strains in asymmetric plates. The viscoelastic model used in this work reproduced such a behavior. Furthermore, creep strains can increase by up to 20 % the geometrical distortion of asymmetric plates. Neglecting the viscoelastic phenomenon during the post-curing or in parts submitted to thermal cycles during their service lives can be detrimental for high precision applications.

6.5.2 L-shaped part

Figure 6.10 shows the original L-shaped and predicted geometrical distortion developed in the part after manufacturing (left) and following a 30-minute isotherm at 150 °C (right). The displacement was normalized by the maximum displacement in the x direction after the 30-minute isotherm at 150 °C. The spring-in angle was calculated by trigonometry from the nodal displacement shown in Figure 6.10. A spring-in angle of 0.67° was predicted by the viscoelastic model after the manufacturing process. This result is in agreement with the spring-in typically measured in the literature that ranges between 0.5 to 2°. In this case, the spring-in distortion is governed by the relation between the in-plane and through the thickness properties. A 3D interlock fabric has significantly more fibers in the out-of-plane direction than conventional two-dimensional fabrics. Consequently, the spring-in angle in such composites should be lower than that of conventional two-dimensional fabrics (Tan et al., 1999; Tandon, 2006).

Figure 6.11 shows the spring-in evolution during the post-curing cycle. The results were normalized by the spring-in computed after the manufacturing process. The spring-in increased after being submitted to a higher the post-curing temperature, as it was observed in the asymmetric plate. The model predicts a 27 % increase in the spring-in after a 30-minute post-curing at 150 °C. These results were in agreement with those presented by Svanberg and Holmberg (2004b), where they measured a spring-in increase by up to 30 % after submitting a L-shaped part to a four-hour free standing post-curing. The numerical results confirm that the increment in the spring-in angle after submitting the part to a free-standing post-curing cycle is related to the composite's viscoelastic behavior, and not to the "frozen-in" strains.

Finally, it was shown that the spring-in increase measured by Svanberg and Holmberg (2004b) after submitting L-shaped parts to free standing post-curing can be predicted numerically with a viscoelastic model.

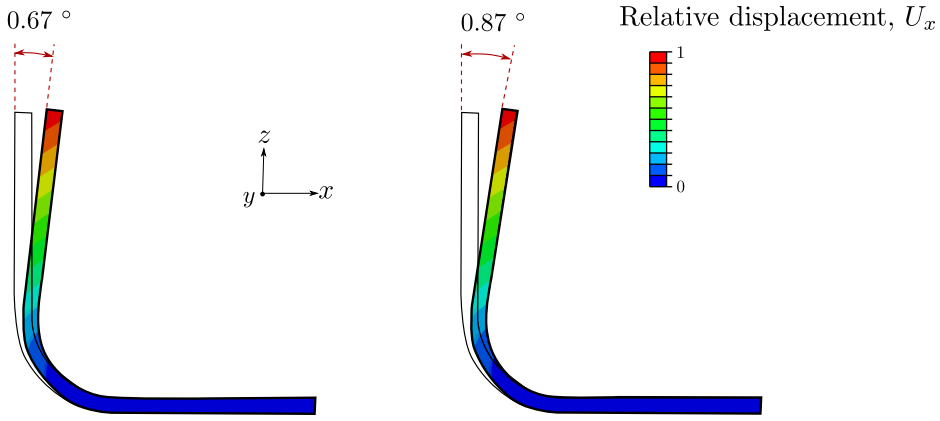

a) After manufacturing b) After 30 min isotherm at 150°C

Figure 6.10 Corner spring-in at room temperature after manufacturing (a) and after 30 minutes isotherm at 150 °C (b)

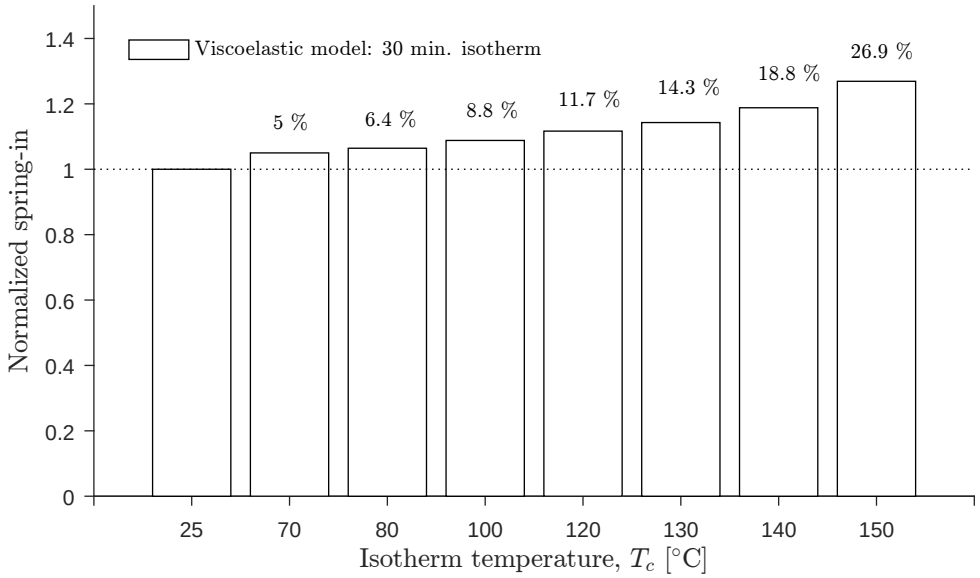

Figure 6.11 Spring-in evolution during subsequents 30 minutes isotherm post-curing

6.6 Conclusion

This paper presented a numerical analysis of process-induced residual distortions during manufacturing and post-curing in flat plates with asymmetric lay-up configuration and L-shaped composites parts. Degree of cure- and temperature-dependent elastic and viscoelastic models were implemented into a modular approach to simulate the thermo-chemo-mechanical phenomena occurring during the manufacturing and post-curing processes.

A characterization of the plates curvature with time and temperature revealed that the geometrical distortion could increase in up to 20 % depending on the post-cure temperature and duration. Svanberg and Holmberg (2001) suggested that this increment was caused by the "frozen-in" strains developed during the in-mold manufacturing. Those "frozen-in" strains could be released when the part was heated above its glass transition temperature, thus increasing the geometrical distortion once the part is cooled down to room temperature. Recently, Benavente et al. (2017a) presented an hypothesis that stated that the geometrical distortion increment was generated by the creep strains that can occur during a free-standing post-curing process.

The numerical results presented in this work revealed that the elastic model was not able to predict any geometrical distortion evolution during post-curing as it was observed experimentally. The results obtained with the viscoelastic model predicted a 10 % curvature increment after submitting the plate to a 30-minute free-standing post-curing at 150 °C. Moreover, the viscoelastic model reproduces accurately the time- and temperature-dependency measured experimentally. These results confirmed that the geometrical distortion evolution after submitting a part to a free-standing post-curing is caused by the creep strains, and hence, a viscoelastic model is needed to predict this phenomenon. The numerical simulations carried out in L-shaped parts using the viscoelastic model confirm that the spring-in could increase by up to 27 % depending on the post-cure temperature and duration. These results were in agreement with experimental data from the literature.

To conclude, the numerical results confirmed that creep strains occurred during free-standing post-curing. The part's total geometrical deformation can increase by up to 30 %, depending in the post-curing cycle and part geometry. Significant geometrical distortion was predicted by the viscoelastic model at temperatures below the glass transition temperature. Instantaneous creep strains were observed both, experimentally and numerically, during the heating-up phase above 80 °C. Neglecting the viscoelastic phenomenon during the post-curing process or in parts that are submitted to thermal cycles during their service life can be detrimental. Thus, a temperature-dependent viscoelastic model is required to compute accurately

the geometrical distortion developed during cure cycles where free-standing post curing is involved.

Acknowledgments

The authors would like to acknowledge Safran Group and the Canada Research Chair program for the financial support and for providing the resin and reinforcements used in this work. The National Science and Engineering Research Council (NSERC) of Canada, the Fonds Québécois pour la Recherche sur la Nature et les Technologies (FQRNT), the Canada Foundation for Innovation (CFI) and of the Ministère de l'Éducation du Québec are gratefully acknowledge for their contribution with the infrastructure and expenses of the composite laboratory. The authors also thank the contribution of Thierry Godon for his technical support.

CHAPTER 7 GENERAL DISCUSSION

The aim of this thesis was to develop a numerical tool to predict the residual stresses evolution during the manufacturing and free-standing post-curing processes of composite. The results of this study are given in the three papers presented above and discussed in this section.

7.1 Physical origins of process-induced geometrical distortions

Several authors observed that the geometrical distortions could increase significantly after submitting a part to a free-standing post-curing cycle (White and Hahn, 1993; Svanberg and Holmberg, 2001; Hubert et al., 2002; Pazdzior et al., 2004; Svanberg and Holmberg, 2004b). White and Hahn (1993) associated this geometrical distortion evolution with an additional resin cure and, hence, chemical shrinkage and mechanical properties evolution. However, this increment was also measured in plates that were completely cured prior to the post-curing process, and therefore an additional cure should not be expected. For completely cured samples, Svanberg and Holmberg (2001) suggested that the evolution of geometrical distortion measured after the free-standing post-curing could be explained by the release of "frozen-in" strains developed during the in-mold manufacturing process. "Frozen-in" strains are locked into the part when the material transforms from rubbery to glassy state. During the post-curing process the "frozen-in" strains are totally or partially released, increasing the part's geometrical distortion. However, the physical origin of the "frozen-in" strains and their release during the post-curing process can be questioned.

In this thesis, an hypothesis based on the composite's viscoelastic behavior was presented to explain the geometrical distortion evolution after submitting a part to a free-standing post-curing process. This hypothesis stated that, during a free-standing post-curing process, creep strains can occur during the heating and isotherm phases, thus increasing the part's geometrical distortion once it is cooled-down to its initial temperature.

To validate this hypothesis, plates with asymmetric lay-up configuration were manufactured by RTM and submitted to different free-standing post-curing cycles. The degree of cure and glass transition temperature measured after the RTM process by a DSC revealed that the plates were completely cured prior to the post-curing cycle. Thus, an additional resin cure or glass transition evolution was not possible during the post-curing cycle. The geometrical distortion evolution was then characterized during and after submitting the plates to several free-standing post curing cycles. The results revealed that the increase of the geometrical

distortion measured after submitting the part to a free-standing post-curing cycle was time- and temperature-dependent. A higher geometrical distortion was encountered in asymmetric plates submitted to a higher temperature for the same post-cure duration. Similar results were obtained after submitting the part to a longer post-curing cycle at the same temperature.

Part geometry

The numerical results suggested that the effect of the creep behavior occurring during the isotherms had a higher impact on L-shaped parts than in the asymmetric plate geometrical distortion, increasing the geometrical distortion by 27 and 10 %, respectively, for the same post-curing cycle.

Figure 7.1 shows the strains evolution over time when submitted to a constant uniaxial load of 10 MPa at 140 °C in the warp, weft and through-thickness directions. The results revealed that the warp and weft directions had a similar creep behavior and creep strains of around 15 % were computed for both direction. On the other hand, the strains in the through-thickness direction increase by 70 % over the creep test. This can be explained by the fact that the through-thickness direction mechanical properties are governed by the matrix. When considering that the spring-in is governed by the through-thickness mechanical properties, it would be expected that the geometrical distortion evolution in L-shaped parts during post-curing is more significant than in asymmetric plates. These results suggest that the geometrical distortion evolution depends on the part geometry and the post-curing cycle. However, further analyses should be carried out to investigate the geometrical distortions in different part geometries to validate these results.

7.2 Modeling aspects

A modular approach was developed in this work to predict the residual stresses developed during the RTM manufacturing and post-curing processes. A preliminary study was carried out to compute the effect of the injection stage on the residual stresses development. First, the injection stage evolution was computed by PAM-RTM software. The degree of cure and temperature gradient along the part at the end of the injection was transferred into ABAQUS and used as initial conditions. The results revealed that accounting for the injection stage led to differences lower than 1 % of the total geometrical distortion developed during the studied manufacturing cycle in asymmetric plates. The effect of the injection stage was therefore neglected in the sequel. However, these results only apply to the part, tool, materials

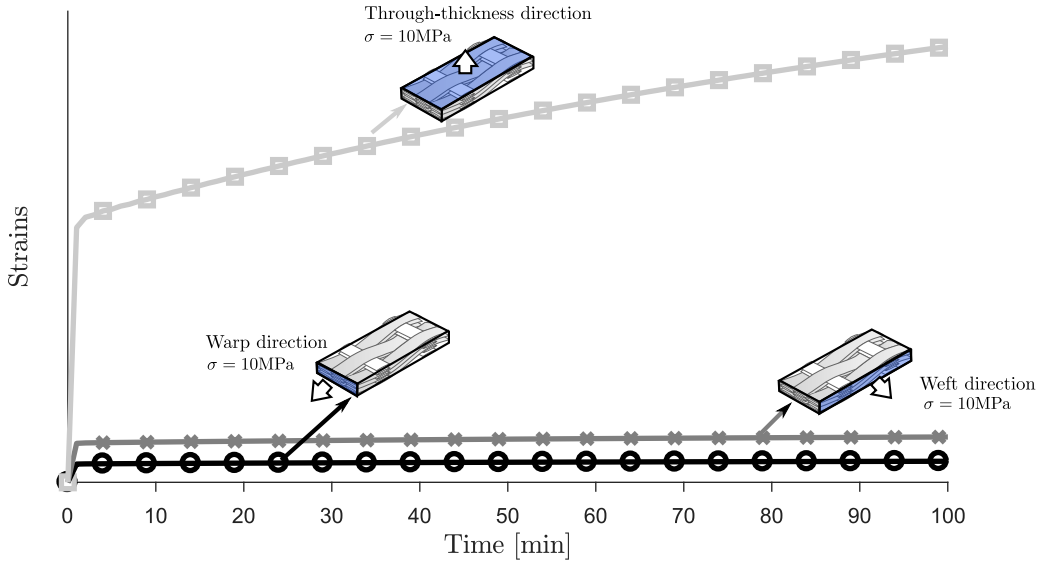

Figure 7.1 Creep strain evolution in the warp, weft and through-thickness directions during uniaxial 100 minutes creep tests at 140 °C

and molding cycle studied in this research. Larger parts, more reactive resin systems, or thermally unbalanced tools may lead to different results, where the injection stage may have an important impact on residual stresses and consequent geometrical distortions.

Finally, it was assumed that the residual stresses developed prior the resin's gel-point were immediately relaxed. Note that the gel point of the studied resin was fixed at $\alpha = 0.7$, thus, only 30 % of the chemical shrinkage induced to permanent residual stresses in the final part.

7.2.1 Linearly viscoelastic model

A linearly viscoelastic model was used in this thesis to compute the residual stresses developed during the manufacturing and post-curing process. Several assumptions were considered to develop this model :

- The composite had an orthotropic behavior.
- The inverted relaxation times, $\omega(k)$, and the activation energies used in the shift factor (equation 5.28) were the same as those from the epoxy resin.
- The composite remains in the linearly viscoelastic domain for all the temperatures and conditions studied.

The numerical results revealed that the implemented viscoelastic model predicted accurately the geometrical distortions measured after the fabrication and during the post-curing process. However, the results also showed that the viscoelastic model overestimated the creep strains at

low temperatures (below 120 °C) and underestimated the creep strains at high temperatures (above 150 °C) over time. Further analyses are needed to improve the viscoelastic model at high temperatures and to validate all the assumptions presented above.

7.2.2 Constitutive laws

Several authors have studied the predictive capabilities of non-viscoelastic models, such as the instantaneous-elastic or path-dependent models, to predict the geometrical distortions developed during the manufacturing process of composite parts. It was found that the instantaneous-elastic models could predict satisfactorily the geometrical distortions after the manufacturing of composite parts (Fernlund et al., 2002; David A. Darrow and Smith, 2002; Ersoy et al., 2010b). However, the results presented in this thesis have revealed that the instantaneous-elastic and path-dependent models were not suitable for analyses involving mechanical properties variation. They should not, therefore, be used to predict the residual stresses during manufacturing.

Moreover, it has been shown that the thermo-elastic and viscoelastic models could predict accurately the geometrical distortion encountered in asymmetric plates after the studied RTM manufacturing cycle. However, the thermo-elastic model required 30 times less computation time than the viscoelastic model. This difference between the two models is related to the viscoelastic model complexity. The viscoelastic model was composed by 13 relaxation tensors, $\mathbf{C}^{(k)}$, that led to large $\mathbf{L}^{(2)}$ (78×6) and $\mathbf{L}^{(3)}$ (78×78) matrices, increasing the computational time. The second-order Crank Nicolson (see Appendix B) scheme was implemented into ABAQUS to increase the convergence rate. However, the results in single elements simulations revealed that the CN scheme presented oscillations at high temperature, as shown in Figure 7.2. These oscillations were associated to the resolution method for the viscoelastic properties above the glass transition temperature used in this project.

Thermo-elastic models do not account for stress relaxation that can occur during the in-mold manufacturing process. Thus, different cure cycles could lead to significant discrepancies between the thermo-elastic and viscoelastic models and, hence, with the experimental geometrical distortion. Moreover, the experimental results revealed that creep strains occurring during the post-cure could increase by 20 % the geometrical distortion in asymmetric plates. This phenomenon was well captured by the viscoelastic model while it was neglected by the thermo-elastic model.

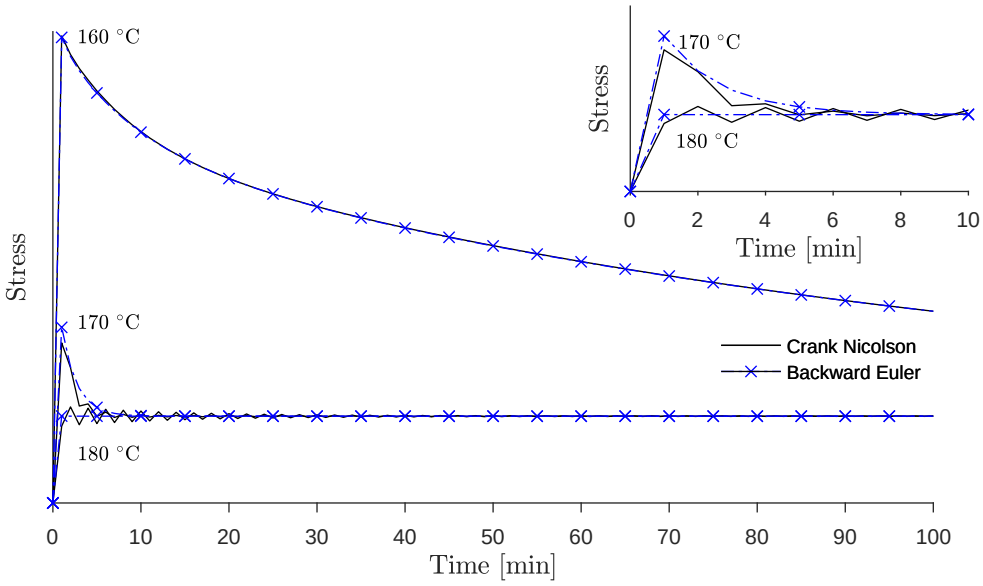

Figure 7.2 Stress relaxation evolution in the warp direction at different temperatures computed with the Crank Nicholson and backward Euler methods

CHAPTER 8 CONCLUSION AND RECOMMENDATIONS

This thesis investigated the physical origins of the geometrical distortion evolution triggered by the residual stresses during the manufacturing and post-curing processes of composite asymmetric plates. The purpose was to develop a numerical tool that accounted for the thermo-chemo-mechanical phenomena occurring during the RTM and post-curing processes thermoset-composite parts.

The impact of the viscoelastic behavior on the part's geometrical distortion was studied experimentally during the post-curing process. Six completely-cured asymmetric plates were submitted to free-standing post-curing cycles at various temperatures and duration. Digital image analysis was used to measure the geometrical distortion evolution encountered in asymmetric plates during the post-curing process. The results showed that creep strains occurred during the free-standing post-curing process at high temperatures, thus increasing the plates geometrical distortion. The study revealed that the part experienced an irreversible 20 % increase in geometrical distortion after being heated free-standing above its glass transition temperature for short periods of time (30 minutes). For lower temperatures, a longer exposure time was needed to achieve the stabilized creep strains. In-mold post-curing process induced internal stress relaxation that led a 6 % reduction in the geometrical distortion after 30 minutes above the resin's glass transition temperature.

Elastic, viscoelastic and path-dependent constitutive laws were implemented in ABAQUS to study their validity and accuracy. Simulations were then performed in a single element submitted to different thermal and load cycles constituted of creep and relaxation periods. The results revealed that the instantaneous-elastic implementation, generally used in the literature, and path-dependent model, led to results that were not physically coherent and, therefore, were not suitable to predict the residual stresses developed during the manufacturing process. Moreover, the viscoelastic model predicted significant stresses relaxation and creep strains in the warp direction during the simulations carried out at high temperature. This result confirmed that the viscoelastic behavior should not be neglected during analyses carried out at high temperature.

A sequentially modular approach was developed to simulate the thermo-chemo-mechanical phenomena involved in the manufacturing and post-manufacturing processes. The geometric distortion developed in asymmetric plates during the manufacturing and post-curing cycle was predicted by an elastic and a viscoelastic model. The geometrical distortion predicted by the elastic and viscoelastic models after the manufacturing process led to discrepancies

lower than 5 %, when compared to the experimental data for the studied cure cycle. However, only the viscoelastic model predicted the time- and temperature-dependent increment of the geometrical distortion phenomenon observed experimentally during the post-curing process. The numerical results predicted that the creep strains developed during the post-curing cycle can led to an increase of 15 to 30 % in the geometrical distortion, depending on thermal cycle and part geometry. Thus, a degree of cure- and temperature-dependent viscoelastic model is needed to accuratly predict the phenomena occurring during the whole manufacturing process. These results confirmed that the increase of the geometrical distortion is generated by the creep strains related to the viscoelastic behavior and that it is time and temperature dependent.

Table 8.1 and 8.2 recall the main mechanisms inducing to residual stresses and the numerical models used to predict them, respectively, presented in the literature during the manufacturing and post-curing processes. The contributions made during this project are presented in blue.

Finally, the numerical tool developed during this work has been transferred to our industrial partner and it is currently being used to predict the residual stresses and geometrical distortions developed during the RTM manufacturing and post-manufacturing treatments (*i.e.,* post-curing or bonding) of structural parts.

Limitations and recommendations for future studies

- **Investigate the effect of the tool-part interaction :**
  It would of interest to evaluate the effect of the tool-part interaction on the thermochemical and mechanical analysis. One could study the influence of using different numerical contact interactions (*i.e.,* perfectly constrained, friction model). Further, experimental analysis could be used to fully understand the interaction evolution with the degree of cure and temperature. Polytetrafluoroethylene (PTFE) films could be glued on the mold surface to experimentally investigate the tool-part interaction effect on thick parts. Finally, the experimental results could be used to validate the friction model implemented into the numerical tool.
  The effect of the tool part-interaction during the post-curing process has been observed to have a direct influence on the geometrical distortion. Further, numerical and experimental analysis would be interesting to fully understand the geometrical distortion evolution over time.

- **Optimization of the viscoelastic model and its implementation into the FE software** :

Table 8.1 Main mechanisms inducing to residual stresses and geometrical distortion during the manufacturing and post-curing processes and completed with the contributions made during this project (in blue)

	Phenomena	Contribution during manufacturing	Contribution during P-C
Tool-part interaction	Physical	Significant	–
Chemical shrinkage	Chemical	Significant	Unknown
CTE mismatch	Physical	Significant	–
Viscoelastic behavior	Physical	Unknown	Significant
~~**"Frozen-in" strains**~~	~~Phenomenological~~	~~Unknown~~	~~Unknown~~

Table 8.2 Numerical models used in the literature to predict the residual stresses and geometrical distortion developed during the manufacturing and post-curing processes. The contribution of this project on the numerical models are presented in blue. T= Temperature, t= time, DoC= Degree of cure, FD= Finite differences and P-C= Post-cure

	Elastic		Viscoelastic	Path-Dependent
Model development	Easy		Complex	Easy
Phenomena	T and DoC		T, t and DoC	T, DoC and "frozen-in" stress
Computational time	Fast		Long	Fast
Implementation	Thermo	Instantaneous	FD	Similar to instantaneous
Validity	**Valid**	**Non-valid**	**Valid**	**Non-valid**
Accuracy during RTM	Good	–	Excellent	–
Accuracy during P-C	Poor	–	Excellent	–

The numerical results revealed that the viscoelastic model did not accurately predict the composite viscoelastic behavior at high temperatures. Therefore, further analysis should be carried out to study the composite's viscoelastic behavior near or above its glass transition temperature. The use of non-linear viscoelastic models should be probably taken into consideration for low degrees of cure and high temperatures.
A first order backward Euler finite difference scheme was used to implement the degree of cure- and temperature-dependent linearly viscoelastic model during this work. It could be interesting to implement a higher order finite difference scheme, such as Crank-Nicolson or Runge-Kutta second and fourth order, respectively. These methods would increase the convergence ratio and, therefore, could be used to reduce the computation time.

- **Investigate the effect of reinforcement deformation and shear :**
  This thesis was limited to simple geometries, with constant fiber volumetric fraction and known fiber orientation. However, in complex parts, such as in aerospace fan cases and fan blades, the reinforcement is forced into the part shape, thus modifying the local volumetric fraction and fiber orientation. Further analysis should be carried out to study the effect of the reinforcement deformation, wrinkling and fiber shearing in the composites mechanical properties, and hence in the residual stresses and geometrical distortion.

REFERENCES

Adolf, D. B. and Chambers, R. S. (2007). A thermodynamically consistent, nonlinear viscoelastic approach for modeling thermosets during cure. *Journal of Rheology*, 51(1) :23–50.

Albert, C. and Fernlund, G. (2002). Spring-in and warpage of angled composite laminates. *Composites Science and Technology*, 62(14) :1895–1912.

Arafath, A. R. A., Vaziri, R., and Poursartip, A. (2008). Closed-form solution for process-induced stresses and deformation of a composite part cured on a solid tool : part i–flat geometries. *Composites Part A : Applied Science and Manufacturing*, 39(7) :1106–1117.

Baran, I., Akkerman, R., and Hattel, J. H. (2014). Material characterization of a polyester resin system for the pultrusion process. *Composites Part B : Engineering*, 64 :194 – 201.

Baran, I., Cinar, K., Ersoy, N., Akkerman, R., and Hattel, J. H. (2016). A review on the mechanical modeling of composite manufacturing processes. *Archives of Computational Methods in Engineering*, 24 (2) :365–395.

Baucom, J. and Zikry, M. (2005). Low-velocity impact damage progression in woven e-glass composite systems. *Composites Part A : Applied Science and Manufacturing*, 36(5) :658–664.

Bayraktar, H., Tsukrov, I., Giovinazzo, M., Goering, J., Gross, T., Fruscello, M., and Martinsson, L. (2012). Predicting cure-induced microcracking in 3d woven composites with realistic simulation technology. In *Society for the Advancement of Material and Process Engineering*.

Bažant, Z. (1972). Matrix differential equation and higher-order numerical methods for problems of non-linear creep, viscoelasticity and elasto-plasticity. *International Journal for Numerical Methods in Engineering*, 4(1) :11–15.

Benavente, M., Marcin, L., Courtois, A., Levesque, M., and Ruiz, E. (2017a). Viscoelastic distortion in asymmetric plates during post curing. *Composites Part A : Applied Science and Manufacturing*, 103 :122–130.

Benavente, M., Marcin, L., Godon, T., Courtois, A., Lévesque, M., and Ruiz, E. (2017b). Numerical analysis of process-induced residual distortions in asymmetric plates : Fe implementation of different constitutive laws. *Composites Part A : Applied Science and Manufacturing - Submitted*.

Billotte, C., Bernard, F., and Ruiz, E. (2013). Chemical shrinkage and thermomechanical characterization of an epoxy resin during cure by a novel in situ measurement method. *European Polymer Journal*, 49(11) :3548 – 3560.

Biot, M. A. (1954). Theory of stress-strain relations in anisotropic viscoelasticity and relaxation phenomena. *Journal of Applied Physics*, 25(11) :1385–1391.

Bogetti, T. A. and Gillespie Jr, J. W. (1991). Two-dimensional cure simulation of thick thermosetting composites. *Journal of Composite Materials*, 25(3) :239–273.

Bogetti, T. A. and Gillespie Jr, J. W. (1992). Process-induced stress and deformation in thick-section thermoset composite laminates. *Journal of Composite Materials*, 26(5) :626–660.

Brauner, C., Block, T. B., and Herrmann, A. S. (2012). Meso-level manufacturing process simulation of sandwich structures to analyze viscoelastic-dependent residual stresses. *Journal of Composite Materials*, 46(7) :783–799.

Canal, L. P., Benavente, M., Hausmann, M., and Michaud, V. (2015). Process-induced strains in rtm processing of polyurethane/carbon composites. *Composites Part A : Applied Science and Manufacturing*, 78 :264 – 273.

Cann, M. T. and Adams, D. O. (2001). Effect of part-tool interaction on cure distortion of flat composite laminates. In *46th International SAMPE Symposium and Exhibition-2001 a Materials and Processes Odyssey*.

Carbajal, N., Vargas, G., Arrese, A., and Mujika, F. (2008). Analysis of thermal stresses in unsymmetric cross-ply composite strips. *Journal of Composite Materials*, 42(12) :1247–1266.

Carpenter, W. C. (1972). Viscoelastic stress analysis. *International Journal for Numerical Methods in Engineering*, 4(3) :357–366.

Causse, P., Ruiz, E., and Trochu, F. (2012). Spring-in behavior of curved composites manufactured by flexible injection. *Composites Part A : Applied Science and Manufacturing*, 43(11) :1901–1913.

Causse, P. and Trochu, F. (2012). Analyse des contraintes et déformations résiduelles lors de la mise en forme de composites à matrice thermodurcissable : synthèse bibliographique. État de l'art sur les contraintes résiduelles.

Cheung, A., Yu, Y., and Pochiraju, K. (2004). Three-dimensional finite element simulation of curing of polymer composites. *Finite Elements in Analysis and Design*, 40(8) :895 – 912.

Courtois, A., Hirsekorn, M., Vernet, N., Marcin, L., Ruiz, E., and Lévesque, M. (2016). Viscoelastic behavior of an epoxy resin during cure : Characterization and modeling. In *The 10th International Conference on the Mechanics of Time Dependent Materials, Paris, 2016*.

Cowley, K. D. and Beaumont, P. W. (1997). The measurement and prediction of residual stresses in carbon-fibre/polymer composites. *Composites Science and Technology*, 57(11) :1445 – 1455.

Crochon, T. (2014). *Modeling of the viscoelastic behavior of a polyimide matrix at elevated temperatures*. PhD thesis, Université de Montréal.

Crochon, T., Schönherr, T., Li, C., and Lévesque, M. (2010). On finite-element implementation strategies of schapery-type constitutive theories. *Mechanics of Time-Dependent Materials*, 14(4) :359–387.

David A. Darrow, J. and Smith, L. V. (2002). Isolating components of processing induced warpage in laminated composites. *Journal of Composite Materials*, 36(21) :2407–2419.

De Luycker, E., Morestin, F., Boisse, P., and Marsal, D. (2009). Simulation of 3d interlock composite preforming. *Composite Structures*, 88(4) :615–623.

de Oliveira, R., Lavanchy, S., Chatton, R., Costantini, D., Michaud, V., Salathé, R., and Månson, J.-A. (2008). Experimental investigation of the effect of the mould thermal expansion on the development of internal stresses during carbon fibre composite processing. *Composites Part A : Applied Science and Manufacturing*, 39(7) :1083 – 1090.

Ding, A., Li, S., Sun, J., Wang, J., and Zu, L. (2016a). A comparison of process-induced residual stresses and distortions in composite structures with different constitutive laws. *Journal of Reinforced Plastics and Composites*, 35(10) :807–823.

Ding, A., Li, S., Sun, J., Wang, J., and Zu, L. (2016b). A thermo-viscoelastic model of process-induced residual stresses in composite structures with considering thermal dependence. *Composite Structures*, 136 :34 – 43.

Ding, A., Li, S., Wang, J., Ni, A., and Zu, L. (2017). A new path-dependent constitutive model predicting cure-induced distortions in composite structures. *Composites Part A : Applied Science and Manufacturing*, 95 :183–196.

Dong, C. (2011). Model development for the formation of resin-rich zones in composites processing. *Composites Part A : Applied Science and Manufacturing*, 42(4) :419–424.

Ersoy, N., Garstka, T., Potter, K., Wisnom, M. R., Porter, D., Clegg, M., and Stringer, G. (2010a). Development of the properties of a carbon fibre reinforced thermosetting composite through cure. *Composites Part A : Applied Science and Manufacturing*, 41(3) :401 – 409.

Ersoy, N., Garstka, T., Potter, K., Wisnom, M. R., Porter, D., and Stringer, G. (2010b). Modelling of the spring-in phenomenon in curved parts made of a thermosetting composite. *Composites Part A : Applied Science and Manufacturing*, 41(3) :410–418.

Ersoy, N., Potter, K., Wisnom, M. R., and Clegg, M. J. (2005). Development of spring-in angle during cure of a thermosetting composite. *Composites Part A : Applied Science and Manufacturing*, 36(12) :1700 – 1706.

Fernlund, G., Poursartip, A., Twigg, G., and Albert, C. (2003). Residual stress, spring-in and warpage in autoclaved composite parts. *Technical Papers-Society Of Manufacturing Engineers-All Series*.

Fernlund, G., Rahman, N., Courdji, R., Bresslauer, M., Poursartip, A., Willden, K., and Nelson, K. (2002). Experimental and numerical study of the effect of cure cycle, tool surface, geometry, and lay-up on the dimensional fidelity of autoclave-processed composite parts. *Composites Part A : Applied Science and Manufacturing*, 33(3) :341–351.

Ferry, J. D. (1980). *Viscoelastic properties of polymers*. John Wiley & Sons.

Gao, Z.-S. and Young, W.-B. (2002). Study of the bending induced gap in fiber preforming of woven fiber mats. *Polymer composites*, 23(2) :239–248.

Gigliotti, M., Wisnom, M., and Potter, K. (2003). Development of curvature during the cure of as4/8552 [0/90] unsymmetric composite plates. *Composites Science and Technology*, 63(2) :187 – 197.

Golestanian, H. and El-Gizawy, A. S. (2001). Modeling of process induced residual stresses in resin transfer molded composites with woven fiber mats. *Journal of Composite Materials*, 35(17) :1513–1528.

Hahn, H. and Pagano, N. (1975). Curing stresses in composite laminates. *Journal of Composite Materials*, 9(1) :91–106.

Hahn, H. T. (1976). Residual stresses in polymer matrix composite laminates. *Journal of Composite Materials*, 10(4) :266–278.

Harper, B. and Weitsman, Y. (1981). Residual thermal stresses in an unsymmetrical cross-ply graphite/epoxy laminate. In *22nd Structures, Structural Dynamics and Materials Conference*, page 580.

Hello, G., Schneider, J., and Aboura, Z. (2014). Numerical simulations of woven composite materials with voxel-fe models. In *Proceedings of the 16th European Conference on Composite Materials*, pages 22–26.

Huang, X., Gillespie, J. W., and Bogetti, T. (2000). Process induced stress for woven fabric thick section composite structures. *Composite Structures*, 49(3) :303–312.

Hubert, P., Grimsley, B. W., Cano, R. J., and Pipes, R. B. (2002). Dimensional stability of complex shapes manufactured by the vartm process.

Hubert, P., Johnston, A., Poursartip, A., and Nelson, K. (2001). Cure kinetics and viscosity models for hexcel 8552 epoxy resin. In *International SAMPE symposium and exhibition*, pages 2341–2354. SAMPE ; 1999.

Ifju, P. G., Kilday, B. C., Niu, X., and Liu, S.-C. (1999). A novel method to measure residual stresses in laminated composites. *Journal of Composite Materials*, 33(16) :1511–1524.

Johnston, A., Vaziri, R., and Poursartip, A. (2001). A plane strain model for process-induced deformation of laminated composite structures. *Journal of Composite Materials*, 35(16) :1435–1469.

Johnston, A. A. (1997). *An integrated model of the development of process-induced deformation in autoclave processing of composite structures*. PhD thesis, University of British Columbia.

Joshi, S., Liu, X., and Lam, Y. (1999). A numerical approach to the modeling of polymer curing in fibre-reinforced composites. *Composites Science and Technology*, 59(7) :1003 – 1013.

Kamal, M. and Sourour, S. (1973). Kinetics and thermal characterization of thermoset cure. *Polymer Engineering & Science*, 13(1) :59–64.

Khoun, L., Centea, T., and Hubert, P. (2010). Characterization methodology of thermoset resins for the processing of composite materials—case study : Cycom 890rtm epoxy resin. *Journal of Composite Materials*, 44(11) :1397–1415.

Khoun, L., Challagulla, K., and Hubert, P. (2012). Thermo-mechanical properties of 5-harness satin fabric composites. *Journal of Composite Materials*, 46(25) :3121–3136.

Khoun, L., de Oliveira, R., Michaud, V., and Hubert, P. (2011). Investigation of process-induced strains development by fibre bragg grating sensors in resin transfer moulded composites. *Composites Part A : Applied Science and Manufacturing*, 42(3) :274 – 282.

Kiasat, M. and Mostofi, H. (2008). Theoretical simulation of cure-induced deformations of composite car body panels. *SPE Automotive and Composites Division*, 2(1135-1145).

Kim, K. and Hahn, H. (1989). Residual stress development during processing of graphite/epoxy composites. *Composites Science and Technology*, 36(2) :121–132.

Kim, Y. K. (2004). Process-induced residual stress analysis by resin transfer molding. *Journal of Composite Materials*, 38(11) :959–972.

Kim, Y. K. and Daniel, I. M. (2002). Cure cycle effect on composite structures manufactured by resin transfer molding. *Journal of Composite Materials*, 36(14) :1725–1743.

Kim, Y. K. and White, S. R. (1997). Viscoelastic analysis of processing-induced residual stresses in thick composite laminates. *Mechanics Of Composite Materials And Structures An International Journal*, 4(4) :361–387.

Kominar, V. (1996). Thermo-mechanical regulation of residual stresses in polymers and polymer composites. *Journal of Composite Materials*, 30(3) :406–415.

Lévesque, M., Derrien, K., Baptiste, D., and Gilchrist, M. D. (2008). On the development and parameter identification of schapery-type constitutive theories. *Mechanics of Time-Dependent Materials*, 12(2) :95–127.

Lévesque, M., Gilchrist, M. D., Bouleau, N., Derrien, K., and Baptiste, D. (2007). Numerical inversion of the laplace–carson transform applied to homogenization of randomly reinforced linear viscoelastic media. *Computational mechanics*, 40(4) :771–789.

Loos, A. C. and Springer, G. S. (1983). Curing of epoxy matrix composites. *Journal of Composite Materials*, 17(2) :135–169.

Luk-Cyr, J., Crochon, T., Li, C., and Lévesque, M. (2013). Interconversion of linearly viscoelastic material functions expressed as prony series : a closure. *Mechanics of Time-Dependent Materials*, 17(1) :53–82.

Machado, M., Cakmak, U. D., Kallai, I., and Major, Z. (2016). Thermomechanical viscoelastic analysis of woven-reinforced thermoplastic-matrix composites. *Composite Structures*, 157 :256–264.

Minakuchi, S. (2015). In situ characterization of direction-dependent cure-induced shrinkage in thermoset composite laminates with fiber-optic sensors embedded in through-thickness and in-plane directions. *Journal of Composite Materials*, 49(9) :1021–1034.

Mouritz, A., Bannister, M., Falzon, P., and Leong, K. (1999). Review of applications for advanced three-dimensional fibre textile composites. *Composites Part A : Applied Science and Manufacturing*, 30(12) :1445 – 1461.

Naik, N., Azad, S. N., and Prasad, P. D. (2002). Stress and failure analysis of 3d angle interlock woven composites. *Journal of Composite Materials*, 36(1) :93–123.

Nawab, Y., Jacquemin, F., Casari, P., Boyard, N., Borjon-Piron, Y., and Sobotka, V. (2013a). Study of variation of thermal expansion coefficients in carbon/epoxy laminated composite plates. *Composites Part B : Engineering*, 50 :144–149.

Nawab, Y., Jaquemin, F., Casari, P., Boyard, N., and Sobotka, V. (2013b). Evolution of chemical and thermal curvatures in thermoset-laminated composite plates during the fabrication process. *Journal of Composite Materials*, 47(3) :327–339.

Nawab, Y., Shahid, S., Boyard, N., and Jacquemin, F. (2013c). Chemical shrinkage characterization techniques for thermoset resins and associated composites. *Journal of Materials Science*, 48(16) :5387–5409.

Nawab, Y., Tardif, X., Boyard, N., Sobotka, V., Casari, P., and Jacquemin, F. (2012). Determination and modelling of the cure shrinkage of epoxy vinylester resin and associated composites by considering thermal gradients. *Composites Science and Technology*, 73 :81–87.

Nielsen, L. E. (1969). Cross-linking–effect on physical properties of polymers.

Nielsen, M. W. (2012). *Prediction of process induced shape distortions and residual stresses in large fibre reinforced composite laminates*. PhD thesis, Technical University of Denmark, DTU.

Novak, R. C. and DeCrescente, M. (1970). Fabrication stresses in graphite-resin composites. *Journal of Engineering for Power*, 92 :377–380.

O'Brien, D. J., Mather, P. T., and White, S. R. (2001). Viscoelastic properties of an epoxy resin during cure. *Journal of Composite Materials*, 35(10) :883–904.

Palerosi, A. C. and de Almeida, S. F. M. (2007). Thermoelastic evaluation of composite laminates using digital imaging processing. *Composites Part A : Applied Science and Manufacturing*, 38(11) :2283–2293.

Parlevliet, P. P., Bersee, H. E., and Beukers, A. (2006). Residual stresses in thermoplastic composites—a study of the literature—part i : Formation of residual stresses. *Composites Part A : Applied Science and Manufacturing*, 37(11) :1847 – 1857.

Pascault, J. and Williams, R. (1990). Relationships between glass transition temperature and conversion. *Polymer Bulletin*, 24(1) :115–121.

Pazdzior, P., Hubert, P., Johnston, A., and Djokic, D. (2004). In-situ monitoring of residual stress development during e-beam processing. In *49th SAMPE international symposium*.

Potter, K., Campbell, M., Langer, C., and Wisnom, M. (2005). The generation of geometrical deformations due to tool/part interaction in the manufacture of composite components. *Composites Part A : Applied Science and Manufacturing*, 36(2) :301 – 308. 7th International Conference on the Deformation and Fracture of Composites (DFC-7).

Prasatya, P., McKenna, G. B., and Simon, S. L. (2001). A viscoelastic model for predicting isotropic residual stresses in thermosetting materials : effects of processing parameters. *Journal of Composite Materials*, 35(10) :826–848.

Pupin, C., Ross, A., Dubois, C., Rietsch, J.-C., Vernet, N., and Ruiz, E. (2017). Formation and suppression of volatile-induced porosities in an rtm epoxy resin. *Composites Part A : Applied Science and Manufacturing*, 94 :146–157.

Rabearison, N., Jochum, C., and Grandidier, J.-C. (2011). A cure kinetics, diffusion controlled and temperature dependent, identification of the araldite ly556 epoxy. *Journal of Materials Science*, 46(3) :787–796.

Radford, D. (1987). *Shape stability in composites*. PhD thesis, Rensselaer Polytechnic Institute,Troy, NY.

Radford, D. (2010). Balancing mechanisms of distortion to yield distortion-free/shape stable composites. *Journal of Reinforced Plastics and Composites*, 29(12) :1875–1892.

Radford, D. and Diefendorf, R. (1993). Shape instabilities in composites resulting from laminate anisotropy. *Journal of Reinforced Plastics and Composites*, 12(1) :58–75.

Radford, D. and Rennick, T. (2000). Separating sources of manufacturing distortion in laminated composites. *Journal of Reinforced Plastics and Composites*, 19(8) :621–641.

Ruiz, E. and Trochu, F. (2005a). Numerical analysis of cure temperature and internal stresses in thin and thick rtm parts. *Composites Part A : Applied Science and Manufacturing*, 36(6) :806–826.

Ruiz, E. and Trochu, F. (2005b). Thermomechanical properties during cure of glass-polyester rtm composites : elastic and viscoelastic modeling. *Journal of Composite Materials*, 39(10) :881–916.

Ruiz, E. and Trochu, F. (2006). Multi-criteria thermal optimization in liquid composite molding to reduce processing stresses and cycle time. *Composites Part A : Applied Science and Manufacturing*, 37(6) :913–924.

Schapery, R. A. (1969). On the characterization of nonlinear viscoelastic materials. *Polymer Engineering & Science*, 9(4) :295–310.

Schneider, J., Hello, G., Aboura, Z., Benzeggagh, M., and Marsal, D. (2009). A meso-fe voxel model of an interlock woven composite. In *Proceeding of the international conference in composite materials 17th (ICCM17), Edinburgh, Scotland.*

Stefaniak, D., Kappel, E., Spröwitz, T., and Hühne, C. (2012). Experimental identification of process parameters inducing warpage of autoclave-processed cfrp parts. *Composites Part A : Applied Science and Manufacturing*, 43(7) :1081–1091.

Svanberg, J. and Holmberg, J. (2001). An experimental investigation on mechanisms for manufacturing induced shape distortions in homogeneous and balanced laminates. *Composites Part A : Applied Science and Manufacturing*, 32(6) :827 – 838.

Svanberg, J. and Holmberg, J. (2004a). Prediction of shape distortions. part ii. experimental validation and analysis of boundary conditions. *Composites Part A : Applied Science and Manufacturing*, 35(6) :723 – 734.

Svanberg, J. M., Altkvist, C., and Nyman, T. (2005). Prediction of shape distortions for a curved composite c-spar. *Journal of Reinforced Plastics and Composites*, 24(3) :323–339.

Svanberg, J. M. and Holmberg, J. A. (2004b). Prediction of shape distortions part i. fe-implementation of a path dependent constitutive model. *Composites Part A : Applied Science and Manufacturing*, 35(6) :711–721.

Tan, P., Tong, L., and Steven, G. P. (1999). Micromechanics models for mechanical and thermomechanical properties of 3d through-the-thickness angle interlock woven composites. *Composites Part A : Applied Science and Manufacturing*, 30(5) :637 – 648.

Tandon, R. (2006). *Mechanical Properties and Performance of Engineering Ceramics II*. WILEY.

Taylor, R. L., Pister, K. S., and Goudreau, G. L. (1970). Thermomechanical analysis of viscoelastic solids. *International Journal for Numerical Methods in Engineering*, 2(1) :45–59.

Tong, L., Mouritz, A. P., and Bannister, M. K. (2002). *3D Fibre Reinforced Polymer Composites : Introduction*. Elsevier Science, Oxford.

Tseng, S.-C. and Osswald, T. A. (1994). Prediction of shrinkage and warpage of fiber reinforced thermoset composite parts. *Journal of Reinforced Plastics and Composites*, 13(8) :698–721.

Turi, E. A. (1981). *Thermal characterization of polymeric materials*. Academic Press.

Twigg, G., Poursartip, A., and Fernlund, G. (2004a). Tool–part interaction in composites processing. part i : experimental investigation and analytical model. *Composites Part A : Applied Science and Manufacturing*, 35(1) :121–133.

Twigg, G., Poursartip, A., and Fernlund, G. (2004b). Tool–part interaction in composites processing. part ii : numerical modelling. *Composites Part A : Applied Science and Manufacturing*, 35(1) :135–141.

Unger, W. and Hansen, J. (1993). The effect of cooling rate and annealing on residual stress development in graphite fibre reinforced peek laminates. *Journal of Composite Materials*, 27(2) :108–137.

Wang, T.-M., Daniel, I., and Gotro, J. (1992). Thermoviscoelastic analysis of residual stresses and warpage in composite laminates. *Journal of Composite Materials*, 26(6) :883–899.

Weitsman, Y. (1979). Residual thermal stresses due to cool-down of epoxy-resin composites. *Journal of Applied Mechanics*, 46(3) :563–567.

White, S. and Hahn, H. (1992). Process modeling of composite materials : Residual stress development during cure. part ii. experimental validation. *Journal of Composite Materials*, 26(16) :2423–2453.

White, S. and Hahn, H. (1993). Cure cycle optimization for the reduction of processing-induced residual stresses in composite materials. *Journal of Composite Materials*, 27(14) :1352–1378.

White, S. R. and Kim, Y. K. (1998). Process-induced residual stress analysis of as4/3501-6 composite material. *Mechanics of Composite Materials and Structures an International Journal*, 5(2) :153–186.

Wisnom, M., Gigliotti, M., Ersoy, N., Campbell, M., and Potter, K. (2006). Mechanisms generating residual stresses and distortion during manufacture of polymer–matrix composite structures. *Composites Part A : Applied Science and Manufacturing*, 37(4) :522–529.

Worgull, M., Hétu, J. F., Kabanemi, K. K., and Heckele, M. (2006). Modeling and optimization of the hot embossing process for micro- and nanocomponent fabrication. *Microsystem Technologies*, 12(10) :947–952.

Yang, S. Y., Huang, C. K., and Chen, C. C. (2003). Effect of processing on precision of composite panels. *Materials and Manufacturing Processes*, 18(5) :769–781.

Yousefi, A., Lafleur, P., and Gauvin, R. (1997). Kinetic studies of thermoset cure reactions : a review. *Polymer Composites*, 18(2) :157–168.

Zeng, X. and Raghavan, J. (2010). Role of tool-part interaction in process-induced warpage of autoclave-manufactured composite structures. *Composites Part A : Applied Science and Manufacturing*, 41(9) :1174 – 1183.

Zhao, L., Warrior, N., and Long, A. (2006). A micromechanical study of residual stress and its effect on transverse failure in polymer–matrix composites. *International Journal of Solids and Structures*, 43(18) :5449 – 5467.

Zhu, Q., Geubelle, P. H., Li, M., and Tucker III, C. L. (2001). Dimensional accuracy of thermoset composites : simulation of process-induced residual stresses. *Journal of Composite Materials*, 35(24) :2171–2205.

Zobeiry, N. (2006). *Viscoelastic constitutive models for evaluation of residual stresses in thermoset composites during cure*. PhD thesis, University of British Columbia.

Zocher, M., Groves, S., and Allen, D. (1997). A three-dimensional finite element formulation for thermoviscoelastic orthotropic media. *International Journal for Numerical Methods in Engineering*, 40(12) :2267–2288.

APPENDIX A COMPOSITE PROPERTIES

The properties were normalized by the value of the shift factor, a_T, at room temperature of the fully cured composite (α=1).

Cure kinetics model

Pupin et al. (2017) characterized the cure kinetics evolution of the studied epoxy resin with a Q2000 M-DSC from TA Instruments. Constant heating ramps at rates of 2, 4, 5, 6 and 10 ° C/min from 20 to 220 ° C and isothermal cures near and above the glass transition temperature were carried out to develop the Kamal and Sourour model.

$$\frac{\mathrm{d}\alpha}{\mathrm{d}t} = (k_1 + k_2\alpha^m)\,(1-\alpha)^n\,F(\alpha) \tag{A.1}$$

$A_1[min]$	E_1	$A_2[min]$	E_2	m	n
4.17×10^3	1.38×10^3	1.83	3.44×10^3	0.41	0.66

where

$$F(\alpha) = \frac{1}{1+\exp(B_1(\alpha - B_2))} \tag{A.2}$$

being

$$B_1 = A_f + A_{f2}T \tag{A.3}$$

and

$$B_2 = E_f + E_{f2}T \tag{A.4}$$

A_{f1}	A_{f2}	E_{f1}	E_{f2}
53.24	$4.8 \times 10^{-}2$	0.16	$2.22\times 10^{-}3$

Specific heat and orthotropic thermal conductivity

The composite specific heat was modeled based on the mixed rule law as

$$\zeta_{pc} = \zeta_{pf}V^f + \zeta_{pr}(1-V^f) \tag{A.5}$$

where ζ_{pc} and ζ_{pc} where the fibers' and resin's specific heat specifically. The composite specific heat was expressed as shown in Table A.1.

Table A.1 Normalized composite specific heat properties

Temperature [°C]	25	50	75	100	125	150	175	200
Specific heat, ζ_{pc}	402.21	441.96	479.83	517.71	555.58	600.93	640.68	674.81

The thermal conductivity of the thermoset composite reinforced by a 3D interlock fabric was computed by a multi-scale homogenization technique and was expressed as shown in Table A.2.

Table A.2 Normalized thermal conductivity properties

		K1[W/m°C]	K1[W/m°C]	K1[W/m°C]
$\alpha = 0$	20 °C	1.72	0.96	0.25
	220 °C	2.65	1.43	0.31
$\alpha = 1$	20 °C	1.74	0.99	0.28
	220 °C	2.70	1.49	0.37

Chemical shrinkage and CTE properties

In the table : $\alpha_{gel} = 0.7$.

Table A.3 Normalized chemical shrinkage properties

	δ (Warp direction)	δ (Weft direction)	δ (Thickness direction)
$\alpha < \alpha_{gel}$	0	0	0
$\alpha \geq \alpha_{gel}$	-5.55×10^{-5}	-5.55×10^{-4}	-3.03×10^{-3}

Elastic models

The normalized stiffness tensors were defined as

$$\mathbf{C}^{(0)} = \begin{bmatrix} 61.64 & 3.03 & 3.31 & 0 & 0 & 0 \\ 3.03 & 29.46 & 2.65 & 0 & 0 & 0 \\ 3.31 & 2.65 & 5.51 & 0 & 0 & 0 \\ 0 & 0 & 0 & 3.77 & 0 & 0 \\ 0 & 0 & 0 & 0 & 1.10 & 0 \\ 0 & 0 & 0 & 0 & 0 & 1.61 \end{bmatrix} \times 10^9$$

$$\mathbf{C}_e^{(1)} = \begin{bmatrix} 59.20 & 2.61 & 2.76 & 0 & 0 & 0 \\ 2.61 & 27.55 & 2.01 & 0 & 0 & 0 \\ 2.76 & 2.01 & 4.20 & 0 & 0 & 0 \\ 0 & 0 & 0 & 2.69 & 0 & 0 \\ 0 & 0 & 0 & 0 & 0.78 & 0 \\ 0 & 0 & 0 & 0 & 0 & 1.16 \end{bmatrix} \times 10^9$$

Table A.4 Normalized Coefficient of thermal expansion

	$\boldsymbol{\theta}$ (Warp direction)	$\boldsymbol{\theta}$ (Weft direction)	$\boldsymbol{\theta}$ (Thickness direction)
$T < T_g(\alpha)$	0.78×10^{-6}	3.08×10^{-6}	33.45×10^{-6}
$T \geq T_g(\alpha)$	2.53×10^{-6}	9.21×10^{-6}	160.31×10^{-6}

$$\mathbf{C}^{(\infty)} = \begin{bmatrix} 995.52 & 105.63 & 31.87 & 0 & 0 & 0 \\ 105.63 & 556.69 & 14.48 & 0 & 0 & 0 \\ 31.87 & 14.48 & 23.97 & 0 & 0 & 0 \\ 0 & 0 & 0 & 0.87 & 0 & 0 \\ 0 & 0 & 0 & 0 & 0.61 & 0 \\ 0 & 0 & 0 & 0 & 0 & 0.84 \end{bmatrix} \times 10^7$$

Linearly viscoelastic model

Thirteen relaxation times, one per decade, were considered in the composites viscoelastic model going from 10^{-9} to 10^3 min. The normalized relaxation matrices $\mathbf{C}_{(k)}$ were given as follows for the viscoelastic model

$$\mathbf{C}^{(1)} = \begin{bmatrix} 20.46 & 3.23 & 4.14 & 0 & 0 & 0 \\ 3.23 & 13.16 & 5.08 & 0 & 0 & 0 \\ 5.08 & 4.14 & 10.43 & 0 & 0 & 0 \\ 0 & 0 & 0 & 9.28 & 0 & 0 \\ 0 & 0 & 0 & 0 & 2.93 & 0 \\ 0 & 0 & 0 & 0 & 0 & 4.15 \end{bmatrix} \times 10^7$$

$$\mathbf{C}^{(2)} = \begin{bmatrix} 22.18 & 3.35 & 4.42 & 0 & 0 & 0 \\ 3.35 & 14.09 & 5.04 & 0 & 0 & 0 \\ 5.04 & 4.42 & 10.43 & 0 & 0 & 0 \\ 0 & 0 & 0 & 9.70 & 0 & 0 \\ 0 & 0 & 0 & 0 & 3.02 & 0 \\ 0 & 0 & 0 & 0 & 0 & 4.28 \end{bmatrix} \times 10^7$$

$$\mathbf{C}^{(3)} = \begin{bmatrix} 23.15 & 3.43 & 4.59 & 0 & 0 & 0 \\ 3.43 & 14.67 & 5.59 & 0 & 0 & 0 \\ 4.59 & 5.59 & 11.42 & 0 & 0 & 0 \\ 0 & 0 & 0 & 9.99 & 0 & 0 \\ 0 & 0 & 0 & 0 & 3.07 & 0 \\ 0 & 0 & 0 & 0 & 0 & 4.35 \end{bmatrix} \times 10^7$$

$$\mathbf{C}^{(4)} = \begin{bmatrix} 24.39 & 3.48 & 4.81 & 0 & 0 & 0 \\ 3.48 & 15.29 & 5.84 & 0 & 0 & 0 \\ 4.81 & 5.84 & 11.92 & 0 & 0 & 0 \\ 0 & 0 & 0 & 10.35 & 0 & 0 \\ 0 & 0 & 0 & 0 & 3.15 & 0 \\ 0 & 0 & 0 & 0 & 0 & 4.45 \end{bmatrix} \times 10^7$$

$$\mathbf{C}^{(5)} = \begin{bmatrix} 26.76 & 3.71 & 5.07 & 0 & 0 & 0 \\ 3.72 & 16.64 & 6.11 & 0 & 0 & 0 \\ 5.07 & 6.11 & 12.46 & 0 & 0 & 0 \\ 0 & 0 & 0 & 10.72 & 0 & 0 \\ 0 & 0 & 0 & 0 & 3.22 & 0 \\ 0 & 0 & 0 & 0 & 0 & 4.56 \end{bmatrix} \times 10^7$$

$$\mathbf{C}^{(6)} = \begin{bmatrix} 25.94 & 3.42 & 5.25 & 0 & 0 & 0 \\ 3.42 & 16.09 & 6.35 & 0 & 0 & 0 \\ 5.25 & 6.35 & 12.86 & 0 & 0 & 0 \\ 0 & 0 & 0 & 11.02 & 0 & 0 \\ 0 & 0 & 0 & 0 & 3.29 & 0 \\ 0 & 0 & 0 & 0 & 0 & 4.65 \end{bmatrix} \times 10^7$$

$$\mathbf{C}^{(7)} = \begin{bmatrix} 35.13 & 4.66 & 5.79 & 0 & 0 & 0 \\ 4.67 & 21.23 & 6.82 & 0 & 0 & 0 \\ 5.79 & 6.83 & 13.92 & 0 & 0 & 0 \\ 0 & 0 & 0 & 11.65 & 0 & 0 \\ 0 & 0 & 0 & 0 & 3.42 & 0 \\ 0 & 0 & 0 & 0 & 0 & 4.83 \end{bmatrix} \times 10^7$$

$$\mathbf{C}^{(8)} = \begin{bmatrix} 17.52 & 1.69 & 5.29 & 0 & 0 & 0 \\ 1.60 & 11.18 & 6.57 & 0 & 0 & 0 \\ 5.29 & 6.57 & 13.07 & 0 & 0 & 0 \\ 0 & 0 & 0 & 11.35 & 0 & 0 \\ 0 & 0 & 0 & 0 & 3.35 & 0 \\ 0 & 0 & 0 & 0 & 0 & 4.74 \end{bmatrix} \times 10^7$$

$$\mathbf{C}^{(9)} = \begin{bmatrix} 78.36 & 11.21 & 9.11 & 0 & 0 & 0 \\ 11.21 & 46.02 & 10.14 & 0 & 0 & 0 \\ 9.11 & 10.14 & 20.92 & 0 & 0 & 0 \\ 0 & 0 & 0 & 16.2 & 0 & 0 \\ 0 & 0 & 0 & 0 & 4.6 & 0 \\ 0 & 0 & 0 & 0 & 0 & 6.47 \end{bmatrix} \times 10^7$$

$$\mathbf{C}^{(10)} = \begin{bmatrix} 19.72 & 16.85 & 25.72 & 0 & 0 & 0 \\ 16.85 & 16.48 & 27.40 & 0 & 0 & 0 \\ 25.72 & 27.40 & 47.73 & 0 & 0 & 0 \\ 0 & 0 & 0 & 41.66 & 0 & 0 \\ 0 & 0 & 0 & 0 & 12.59 & 0 \\ 0 & 0 & 0 & 0 & 0 & 17.79 \end{bmatrix} \times 10^7$$

$$\mathbf{C}^{(11)} = \begin{bmatrix} 61.09 & 8.02 & 8.82 & 0 & 0 & 0 \\ 8.02 & 36.01 & 9.98 & 0 & 0 & 0 \\ 8.82 & 9.98 & 19.78 & 0 & 0 & 0 \\ 0 & 0 & 0 & 14.38 & 0 & 0 \\ 0 & 0 & 0 & 0 & 3.76 & 0 \\ 0 & 0 & 0 & 0 & 0 & 5.31 \end{bmatrix} \times 10^8$$

$$\mathbf{C}^{(12)} = \begin{bmatrix} 123.23 & -6.67 & 8.13 & 0 & 0 & 0 \\ -6.67 & 52.83 & 6.33 & 0 & 0 & 0 \\ 8.13 & 6.33 & 12.84 & 0 & 0 & 0 \\ 0 & 0 & 0 & 6.97 & 0 & 0 \\ 0 & 0 & 0 & 0 & 2.13 & 0 \\ 0 & 0 & 0 & 0 & 0 & 3.44 \end{bmatrix} \times 10^8$$

$$\mathbf{C}^{(13)} = \begin{bmatrix} 282.05 & 11.78 & 3.95 & 0 & 0 & 0 \\ 11.78 & 120.15 & -1.18 & 0 & 0 & 0 \\ 3.95 & -1.18 & 0.75 & 0 & 0 & 0 \\ 0 & 0 & 0 & 0.08 & 0 & 0 \\ 0 & 0 & 0 & 0 & 0.22 & 0 \\ 0 & 0 & 0 & 0 & 0 & 0.40 \end{bmatrix} \times 10^8$$

DiBenedetto model and shift factor coefficient

$$\frac{T_g(\alpha) - T_g^{(0)}}{T_g^{(\infty)} - T_g^{(0)}} = \frac{\lambda\alpha}{1-(1-\lambda)\alpha} \tag{A.6}$$

$$\log(a_T(T,\alpha)) = \begin{cases} \frac{H_1}{(\ln 10)R}\left(\frac{1}{T} - \frac{1}{T_g(\alpha)}\right) & T \geq T_g(\alpha) \\ \frac{H_2}{(\ln 10)R}\left(\frac{1}{T} - \frac{1}{T_g(\alpha)}\right) & T < T_g(\alpha) \end{cases} \tag{A.7}$$

Table A.5 Normalized activation energies to compute the shift factor, $aT(T,\alpha)$ and the cure dependent glass transition temperature,$\mathrm{T}_g(\alpha)$

H1 [KJ/mol]	H2 [KJ/mol]	$\mathrm{T}_g^{(0)}$ [°C]	$\mathrm{T}_g^{(\infty)}$ [°C]	λ
110.95	249.63	-25	156	0.4

APPENDIX B CRANK NICOLSON IMPLEMENTATION

Crank Nicolson (CN) finite difference schema was used to implement the linearly viscoelastic model into ABAQUS. This schema is a second-order method in time, meaning that the convergence ratio is higher than for the first-order Euler backward method.

Crochon (2014) used the CN finite difference schema to solve the differential equations 2.13 as

$$\boldsymbol{\sigma}(t+\Delta t) = \mathbf{L}^{(1)} : \boldsymbol{\varepsilon}(t+\Delta t) + \mathbf{L}^{(2)} : \boldsymbol{\chi}(t+\Delta t) \tag{B.1}$$

where

$$\begin{aligned}\boldsymbol{\chi}(t+\Delta t) &= \boldsymbol{\chi}(t) + \frac{\Delta t}{2}\left(\dot{\boldsymbol{\chi}}(t) + \dot{\boldsymbol{\chi}}(t+\Delta t)\right) \\ &= \boldsymbol{\chi}(t) - \frac{\Delta t}{2}\mathbf{B}^{-1} : \left[\mathbf{L}^{(3)} : \left(\boldsymbol{\chi}(t) + \boldsymbol{\chi}(t+\Delta t)\right) + \left(\mathbf{L}^{(2)}\right)^{T} : \left(\boldsymbol{\varepsilon}(t) + \boldsymbol{\varepsilon}(t+\Delta t)\right)\right]\end{aligned} \tag{B.2}$$

The combination of equations B.1 and B.2 yielded

$$\begin{aligned}\boldsymbol{\sigma}(t+\Delta t) &= \mathbf{L}^{(1)} : \boldsymbol{\varepsilon}(t+\Delta t) + \mathbf{L}^{(2)} : \left[\mathbf{W}^{(1)} : \boldsymbol{\chi}(t) + \mathbf{W}^{(2)} : \left(\boldsymbol{\varepsilon}(t) + \boldsymbol{\varepsilon}(t+\Delta t)\right)\right] \\ &= \left(\mathbf{L}^{(1)} + \mathbf{L}^{(2)} : \mathbf{W}^{(2)}\right) : \boldsymbol{\varepsilon}(t+\Delta t) + \mathbf{L}^{(2)} : \mathbf{W}^{(1)} : \boldsymbol{\chi}(t) + \mathbf{L}^{(2)} : \mathbf{W}^{(2)} : \boldsymbol{\varepsilon}(t)\end{aligned} \tag{B.3}$$

where

$$\mathbf{W}^{(1)} = \mathbf{W}^{(3)} : \left(\mathbf{I} - \frac{\Delta t}{2}\mathbf{B}^{-1} : \mathbf{L}^{(3)}\right) \tag{B.4a}$$

$$\mathbf{W}^{(2)} = \mathbf{W}^{(3)} : \left(-\frac{\Delta t}{2}\mathbf{B}^{-1} : \left(\mathbf{L}^{(2)}\right)^{T}\right) \tag{B.4b}$$

$$\mathbf{W}^{(3)} = \left(\mathbf{I} + \frac{\Delta t}{2}\mathbf{B}^{-1} : \mathbf{L}^{(3)}\right)^{-1} \tag{B.4c}$$

Regrouping terms leads to

$$\boldsymbol{\sigma}(t+\Delta t) = \mathbf{M}^{(1)} : \boldsymbol{\varepsilon}(t+\Delta t) + \mathbf{M}^{(2)} : \boldsymbol{\chi}(t) + \mathbf{M}^{(3)} : \boldsymbol{\varepsilon}(t) \tag{B.5a}$$

$$\frac{\partial \Delta\boldsymbol{\sigma}}{\partial \Delta\boldsymbol{\varepsilon}} = \mathbf{M}^{(1)} \tag{B.5b}$$